Extraterrestrial Neutrinos as Probes of Their Sources and Interactions

A Dissertation Presented

by

Ningqiang Song

to

The Graduate School

in Partial Fulfillment of the Requirements

for the Degree of

Doctor of Philosophy

in

Physics

Stony Brook University

August 2018

Abstract of the Dissertation

Extraterrestrial Neutrinos as Probes of Their Sources and Interactions

by

Ningqiang Song

Doctor of Philosophy

in

Physics

Stony Brook University

2018

In this thesis we use results on extraterrestrial neutrinos from the Sun, from extragalactic objects and from the Early Universe to study several problems related to the characterization of their sources and their interactions. First we present an updated determination of the fluxes of neutrinos produced in the Sun and the construction of a new generation of Standard Solar Models. Motivated by the inconsistency between the prediction of these models and the global analysis of data from solar neutrino experiments and helioseismology, we study how to use that data to improve on the solar modeling. Next we describe and quantify how the flavor content of the detected high energy neutrinos from extragalactic sources, which is being used to characterize their production mechanism at the source, can be modified by non-standard interactions of the neutrinos with the Earth matter. Lastly we study the tension between sterile neutrinos as suggested by short baseline oscillation anomalies and cosmological observations. To alleviate those we introduce new interactions among sterile neutrinos and present the constraints on this new interaction imposed by cosmological data.

This thesis is mainly based on the following publications:

1. N. Song, M. C. Gonzalez-Garcia, F. L. Villante, N. Vinyoles and A. Serenelli, "Helioseismic and Neutrino Data Driven Reconstruction of Solar Properties," *Mon. Not. Roy. Astron. Soc.* (2018) [arXiv:1710.02147 [astro-ph.SR]].
2. N. Vinyoles, A. Serenelli, F. L. Villante, S. Basu, J. Bergstrom, M. C. Gonzalez-Garcia, M. Maltoni, C. Pena-Garay, N. Song, "A new Generation of Standard Solar Models," *Astrophys. J.* **835**, no. 2, 202 (2017) [arXiv:1611.09867 [astro-ph.SR]].
3. M. C. Gonzalez-Garcia, M. Maltoni, I. Martinez-Soler and N. Song, "Non-standard neutrino interactions in the Earth and the flavor of astrophysical neutrinos," *Astropart. Phys.* **84**, 15 (2016) [arXiv:1605.08055 [hep-ph]].
4. J. Bergstrom, M. C. Gonzalez-Garcia, M. Maltoni, C. Pena-Garay, A. M. Serenelli and N. Song, "Updated determination of the solar neutrino fluxes from solar neutrino data," *JHEP* **1603**, 132 (2016) [arXiv:1601.00972 [hep-ph]].

Additional work completed in the duration of the author's PhD career:

1. N. Song, R. Boyero Garcia, J. J. Gomez-Cadenas, M. C. Gonzalez-Garcia, A. Peralta Conde and J. Taron, "Conditions for Statistical Determination of the Neutrino Mass Spectrum in Radiative Emission of Neutrino Pairs in Atoms," *Phys. Rev. D* **93**, no. 1, 013020 (2016) [arXiv:1510.00421 [hep-ph]].

Dedicated to Jun and my father.

Contents

List of Figures

List of Tables

Acknowledgements

Firstly I would like to express my sincere gratitude to my advisor Concha for her endless help both in and beyond physics. Special thanks to her for the mentoring through these years, for the projects we worked through, for teaching me how to be a good author and speaker, especially, how to become a scientist, for offering me the opportunities to visit Spain and to attend summer schools, for introducing the collaborators who are so helpful, and for going over every detail of the dissertation. I learned from her the passion to be a physicist and to take responsibility for my own work and for everyone I work with.

I also would like to thank Johannes Bergstrom who has helped me live in a country with different language and culture, and guided me to the Bayesian world. Additional thanks to Dr. Michele Maltoni and Dr. Aldo Serenelli, who not only provided fruitful collaborations but also helped a lot in continuing my research career.

I should not forget to acknowledge Dr. Hong-shi Zong who instructed my first research in physics. Without his help I would not have started my PhD in Stony Brook University. I would like to appreciate the inspiring courses from which I benefited a lot here. Thanks to the professors for distilling the beautiful ideas in my mind. In addition, I would like to thank Dr. Xu Du and Dr. George Sterman for their advice in my oral exam and annual meetings, and especially thanks to Dr. George Sterman for all his help as my professor of the lectures, as the chair of my oral committee, as my referee and as the Director of YITP. I am also grateful for the seminars and meetings organized by Dr. Marilena Loverde, Dr. Rouven Essig and Dr. Patrick Meade which opened up new possibilities in my research.

Furthermore I would like to extend my thanks to my friends and officemates who made Stony Brook a wonderful place to live and study in. I would like to thank my colleagues Yao, Yanliang, Choi, Chi-Ting, Ivan, Jordi and many others who offered me valuable insights into important questions in physics.

Finally, I would like to thank my mother who devoted so much to me but I never got a chance to pay back. Thanks to my father, my sisters, my grandma and grandpa for supporting me all the way to be a researcher. Special thanks to my love for the company.

Chapter 1

Introduction

Neutrinos are ubiquitous in Nature. They were produced in the early universe, they are generated by the reactions that make the stars shine, by the interactions of cosmic rays – in particular with our atmosphere –, by radioactivity in our Earth .... To these "natural" neutrinos we have to add those generated by human constructions, including nuclear reactors and accelerators. Since the first observation of neutrinos in 1956, tremendous experimental efforts have been made to detect and study neutrinos from all different sources. They have led us to the confirmation of the flavour effects first observed in solar and atmospheric neutrino beams, with terrestrial accelerator and reactor neutrino experiments and have provided us with the first evidence of physics beyond the Standard Model.

In brief, all these experiments have established that lepton flavor is not conserved in neutrino propagation, but it oscillates with a wavelength depending on distance and energy, demonstrating beyond doubt that neutrinos are massive and the mass states are non-trivial admixtures of flavor states [15, 16], see Ref. [17] for an overview. For example, the results of the NuFIT 3.0 global fit to latest neutrino data in this now well-establish scenario of three-neutrino oscillations are summarized in Table 1.1 [5, 6].

Indeed, now that the neutrino mass differences and most oscillation parameters, are well established with the use of human made neutrinos, we can turn to use some of the results obtained with the natural neutrinos (in particular neutrinos from extraterrestrial sources) to explore some additional questions such as: What are the solar neutrino fluxes produced in the different reactions in the Sun? Are Standard Solar Models consistent with observed solar fluxes and other measurements? Are there non-standard interactions between active neutrinos? Do sterile neutrinos exist? If so, are there any exotic interactions among sterile neutrinos?.

We are trying to answer or partly answer these questions in this thesis

	Normal Ordering (best fit)		Inverted Ordering ($\Delta\chi^2 = 0.83$)	
	bfp $\pm 1\sigma$	3σ range	bfp $\pm 1\sigma$	3σ range
$\sin^2\theta_{12}$	$0.306^{+0.012}_{-0.012}$	$0.271 \to 0.345$	$0.306^{+0.012}_{-0.012}$	$0.271 \to 0.345$
$\theta_{12}/^\circ$	$33.56^{+0.77}_{-0.75}$	$31.38 \to 35.99$	$33.56^{+0.77}_{-0.75}$	$31.38 \to 35.99$
$\sin^2\theta_{23}$	$0.441^{+0.027}_{-0.021}$	$0.385 \to 0.635$	$0.587^{+0.020}_{-0.024}$	$0.393 \to 0.640$
$\theta_{23}/^\circ$	$41.6^{+1.5}_{-1.2}$	$38.4 \to 52.8$	$50.0^{+1.1}_{-1.4}$	$38.8 \to 53.1$
$\sin^2\theta_{13}$	$0.02166^{+0.00075}_{-0.00075}$	$0.01934 \to 0.02392$	$0.02179^{+0.00076}_{-0.00076}$	$0.01953 \to 0.02408$
$\theta_{13}/^\circ$	$8.46^{+0.15}_{-0.15}$	$7.99 \to 8.90$	$8.49^{+0.15}_{-0.15}$	$8.03 \to 8.93$
$\delta_{\rm CP}/^\circ$	261^{+51}_{-59}	$0 \to 360$	277^{+40}_{-46}	$145 \to 391$
$\dfrac{\Delta m^2_{21}}{10^{-5}\ \mathrm{eV}^2}$	$7.50^{+0.19}_{-0.17}$	$7.03 \to 8.09$	$7.50^{+0.19}_{-0.17}$	$7.03 \to 8.09$
$\dfrac{\Delta m^2_{3\ell}}{10^{-3}\ \mathrm{eV}^2}$	$+2.524^{+0.039}_{-0.040}$	$+2.407 \to +2.643$	$-2.514^{+0.038}_{-0.041}$	$-2.635 \to -2.399$

Table 1.1: Three-flavor oscillation parameters from the fit to global data in Ref. [5, 6]. The numbers in the 1st (2nd) column are obtained assuming NO, $m_1 < m_2 < m_3$ (IO, $m_3 < m_2 < m_2$), *i.e.*, relative to the respective local minimum. Note that $\Delta m^2_{3\ell} \equiv \Delta m^2_{31} > 0$ for NO and $\Delta m^2_{3\ell} \equiv \Delta m^2_{32} < 0$ for IO.

whose outline is as follows.

In Chapters 2 and 3 we focus on solar neutrinos. The Sun burns and produces energy through nuclear fusion via two sets of reactions known as the pp chain and the CNO cycle, of which the pp chain serves as the dominant source of energy and of neutrinos. These neutrinos, produced in the core of the Sun, reach the Earth and are then detected by a variety of experiments which renders us the possibility of determining the neutrino fluxes produced by the different reactions directly from neutrino data, this is, independently of the solar modeling and they are used to probe the solar interior. In Chapter 2 we present the results of our global analysis of neutrino oscillation data using Bayesian statistics and provide the results of such model-independent determination of the solar neutrino fluxes.

These newly determined solar neutrino fluxes in turn provide us with a better perspective of the solar models as we discuss in Chapter 3. Standard Solar Models (SSMs), as we will describe, are a snapshot in the evolution of a $1\,\mathrm{M}_\odot$ star, calibrated to match present-day properties of the Sun. And in Chapter 3 we introduce the newly constructed B16 solar models and quantify their statistical significance when confronting their predictions with the solar neutrino and helioseismic data. Motivated by the discrepancy between the SSMs predictions and the data – the so-called solar composition problem – we turn to study possible improvements in the solar modeling assumptions. In particular we scrutinize the solar opacity profile used in the models which is an input subject to biases associated with its assumed functional form. To avoid those we introduce the use of Gaussian Process, a minimum bias non-parametric regression method, to reconstruct the opacity profile and its uncertainty directly from the data. We also develop and apply the methodology to determine the chemical composition and other solar model inputs which better describe the helioseismic and neutrino observations.

Next, in Chapter 4, we focus on the ultra-high energy neutrinos produced in extragalactic sources and recently detected for the first time. The measurement of the flavour composition of these neutrinos has been proposed as a probe of the mechanism at work in their sources. This requires the precise knowledge of the flavour evolution of the neutrino ensemble from the source to the detector. As we describe in this chapter, in the now standard framework of three-neutrino oscillations, there is a well-determined correlation between the detected flavour composition and the one produced in the source. But as we discuss, this correlation can be modified if neutrinos have non-standard interactions which would affect their flavour evolution when crossing the Earth matter before reaching the detector. To quantify this effect we investigate how the neutrino flavor transition probability from the source to the detector is modified in the presence of a general form of Earth matter potential induced by the NSI. With those we can quantify the possible modification of the detected flavor composition which are still allowed within the existing bounds on the NSI.

Finally in Chapter 5 we focus on cosmological neutrinos, produced in the early universe, and study how cosmological data can be used to constrain secret interactions among eV scale sterile neutrinos which should be part of those cosmological neutrinos in proposed extensions of the standard three-neutrino scenario. As described in the chapter, this study requires understanding the expansion history of the universe and the corresponding evolution of its inhomogeneities and anisotropies which lead to the observed spectrum of cosmic microwave background (CMB) and large scale structure data. Neutrinos leave imprints on these observations which depend on their mass and interactions. The motivation of this study is a set of anomalies observed in short baseline oscillation experiments which favour sterile neutrinos of eV mass scale and non negligible mixing with the three active ones. Technically, to study the thermalization of such sterile neutrinos in the early universe we resort to the quantum kinetic equations (QKEs) with a momentum average approximation, and to quantify their effect on the evolution of the anisotropies and inhomogeneities the neutrino Boltzmann equations have to be modified. New interactions among these sterile states could also be accounted for in the same formalism and, depending on their strength, they can severely modify the effects that those sterile neutrinos have on the observables. Once all the effects are quantitatively accounted for we perform an statistical analysis of CMB and large scale structure data which allows us to constrain the parameter space for sterile neutrinos with such new interactions.

We provide a summary of the main conclusions in Chapter 6.

Chapter 2

Solar Neutrinos

The Sun, as a main-sequence star, has been burning for over 4.6 billion years. While it is commonly considered to be born in primordial gases bounded by gravity, one may question how the Sun stabilize itself form gravitational collapse over the years. The answer is pressure. There are two sources of pressure keeping the Sun balanced, one from the thermal motion of electrons and nuclei, and the other from the radiation of photons. The latter is a product of nuclear fusion inside the solar core. It was not until the discovery of neutrinos that people realized that photons are not the only particles which are generated in the Sun and are able to escape. Because of the Sun's opacity, it takes photons about 10^4 years to diffuse from the core to the surface of the Sun. Neutrinos, on the contrary, barely interact with the solar matter, and can escape the Sun in an almost transparent way. These neutrinos have been detected with great efforts at terrestrial solar neutrino experiments, which soon raised a tension between the detected and theoretically predicted solar neutrino fluxes. This is the well-known "solar neutrino problem" [18]. The solution of the solar neutrino problem reside in the flavour transition of massive neutrinos in the Sun matter via the Mikheyev-Smirnov-Wolfenstein (MSW) [19–21] mechanism. In this chapter we begin with the introduction of solar neutrinos and their oscillations. After that we provide the model-independent determination of solar neutrino fluxes.

2.1 Introduction to Solar Neutrinos

In this section, we first introduce in Sec. 2.1.1 the mechanisms that produce solar neutrinos and then in Sec. 2.1.2 briefly describe the main solar neutrino experiments which have detected solar neutrinos from high energy ^{8}B neutrinos down to low energy ^{7}Be and even *pp* neutrinos. We then introduce in Sec. 2.1.3

the basics of flavour oscillation of neutrinos in the Sun able to reconcile the observed and the predicted neutrino fluxes.

2.1.1 Proton-proton chain and CNO cycle

We know from the theory of Big Bang Nucleosythesis that there are 75% of hydrogen and 25% of helium in the primordial gas by mass fraction. The Sun, which is formed from primordial gas, is believed to contain 71.0% of hydrogen, 27.1% of helium and the rest are metals [22, 23] (here metals refer to nuclei heavier than helium). Thus the most frequent reactions in the Sun are the fusion of four hydrogen nuclei into one helium nucleus

$$4p \longrightarrow {}^4\mathrm{He} + 2e^+ + 2\nu_e + \gamma \tag{2.1}$$

where the energy released in this process can be approximated by $Q \simeq 4m_p - m_{^4\mathrm{He}} - 2m_e \simeq 26$ MeV. However, the temperature in the solar interior is not high enough to bring four protons close enough for the reaction to happen directly. Most of the time the hydrogen burn into ^{4}He via two set of processes: the proton-proton (*pp*) chain and the carbon-nitrogen-oxygen (CNO) cycle.

As we will describe in Chapter 3 the nuclear rates associated with these two sets of reactions are a fundamental input in the standard modeling of the Sun. With our present knowledge of these nuclear rates the energy provided by the *pp* chain contributes to more than 98% of the solar luminosity. It begins with the process $p + p \to \mathrm{D} + e^+ + \nu_e$. The neutrinos produced by this reaction are referred to as *pp* neutrinos. As a result of the kinematics of e^+ and ν_e, the energy spectrum of *pp* neutrinos is continuous. We see from Table 2.1 that the spectrum is characterized by the maximum energy of 0.423 MeV and average energy of 0.267 MeV. A rare process which contributes to 0.25% of deuterium production is the capture of electrons via $p + e^- + p \to \mathrm{D} + \nu_e$. These neutrinos are referred to as *pep* neutrinos with energy 1.455 MeV. Note that the nuclear matrix elements of *pp* reactions and *pep* reactions are the same. As a consequence, the ratio of *pp* neutrino flux and *pep* neutrino flux is fixed. We shall use this fact in our global fit discussed in the next section. Deuterium in the Sun can only burn into ^{3}He through $\mathrm{D} + p \to^3 \mathrm{He} + \gamma$. No neutrino production is associated with this process. ^{3}He is of course not the end of the story because of its instability. Further nuclear fusions lead to the synthesis of heavier nuclei. There are several mechanisms which terminate the *pp* chain and finally produce ^{4}He as described in reaction (2.1). The first is ^{3}He burn into ^{4}He directly, i.e. ${}^3\mathrm{He} +^3 \mathrm{He} \to^4 \mathrm{He} + 2p$. This is known as *pp*-I and makes up 86% of the terminations. Another mechanism is the formation of ^{7}Be via ${}^3\mathrm{He} +^4 \mathrm{He} \to^7 \mathrm{Be} + \gamma$. Neutrinos are not produced in this process

	Type	Reaction	E_ν^{ave}	E_ν^{max}
	pp	$p + p \to \mathrm{D} + e^+ + \nu_e$	0.2668	0.423
	pep	$p + e^- + p \to \mathrm{D} + \nu_e$	1.455	1.455
		$\mathrm{D} + p \to^3 \mathrm{He} + \gamma$		
pp-I		$^3\mathrm{He} +^3 \mathrm{He} \to^4 \mathrm{He} + 2p$		
pp-II		$^3\mathrm{He} +^4 \mathrm{He} \to^7 \mathrm{Be} + \gamma$		
	^{7}Be	$^7\mathrm{Be} + e^- \to^7 \mathrm{Li} + \nu_e$	0.8631	0.8631
	^{7}Be	$^7\mathrm{Be} + e^- \to^7 \mathrm{Li}^* + \nu_e$	0.3855	0.3855
		$^7\mathrm{Li} + p \to 2^4\mathrm{He}$		
pp-III		$^7\mathrm{Be} + p \to^8 \mathrm{B} + \gamma$		
	^{8}B	$^8\mathrm{B} \to^8 \mathrm{Be}^* + e^+ + \nu_e$	6.735	∼15
		$^8\mathrm{B}^* \to 2^4\mathrm{He}$		
pp-IV	*hep*	$^3\mathrm{He} + p \to^4 \mathrm{He} + e^+ + \nu_e$	9.628	18.778
CNO	^{13}N	$^{13}\mathrm{N} \to^{13} \mathrm{C} + e^+ + \nu_e$	0.7063	1.1982
	^{15}O	$^{15}\mathrm{O} \to^{15} \mathrm{N} + e^+ + \nu_e$	0.9964	1.7317
	^{17}F	$^{17}\mathrm{F} \to^{17} \mathrm{O} + e^+ + \nu_e$	0.9977	1.7364

Table 2.1: Nuclear reactions in the Sun grouped by *pp* chain and CNO cycle [7, 8]. The average neutrino energy E_ν^{ave} and maximum energy E_ν^{max} are in units of MeV. Different types of neutrinos are named after their sources of nuclear reactions.

but ^{7}Be can capture electrons to form ^{7}Li with neutrinos as byproducts, i.e. $^7\mathrm{Be} + e^- \to^7 \mathrm{Li} + \nu_e$. The ground state ^{7}Li is associated with neutrinos of energy 0.862 MeV (branching ratio 89.7%) and the excited $^7\mathrm{Li}^*$ is associated with neutrinos of energy 0.384 MeV (branching ratio 10.3%). ^{7}Be neutrinos are supposed to be monoenergetic since only two particles are produced and neutrinos are nearly massless compared with ^{7}Li . The fusion of ^{7}Li and proton finally produces ^{4}He , which is known as *pp*-II and constitutes 14% of the terminations. In some rare cases (with the probability of 0.015%), ^{7}Be can burn into ^{8}B via $^7\mathrm{Be} + p \to^8 \mathrm{B} + \gamma$ and $^8\mathrm{B} \to^8 \mathrm{Be}^* + e^+ + \nu_e$. Though the ^{8}B neutrino flux is very small compared with *pp* flux or ^{7}Be flux, it is characterized by an energy as high as 15 MeV, making it more accessible to experimental detection. $^8\mathrm{Be}^*$ subsequently decay into two helium nuclei to terminate the *pp*-III chain. Besides these mechanisms, it is theoretically predicted that ^{3}He is able to burn into ^{4}He by proton capture via $^3\mathrm{He} + p \to^4 \mathrm{He} + e^+ + \nu_e$. It is believed that this process constitutes 2×10^{-7} of the terminations and is sometimes referred to as *pp*-IV. The *hep* neutrino flux produced in this process is very small.

On the other hand, the energy provided by CNO cycles only contributes to about 1.5% of the solar luminosity. CNO cycles start with the burning of the most abundant heavy metal, carbon, as ${}^{12}\mathrm{C} + p \rightarrow^{13} \mathrm{N} + \gamma$. ^{13}N will subsequently decays to ^{13}C via ${}^{13}\mathrm{N} \rightarrow^{13} \mathrm{C} + e^{+} + \nu_e$. This process produces ^{13}N neutrinos with maximum energy 1.1982 MeV and average energy 0.7063 MeV. By capturing protons ^{13}C turns into ^{14}N, i.e. ${}^{13}\mathrm{C} + p \rightarrow^{14} \mathrm{N} + \gamma$. A rare process gives birth to ^{15}O and ^{15}O neutrinos, and also terminates the cycle via ${}^{14}\mathrm{N} + p \rightarrow^{15} \mathrm{O} + \gamma$, ${}^{15}\mathrm{O} \rightarrow^{15} \mathrm{N} + e^{+} + \nu_e$, and ${}^{15}\mathrm{N} + p \rightarrow^{12} \mathrm{C} +^{4} \mathrm{He}$. This cycle is known as CNO-I. About 0.1% of the time [8] ^{15}N instead captures protons and makes ^{16}O with the reaction ${}^{15}\mathrm{N} + p \rightarrow^{16} \mathrm{O} + \gamma$. This reaction is responsible for the production of ^{17}F neutrinos via ${}^{16}\mathrm{O} + p \rightarrow^{17} \mathrm{F} + \gamma$ and ${}^{17}\mathrm{F} \rightarrow^{17} \mathrm{O} + e^{+} + \nu_e$. Most frequently this new cycle, known as CNO-II, is terminated by the production of ^{14}N and ^{4}He via ${}^{17}\mathrm{O} + p \rightarrow^{14} \mathrm{N} +^{4} \mathrm{He}$. There may exist other reactions that produce CNO neutrinos, but they are less relevant in the Sun. Just as ^{13}N neutrinos, ^{15}O and ^{17}F neutrinos are also the product of beta decays characterized by continuous spectra with similar maximum and average energies.

As mentioned above, the rates of these reactions are inputs in the construction of Standard Solar Models (SSM's) (see Chapter 3) which in turn predict the spectrum of neutrinos emitted. For example, we show in Fig 2.1.1 the energy spectra of neutrinos from *pp* chains and CNO cycles as predicted by the B16 GS98 model of Ref.[1]. It is clear that *pp* neutrinos dominate the solar neutrino fluxes. However, as a result of the higher energy reach, ^{8}B neutrinos are most likely to fall into the detector sensitivity of solar neutrino experiments. We now briefly describe the experimental results of the direct detection of solar neutrinos.

2.1.2 Solar Neutrino Experiments

Over the past half century and thanks to the development in experimental techniques, we have been able to detect solar neutrinos with better and better precision over an increasing range of neutrino energies. One can classify the solar neutrino experiments in three groups according to their detection technique:

- *Radiochemical experiments*. The pioneering work was conducted by Homestake experiment which detected solar neutrinos by the inverse beta decay of ^{37}Cl via [24]

$$\nu_e +^{37} \mathrm{Cl} \rightarrow^{37} \mathrm{Ar} + e^{-} \,. \tag{2.2}$$

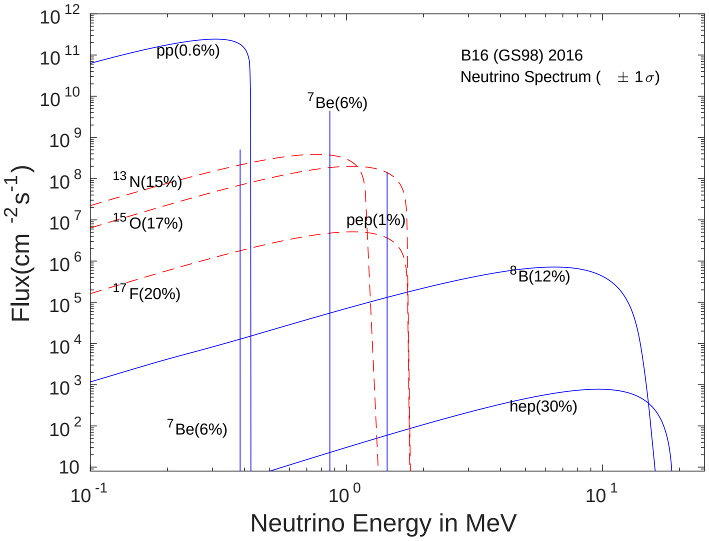

Figure 2.1: The energy spectrum of solar neutrinos as a function of neutrino energy with the uncertainties in the different contributions quoted in the parentheses [1].

The experiment was carried out in the Homestake Gold Mine in Lead, South Dakota. The apparatus consists of 380 m^3 of perchloroethylene (C_2Cl_4) placed deep underground to shield the detector from cosmic rays. The reaction threshold is 0.814 MeV so this experiment can only detect neutrinos with relatively high energies. The ^{37}Ar produced in the detector were collected and counted periodically to obtain the neutrino capture rate. After the operation from 1970 to 1994, Cleveland *et al* [25] report the average event rate:

$$R_{\rm Cl} = 2.56 \pm 0.16 \pm 0.16 \, \rm SNU \, , \tag{2.3}$$

where the unit $1\,\rm SNU = 10^{-36}$captures/atom/sec was introduced by Bahcall [26]. This is about 1/3 the prediction of SSM's. Notice that as only the total rate can be measured the experiment provide no spectral information beyond that of the threshold energy.

Instead of Chlorine, GALLEX/GNO and SAGE experiments made use of neutrino capture by ^{71}Ga target. The reaction responsible for this process is

$$\nu_e +^{71} \rm Ga \to^{71} Ge + e^- \, , \tag{2.4}$$

which is characterized by an energy threshold as 0.233 MeV. The low threshold makes it possible to detect neutrinos from almost the full spectrum, especially *pp* neutrinos which make up the largest portion of solar neutrinos. GALLEX [27] operated from 1991 to 1997 at the Laboratori Nazionali del Gran Sasso (LNGS) in Italy. The detector was filled with 101 tons of $\mathrm{GaCl_3HCl}$ solution which contained 30.3 tons of gallium. After a break, its successor GNO experiment continued running from 1998 to 2003 with the same detector. SAGE [28] used 57 tons of liquid gallium metal deep underground at the Baksan Neutrino Observatory in the Caucasus mountains of Russia. A combined analysis of SAGE and GALLEX/GNO experiments yield the average neutrino capture rate of [29]

$$R_{\mathrm{Ga}} = 68.1 \pm 3.75\,\mathrm{SNU}\,, \tag{2.5}$$

which is about half the prediction of SSM's.

- *Water Cherenkov experiments.* Kamiokande [30] was designed to detect solar neutrinos with the neutrino-electron elastic scattering (ES)

  $$\nu_\alpha + e^- \to \nu_\alpha + e^-\,, \tag{2.6}$$

  where ν_α can be electron, muon or tau neutrinos. The detector was located in the Kamioka mine in Japan, and contained 3000 tons of pure water. The scattered electrons may travel in a speed faster than the velocity of light in water, producing light cones which are called Cherenkov radiation. Kamiokande detector was equipped with 1000 photomultiplier tubes (PMTs) which are able to detect the Cherenkov radiation and reconstruct the neutrino energy and direction. Kamiokande operated from 1987 to 1995 until replaced by the Super-Kamiokande (SK) experiment [31]. The SK detectors were upgraded to contain 50 kilotons of ultrapure water and about 11000 PMTs in the inner detector and about 1900 PMTs in the outer detector. SK experiment has been running for about two decades. From April 1996 to July 2001 was a period called SK-I. The neutrino energy threshold was improved from 6.2 MeV to 4.7 MeV in this period. The experiment resumed in October 2002 and ended in October 2005 with only half of its original number of PMTs. The period was called SK-II. Another SK-III period ran from July 2006 to September 2008 which reduced the energy threshold a little to 4.5 MeV and the SK-IV period began on September 2008. The Kamiokande measured a ^{8}B flux of $(2.80 \pm 0.19 \pm 0.33) \times 10^6\,\mathrm{cm^{-2}s^{-1}}$ and SK obtained the flux of $(2.35 \pm 0.02 \pm 0.08) \times 10^6\,\mathrm{cm^{-2}s^{-1}}$. They are about 40% of the prediction of SSM's.

SNO [32] is another water Cherenkov experiment located in the Creighton mine, near Sudbury, Canada. The detector consists of 1000 tons of ultrapure heavy water and the Cherenkov light is detected by 9456 inward-looking and 91 outward-looking PMTs. Unlike SK experiment, SNO measures the solar neutrinos via three different kinds of reactions: charged current (CC), neutrino current and elastic scattering (ES), i.e.

$$\begin{array}{ll} \text{(CC)} & \nu_e + D \to p + p + e^- \,, \\ \text{(NC)} & \nu_\alpha + D \to p + n + \nu_\alpha \,, \\ \text{(ES)} & \nu_\alpha + e^- \to \nu_\alpha + e^- \,. \end{array} \tag{2.7}$$

The CC, NC and ES reactions are characterized by the neutrino energy threshold of 6.9 MeV, 2.224 MeV and 5.7 MeV respectively and therefore they are measuring also the ^{8}B flux. The SNO experiment underwent three phases from November 2001 with 306.4 live days of data for phase-I, 391.4 live days for the salt phase (phase-II) and 385.2 live days for the NCD phase (phase-III). An analysis of the SNO experiment after the most precise phase-II determined the neutrino fluxes measured in the three reactions [33]

$$\begin{aligned} \Phi_{\rm CC}^{\rm SNO} &= 1.68^{+0.06}_{-0.06}({\rm stat})^{+0.08}_{-0.09}({\rm sys}) \times 10^6\,{\rm cm}^{-2}{\rm s}^{-1}\,, \\ \Phi_{\rm ES}^{\rm SNO} &= 2.35^{+0.22}_{-0.22}({\rm stat})^{+0.15}_{-0.15}({\rm sys}) \times 10^6\,{\rm cm}^{-2}{\rm s}^{-1}\,, \\ \Phi_{\rm NC}^{\rm SNO} &= 4.94^{+0.21}_{-0.21}({\rm stat})^{+0.38}_{-0.34}({\rm sys}) \times 10^6\,{\rm cm}^{-2}{\rm s}^{-1}\,. \end{aligned} \tag{2.8}$$

The results show that while the fluxes measured in CC and ES reactions were about 30% and 40% of the predicted by SSM's, the NC flux was in good agreement with the model prediction. Indeed the ratio of CC and NC fluxes played an important role as test of the particle physics explanation of the observed deficit in solar neutrinos as it is independent of the flux normalization.

- *Scintillator experiments.* In these experiments the target material is liquid scintillator. The incoming solar neutrinos scatter with electrons elastically and the recoiled electrons induce scintillation light in the detector, which is detected by the surrounding PMTs giving information on the deposited energy. Presently the most important of this type of experiment is Borexino [34]. It is an ongoing experiment located at the Laboratori Nazionali del Gran Sasso, Italy. The detector consists of 278 tons of ultrapure liquid scintillator surrounded by 2212 PMTs.

  Borexino began taking data in May 2007. From December 2011 to May

2016 Borexino collaboration launched a run which is called Borexino Phase-II. Recently they announced the first simultaneous precision spectroscopy of *pp*, ^{7}Be and *pep* solar neutrinos [35]. With a multiparameter fit to their observed spectrum and assuming the energy dependence of the different solar neutrino reactions known, they can extract the contribution to their event rates from the different components of the solar flux as (given in captures per day per 100 ton):

$$\begin{aligned} R_{pp} &= 134 \pm 10(\text{stat})^{+6}_{-10}(\text{sys}), \\ R_{^7\text{Be}} &= 48.3 \pm 1.1(\text{stat})^{+0.4}_{-0.7}(\text{sys}) \qquad (2.9) \\ R_{pep} &= 2.43--2.65 \pm 0.36(\text{stat})^{+0.18}_{-0.24}(\text{sys}) \qquad (2.10) \end{aligned}$$

where the range of the R_{pep} spans over uncertainty on the assumed value of the CNO fluxes which were fixed in the analysis.

When compared with the solar model predictions the observed rates show a deficit ranging between 60% for *pp* to about 50% for *pep*.

Most future solar neutrino experiments a belong to the third type of scintillator experiments. An incomplete list of future experiments include the SNO's successor SNO+ [36], JUNO [37], RENO-50 [38], LENA [39], HyperK [40], LENS [41] and ASDC-Theia [42]. While aiming at detecting low energy neutrinos, they may also be expected to search for dark matter and neutrinoless double beta decay.

2.1.3 Flavour Transition for Solar Neutrinos

In the Standard Model there are three species of massless neutrinos characterized by their CC weak interactions: electron neutrinos ν_e, muon neutrinos ν_μ and tau neutrinos ν_τ, which are often referred to as flavor eigenstates. In the model lepton flavour is then conserved by construction. However the results described above from solar neutrino experiments together with those detecting atmospheric neutrinos as well as neutrinos produced in terrestrial sources at reactor and accelerators have convinced us that lepton flavour is not conserved in the propagation of neutrinos and the model has to be extended. The minimal extension able to explain all the confirmed results requires the introduction of masses for the neutrino states so it is possible the misalignment between the neutrino flavor (i.e. interaction) eigenstates and mass eigenstates ν_1, ν_2, ν_3 which are related by

$$|\nu_\alpha\rangle = \sum_i U^*_{\alpha i}|\nu_i\rangle \, , \qquad (2.11)$$

with ν_α as flavor basis and ν_i as mass basis. $U_{\alpha i}$ is the leptonic mixing matrix [43], in similarity with the CKM matrix for quarks. For free neutrinos of momentum p propagation eigenstates are the mass eigenstates so

$$|\nu_i(t)\rangle = e^{-i(E_i t - px)}|\nu_i(0)\rangle \,. \tag{2.12}$$

Neutrinos travel with a speed close to light. In the untrarelativistic limit, we can expand the neutrino energy as

$$E_i = \sqrt{p_i^2 + m_i^2} \simeq p_i + \frac{m_i^2}{2E_i} \,, \tag{2.13}$$

and we are left with

$$|\nu_i(t)\rangle = e^{-i\frac{m_i^2}{2E_i}t}|\nu_i(0)\rangle \,. \tag{2.14}$$

So if neutrinos are produced in a pure eigenstate ν_α and travel a distance L, we can detect them with the same or another neutrino flavor ν_β with the probability

$$\begin{aligned} P_{\alpha\beta} = |\langle\nu_\beta|\nu_\alpha(t)\rangle|^2 = \delta_{\alpha\beta} \quad &- \quad 4\sum_{i>j}\mathrm{Re}(U^*_{\alpha i}U_{\beta i}U_{\alpha j}U^*_{\beta j})\sin^2\left(\frac{\Delta m^2_{ij}L}{4E}\right) \\ &- \quad 2\sum_{i>j}\mathrm{Im}(U^*_{\alpha i}U_{\beta i}U_{\alpha j}U^*_{\beta j})\sin^2\left(\frac{\Delta m^2_{ij}L}{2E}\right), \end{aligned} \tag{2.15}$$

where Eq. (2.11) and (2.14) are applied and $\Delta m^2_{ij} = m_i^2 - m_j^2$ represents the squared mass difference between different mass eigenstates. As most experiments are characterized by some range of L/E, the dominant effect observed comes from one particular mass difference and the flavour transition probability they are most sensitive to can be approximated by the two-neutrino limit where we can simply write

$$P_{\alpha\alpha} = 1 - \sin^2 2\theta \sin^2\left(1.27\frac{\Delta m^2}{\mathrm{eV}^2}\frac{L}{\mathrm{km}}\frac{\mathrm{GeV}}{E}\right) \,, \tag{2.16}$$

and theta is the mixing angle between the two neutrino states. In the 2ν dominance approximation it is physically equivalent to allow Δm^2 to be positive and negative or to allow θ to lie in different octant. It is customary for solar neutrinos to restrict Δm^2 to be positive and choose $0 \leq \theta \leq \pi/2$.

The effects described above are what is defined as neutrino flavour oscillations in vacuum. In some cases, especially for solar neutrinos, neutrinos propagate through dense medium consisting of electrons, protons and neutrons and they can undergo coherent forward scattering with those. As ordinary matter contains electrons but not muons nor taus the scattering amplitudes are different for ν_e than for ν_μ and ν_τ. In the absence of muons and taus, ν_e can interact with solar matter through charged current (CC) interaction while ν_μ and ν_τ cannot. This leads to the modification of the flavour transitions. This effect can be introduced in the evolution equation of the neutrino ensemble in terms of a “matter” potential. For scattering in ordinary matter, we can express the matter potential difference for ν_e's vs the other flavours as

$$V = \sqrt{2} G_{\mathrm{F}} n_e \,, \tag{2.17}$$

where n_e is the electron number density. In the Sun the electron number density decreases from the solar core to the surface approximately as

$$n_e(r) = n_0 e^{-r/r_0} \,, \tag{2.18}$$

where $n_0 = 245\, N_{\mathrm{A}}\, \mathrm{cm}^{-3}$ (N_{A} is the Avogadro constant), $r_0 = 0.1 R_\odot$ ($R_\odot$ is the radius of the Sun) and the relation is valid in the radius $0.1 < r/R_\odot < 0.9$ [8]. Again considering two-flavor neutrino oscillations with electron neutrinos and muon neutrinos only, we can write the admixture of neutrino states as $\boldsymbol{\nu}(x) = \{\nu_e(x), \nu_\mu(x)\}^T$, where $\nu_e(x)$ and $\nu_\mu(x)$ represent the probability amplitude to find electron and muon neutrinos respectively. The flavour evolution of the neutrino ensemble obeys the equation

$$i \frac{d\boldsymbol{\nu}(x)}{dt} = H_m \boldsymbol{\nu}(x) \,, \tag{2.19}$$

where the effective Hamiltonian

$$H_m = \frac{1}{2E} U \begin{pmatrix} m_1^2 & 0 \\ 0 & m_2^2 \end{pmatrix} U^\dagger + \begin{pmatrix} V(x) & 0 \\ 0 & 0 \end{pmatrix} \,, \tag{2.20}$$

and the mixing matrix

$$U = \begin{pmatrix} \cos\theta & \sin\theta \\ -\sin\theta & \cos\theta \end{pmatrix} \,. \tag{2.21}$$

For convenience we define $A \equiv 2EV = 2\sqrt{2} G_{\mathrm{F}} n_e E$. To solve Eq. (2.19) we first diagonalize H_m with matrix U_m and find two eigenvalues

$$\mu_{2,1}^2 = \frac{1}{2} \left[m_1^2 + m_2^2 + A \pm \sqrt{(A - \Delta m^2 \cos 2\theta)^2 + (\Delta m^2 \sin 2\theta)^2} \right] \,. \tag{2.22}$$

They ought to be treated as the new neutrino mass eigenvalues in matter. If the effective potential V was constant, we can proceed to solve Eq. (2.19) and find the survival probability of electron neutrinos

$$P_{ee} = 1 - \sin^2 2\theta_m \sin^2 \left(\frac{(\mu_2^2 - \mu_1^2)L}{4E} \right) , \tag{2.23}$$

with

$$\tan 2\theta_m = \frac{\Delta m^2 \sin 2\theta}{\Delta m^2 \cos 2\theta - A} . \tag{2.24}$$

Eq. (2.23) resembles Eq. (2.16) except that θ and Δm^2 are replaced by the in-medium mixing angle and mass squared difference.

For not constant potential we can define the new mass eigenstates as $\tilde{\boldsymbol{\nu}}(x) = \{\tilde{\nu}_1(x), \tilde{\nu}_2(x)\}^T$ which are the instantaneous eigenvectors of the Hamiltonian. They are not necessarily the original mass eigenstates but depend on time (or traveling distance). After diagonalization of the Hamiltonian we have the equations

$$i\frac{d\boldsymbol{\nu}(x)}{dt} = \frac{1}{2E}\left[U_m \begin{pmatrix} \mu_1^2 & 0 \\ 0 & \mu_2^2 \end{pmatrix} U_m^\dagger \right] \boldsymbol{\nu}(x), \quad \boldsymbol{\nu}(x) = U_m \tilde{\boldsymbol{\nu}}(x) , \tag{2.25}$$

where the in-medium neutrino mixing matrix

$$U_m = \begin{pmatrix} \cos\theta_m & \sin\theta_m \\ -\sin\theta_m & \cos\theta_m \end{pmatrix} . \tag{2.26}$$

It is straightforward to write Eq. (2.25) in terms of the instantaneous mass eigenstates as

$$i\frac{d\tilde{\boldsymbol{\nu}}(x)}{dt} = \left[\frac{1}{2E} \begin{pmatrix} \mu_1^2 & 0 \\ 0 & \mu_2^2 \end{pmatrix} - iU_m^\dagger(x)\frac{dU_m(x)}{dx}\right] \tilde{\boldsymbol{\nu}}(x) . \tag{2.27}$$

Because of the second term, Eq. (2.27) is not diagonal, which means that the instantaneous mass eigenstates are not the eigenstates of the evolution. This leads to the possible violation of adiabaticity in the evolution. If θ_m varies slowly with time, the second term in the square bracket can be ignored. This is the adiabatic condition which is often satisfied in the Sun. If this is the case, we may continue to solve Eq. (2.27) and obtain the electron neutrino survival probability

$$\begin{aligned} P_{ee} &= \frac{1}{2}[1+\cos 2\theta_m(L)\cos 2\theta_m(0)] \\ &+ \frac{1}{2}\sin 2\theta_m(L)\sin 2\theta_m(0)\cos\left[\int_0^L \frac{\mu_2^2(x)-\mu_1^2(x)}{2E}dx\right]\,. \end{aligned} \tag{2.28}$$

Since the energy spectra of neutrinos are continuous and the detected neutrino fluxes are averaged over energy and integrated over large L, the last term in Eq. (2.28) averages out in any solar neutrino experiment provided Δm^2 is above 10^{-10} eV^2. So finally we have

$$\langle P_{ee}\rangle = \frac{1}{2}[1+\cos 2\theta_m(L)\cos 2\theta_m(0)]\,. \tag{2.29}$$

From Eq. (2.24) we see that for a given value of $\Delta m^2\cos 2\theta$ and energy E there is a potential for which the denominator of Eq. (2.24) vanishes. This is usually referred to as the resonance potential. At this value of the potential the mixing angle in matter becomes maximal ($\theta_m = \pi/4$) independently of its value in vacuum and for matter potentials well above this resonance value the mixing in matter becomes $\pi/2$, this is there is a full reversal of the flavour composition. This is the so-called MSW effect [19–21]. For example for a neutrino produced in the core of the Sun and for $\tan^2\theta \sim 0.5$ and $\Delta m^2 \sim 8\times 10^{-5}$eV^2 (which are the parameters which eventually better describe the full data)

$$E_{\rm res} = \frac{\Delta m^2\cos 2\theta}{2\sqrt{2}G_{\rm F}n_e(0)} \simeq 1.75\,{\rm MeV}\,. \tag{2.30}$$

Notice also that since A is positive, the cancellation of the denominator of Eq. (2.24) can only happens for the first octant of θ (in the used convention of positive Δm^2), breaking the symmetry of the vacuum survival probability about $\pi/4$.

Altogether the final result of the matter effects on the neutrino evolution depend on the relation between $\Delta m^2\cos 2\theta$ and A:

- If $\Delta m^2\cos 2\theta \gg A_0$ where A_0 is taken at the neutrino production point (in the solar core), the matter effects can always be neglected. With what we know of θ and Δm^2 this applies to *pp* neutrinos and ^{7}Be neutrinos whose maximum energies are below $E_{\rm res}$. In this case the averaged survival probability of electron neutrinos

$$\langle P_{ee}\rangle = 1-\frac{1}{2}\sin^2 2\theta\,, \tag{2.31}$$

where the average over L/E is applied. The minimum survival probability 0.5 is reached when $\theta = \frac{\pi}{4}$.

- If $\Delta m^2 \cos 2\theta \gtrsim A_0$, the resonance condition $\Delta m^2 \cos 2\theta = A$ is never realized in the neutrino trajectory since the electron number density decreases from the solar core to the surface. As a consequence, the averaged survival probability is not different from Eq. (2.29), i.e.

$$\langle P_{ee} \rangle = \frac{1}{2}[1 + \cos 2\theta \cos 2\theta_m(0)] \,. \tag{2.32}$$

  We don't expect neutrinos to go through dense medium at the detector, thus the in-medium mixing angle $\theta(L)$ is just the vacuum mixing angle θ. This result can be interpreted intuitively. When electron neutrinos are created at the solar core they consist of $\cos^2\theta_m(0)$ fraction of $\tilde{\nu}_1$ and $\sin^2\theta_m(0)$ fraction of $\tilde{\nu}_2$. Neutrinos stay in their new mass eigenstates until they exit the Sun, when a fraction of $\cos^2\theta$ of $\tilde{\nu}_1$ and a fraction of $\sin^2\theta$ of $\tilde{\nu}_2$ contribute to the total electron neutrino fluxes. As a result, we expect $\langle P_{ee} \rangle = \cos^2\theta_m(0)\cos^2\theta + \sin^2\theta_m(0)\sin^2\theta$, which is just Eq. (2.32) above.

- If $\Delta m^2 \cos 2\theta \lesssim A_0$ the resonance condition will be inevitably satisfied in the way when neutrinos travel outside the Sun. It turns out that for the whole energy spectra of solar neutrinos the resonance condition is always crossed adiabatically [17]. Therefore Eq. (2.32) still holds to describe the survival probability of electron neutrinos.

- If $\Delta m^2 \cos 2\theta \ll A_0$, one finds $\theta_m \simeq \frac{\pi}{2}$ from Eq. (2.24) when A is large enough. In this case we have

$$\langle P_{ee} \rangle = \frac{1}{2}(1 - \cos 2\theta) = \sin^2\theta \,, \tag{2.33}$$

  Assuming $\tan^2\theta \sim 0.5$ we arrive at $\langle P_{ee} \rangle \simeq \frac{1}{3}$, which explains the deficit of ^{8}B neutrinos detected at SNO and SK experiments.

Finally let us mention the KamLAND [44] experiment, a non-solar neutrino experiment but which yields information on ν_e (indeed reactor $\bar{\nu}_e$) survival probability in vacuum relevant for the same ranges of Δm^2 and θ. By measuring the spectrum of reactor neutrinos produced at an average distance of 180 km, KamLAND confirmed the flavour vacuum oscillation of $\bar{\nu}_e$ with values of Δm^2 and θ which are consistent with those required for better description of the solar neutrino results in terms of MSW matter transitions. This solar model independent determination of the oscillation parameters allows then to use the solar neutrino results to determine directly from the experiment the values of the different components of the unoscillated solar neutrino fluxes as we describe in the next section.

Before closing this section we have to point out that the probabilities described above are given in the two-neutrino state approximation. However we know that to globally describe the results of neutrino experiments performed with atmospheric neutrinos as well as neutrinos from reactors and accelerators we need to consider the mixing between the three neutrino flavours. In the usual parametrization of the 3ν mixing the solar and KamLAND experiments dominantly determine the parameters Δm^2_{21} and θ_{12} while experiments measuring atmospheric and long baseline accelerator neutrinos mainly determine $|\Delta m^2_{32}|$ and θ_{23} while reactor experiments performed at km baselines determine $|\Delta m^2_{32}|$ and θ_{13}. Furthermore the results are such that $\Delta m^2_{21} \ll |\Delta m^2_{32}| \simeq |\Delta m^2_{31}|$. Because of this hierarchy in the mass splittings, the relevant survival probabilities for solar and KamLAND neutrinos can be precisely approximated as

$$P_{ee} = \cos^4\theta_{13}\, P^{2\nu}_{ee}(\Delta m^2_{12}, \theta_{12}) \,+\, \sin^4\theta_{23} \tag{2.34}$$

where $P^{2\nu}_{ee}$ is given by the 2-ν expressions above but with a modified matter potential $V = \cos^2\theta_{13}\sqrt{2}G_{\rm F}n_e$ [45].

2.2 Solar Neutrino Flux Determination: Methodology

We have discussed the solar neutrino problem extensively in the previous section. It has now been fully solved by neutrino oscillations and matter effects in the neutrino propagation. And with the upcoming of more and better experiments we have been able to determine the neutrino oscillation parameters with better and better precision.

However, in parallel to the increased precision in our understanding of neutrino propagation, a new puzzle emerged in the consistency of SSMs [46] (see Sec. 3.1 for detailed descriptions of SSMs). SSMs built in the 1990's were very successful in predicting other observations. In particular, quantities measured by helioseismology such as the radial distributions of sound speed and density [47–50] showed good agreement with the predictions of the SSM calculations and provided accurate information about the solar interior. A key element to this agreement was the input value of the abundances of heavy elements on the surface of the Sun [10]. However, since 2004 new determinations of these abundances became available, pointing towards substantially lower values [11, 51]. The SSMs based on such lower metallicities fail at explaining the helioseismic observations [46]. This led to the construction of two different sets of SSMs, one based on the older solar abundances [10] generically referred to as "GS98" models implying high metallicity, and one assuming lower metallicity as inferred from the more recent determinations of the solar abundances [11, 51] referred to as "AGSS09" models. The two variant of models lead, in general, to somewhat different prediction for the solar neutrino fluxes.

We will go back to the issue of improvements in the solar modeling in Chapter 3. In here we aim at circumventing the use of solar models by directly determining the solar neutrino spectrum from the solar neutrino experimental results. The basic assumption is that the energy dependence of the neutrinos produced in each of the eight nuclear reactions is well determined by well known kinematics thus the full spectrum can be parametrized in terms of the normalizaiton of the eight components. Furthermore the deconvoluion of the unoscillated fluxes from the measured oscillated rates is possible because the relevant oscillation parameters are determined independently by non-solar experiments, this is, the energy dependence of the survival probability is independently known.

So what we present next is the results of a solar model independent analysis of the solar and terrestrial neutrino data in the framework of three-neutrino masses and mixing, aiming at simultaneously determine the flavor parameters and all the solar neutrino fluxes with a minimum set of theoretical priors. We begin with the introduction in Sec. 2.2.1 of the basics of Bayesian statistics which we use in the analysis and describe the framework of the analysis and the relevant prior constraints imposed in Sec. 2.2.2. The results of the analysis will be presented in Sec. 2.3 and they are based on our published work Ref. [52].

2.2.1 Brief Introduction to Bayesian Statistics

Bayesian inference methods provide a consistent approach to the estimation of a set of parameters $\boldsymbol{\Theta}$ in a model M for the data $\boldsymbol{D}$. Bayes' theorem states that under the assumption that a model M is true, complete inference of its parameters is given by the posterior distribution,

$$\Pr(\boldsymbol{\Theta}|\boldsymbol{D}, M) = \frac{\Pr(\boldsymbol{D}|\boldsymbol{\Theta}, M)\Pr(\boldsymbol{\Theta}|M)}{\Pr(\boldsymbol{D}|M)} = \frac{\mathcal{L}(\boldsymbol{\Theta})\pi(\boldsymbol{\Theta})}{\mathcal{Z}}, \tag{2.35}$$

where $\mathcal{L}(\boldsymbol{\Theta}) \equiv \Pr(\boldsymbol{D}|\boldsymbol{\Theta}, M)$ is the *likelihood function.* The prior probability density of the parameters is given by $\pi(\boldsymbol{\Theta}) \equiv \Pr(\boldsymbol{\Theta}|M)$, and should always be normalized, i.e., it should integrate to unity. Conversely the *evidence*, $\mathcal{Z}_i = \Pr(\boldsymbol{D}|M_i)$, is the likelihood for the model quantifying how well the model

$\lvert\ln(\mathcal{B}_{ij})\rvert$	Strength of Evidence
< 1.0	Inclusive
1.0–2.5	Weak to Moderate
2.5–5	Moderate to Strong
> 5.0	Strong to Very Strong/Decisive

Table 2.2: Jeffrey's scale for interpretation of the Bayes factors

describes the data. It is given by

$$\mathcal{Z} = \int \mathcal{L}(\boldsymbol{\Theta})\pi(\boldsymbol{\Theta})d\boldsymbol{\Theta} \,. \tag{2.36}$$

From the posterior distribution one can construct reparametrization invariant Bayesian credible intervals by defining the "credible level" of a value $\eta = \eta_0$ of a subset of parameters simply as the posterior volume within the likelihood of that value,

$$\mathrm{CL}(\eta_0) = \int_{\mathcal{L}(\eta)>\mathcal{L}(\eta_0)} \Pr(\eta|\boldsymbol{D})\mathrm{d}\eta. \tag{2.37}$$

This function can be converted to the "number of σ's" in the usual manner as

$$S = \sqrt{2}\mathrm{erfc}^{-1}(1 - \mathrm{CL}). \tag{2.38}$$

Bayesian statistics is mostly suited to make a *relative* statement about the plausibility of a given model M_i versus another M_j by comparing their respective posterior probabilities. This is quantified by means of the Bayes factor

$$\mathcal{B}_{ij} = \frac{\mathcal{Z}_i}{\mathcal{Z}_j} \tag{2.39}$$

which is the ratio of the evidences. Jeffrey's scale is often used for the interpretation of the Bayes factors (see Table 2.2.1). This gives what the ratio of posterior probabilities for the models would be if the overall prior probabilities for the two models were equal. Or in other words it shows by how much the probability ratio of model M_i to model M_j changes in the light of the data, and thus can be viewed as a numerical measure of evidence supplied by the data in favour of one hypothesis over the other.

It is also possible to make an *absolute* test of significance of a given model M by using the prior predictive distribution, which is to be understood as a distribution of the possible observable outputs $\boldsymbol{\mathcal{O}}$,

$$\Pr(\boldsymbol{\mathcal{O}}) = \int \Pr(\boldsymbol{\mathcal{O}}|\boldsymbol{\Theta})\pi(\boldsymbol{\Theta})\mathrm{d}^N\boldsymbol{\Theta} \tag{2.40}$$

to determine the probability distribution function for some statistics $\mathcal{T}(\boldsymbol{\mathcal{O}})$ and compare it with what was actually observed. This would be done as usual by calculating the p-value

$$p = \Pr(\mathcal{T}(\boldsymbol{\mathcal{O}}) \geq \mathcal{T}(\boldsymbol{\mathcal{O}}^{\mathrm{dat}})) \tag{2.41}$$

In this work we use MultiNest [53–55], a Bayesian inference tool which, given the prior and the likelihood, calculates the evidence with an uncertainty estimate, and generates posterior samples from distributions that may contain multiple modes and pronounced (curving) degeneracies in high dimensions.

2.2.2 Analysis Framework

In the analysis of solar neutrino experiments we include the total rates from the radiochemical experiments Chlorine [25], Gallex/GNO [56] and SAGE [57]. For real-time experiments we include the results on electron scattering (ES) from the four phases in Super-Kamiokande: the 44 data points of the phase I (SK1) energy-zenith spectrum [58], the 33 data points of the full energy and day/night spectrum in phase II (SK2) [59], the 42 energy and day/night data points in phase III (SK3) [60], and the 24 data points of the energy spectrum and day-night asymmetry of the 1669-day of phase IV (SK4) [61]. The results of the three phases of SNO are included in terms of the parametrization given in their combined analysis [62] which amount to 7 data points. We also include the main set of the 740.7 days of Borexino Phase-1 data [63, 64] as well as their high-energy spectrum from 246 live days [65] and the 408 days of Borexino Phase-2 data [66]. In the framework of three neutrino masses and mixing the expected values for these solar neutrino observables depend on the parameters Δm^2_{21}, θ_{12}, and θ_{13} as well as on the normalizations of the eight solar fluxes.

Besides solar experiments, we also include the observed energy spectrum in KamLAND data sets DS-1 and DS-2 [44] with a total exposure of 3.49×10^{32} target-proton-year (2135 days), which in the framework of three neutrino mixing also yield information on the parameters Δm^2_{21}, θ_{12}, and θ_{13}.

In addition, we include the information on θ_{13} obtained after marginalizing over $\Delta m^2_{3\ell}$, θ_{23} and δ_{CP} the results of all the other oscillation experiments considered in the NuFIT-2.0 analysis presented in Refs. [3, 67, 68]. In particular this accounts for Super-Kamiokande atmospheric neutrino data from phases

Flux	$\Phi_i^{\rm ref}$ [cm^{-2} s^{-1}]	α_i [MeV]	β_i
pp	5.98×10^{10}	13.0987	9.186×10^{-1}
^{7}Be	5.00×10^{9}	12.6008	7.388×10^{-2}
pep	1.44×10^{8}	11.9193	2.013×10^{-3}
^{13}N	2.96×10^{8}	3.4577	1.200×10^{-3}
^{15}O	2.23×10^{8}	21.570	5.641×10^{-3}
^{17}F	5.52×10^{6}	2.3630	1.530×10^{-5}
^{8}B	5.58×10^{6}	6.6305	4.339×10^{-5}
hep	8.04×10^{3}	3.7370	3.523×10^{-8}

Table 2.3: The reference neutrino flux $\Phi_i^{\rm ref}$ (the SFII-GS98 model of Ref. [2]) used for normalization, the energy α_i provided to the star by nuclear fusion reactions associated with the $i^{\rm th}$ neutrino flux (taken from Ref. [9]), and the fractional contribution β_i of the $i^{\rm th}$ nuclear reaction to the total solar luminosity.

SK1–4 [69] (with addition of the 1775 days of phase SK4 over their published results on phases SK1–3 [70]); the energy distribution of long baseline neutrinos from MINOS in both ν_μ and $\bar{\nu}_\mu$ disappearance with 10.71×10^{20} and 3.36×10^{20} pot, respectively, as well as from T2K in ν_μ disappearance [71] with 6.57×10^{20} pot; LBL appearance results from MINOS [72] with exposure 10.6×10^{20} (ν_e) and 3.3×10^{20} ($\bar{\nu}_e$) pot, and from T2K with 6.57×10^{20} pot (ν_e) [73]; reactor data from the finalized experiments CHOOZ [74] and Palo Verde [75] together with the spectrum from Double Chooz with 227.9 days live time [76], and the 621-day spectrum from Daya Bay [77], as well as the near and far rates observed at RENO with 800 days of data-taking [78].

In what follows, for convenience, we will use as normalization parameters for the solar fluxes the reduced quantities:

$$f_i = \frac{\Phi_i}{\Phi_i^{\rm ref}} \tag{2.42}$$

with $i =$ pp, ^{7}Be, pep, ^{13}N, ^{15}O, ^{17}F, ^{8}B, and hep. The numerical values of $\Phi_i^{\rm ref}$ are set to the predictions of the SFII-GS98 solar model as given in Ref. [2] and are listed in Table 2.3. With this, the theoretical predictions for the relevant observables (after marginalizing over Δm^2_{23}, θ_{23} and $\delta_{\rm CP}$) depend on eleven parameters: the three relevant oscillation parameters Δm^2_{21}, θ_{12}, θ_{13} and the eight reduced solar fluxes f_i. With the data and the theoretical predictions for them in terms of these parameters $\boldsymbol{\omega} = (\Delta m^2_{21}, \theta_{12}, \theta_{13}, f_{\rm pp}, \dots, f_{\rm hep})$ we build the corresponding likelihood function

$$-2\ln\mathcal{L}(\boldsymbol{\omega}) = \sum_{i,j} \frac{(\mathcal{O}_i(\boldsymbol{\omega}) - \mathcal{O}_i^{\rm dat})}{\sigma_i^{\rm dat}} (\rho^{\rm dat})^{-1}_{ij} \frac{(\mathcal{O}_j(\boldsymbol{\omega}) - \mathcal{O}_j^{\rm dat})}{\sigma_j^{\rm dat}} \tag{2.43}$$

where $\mathcal{O}_i(\boldsymbol{\omega})$ are the predicted values of the observables as a function of the 11 parameters.

In our model-independent analysis we assume a uniform prior probability complemented by a set of constraints to ensure consistency in the *pp*-chain and CNO-cycle, as well as some relations from nuclear physics. Specifically, we impose the following restrictions:

- The fluxes must be positive:

$$\Phi_i \geq 0 \quad \Rightarrow \quad f_i \geq 0\,. \tag{2.44}$$

- The number of nuclear reactions terminating the *pp*-chain should not exceed the number of nuclear reactions which initiate it [9, 79]:

$$\begin{aligned}&\Phi_{^7\rm Be} + \Phi_{^8\rm B} \leq \Phi_{\rm pp} + \Phi_{\rm pep}\\ &\quad \Rightarrow \quad 8.49\times10^{-2} f_{^7\rm Be} + 9.95\times10^{-5} f_{^8\rm B} \leq f_{\rm pp} + 2.36\times10^{-3} f_{\rm pep}\,.\end{aligned} \tag{2.45}$$

- The $^{14}{\rm N}(p,\gamma)^{15}{\rm O}$ reaction must be the slowest process in the main branch of the CNO-cycle [79]:

$$\Phi_{^{15}\rm O} \leq \Phi_{^{13}\rm N} \quad \Rightarrow \quad f_{^{15}\rm O} \leq 1.34 f_{^{13}\rm N} \tag{2.46}$$

  and the CNO-II branch must be subdominant:

$$\Phi_{^{17}\rm F} \leq \Phi_{^{15}\rm O} \quad \Rightarrow \quad f_{^{17}\rm F} \leq 37 f_{^{15}\rm O}\,. \tag{2.47}$$

- The ratio of the pep neutrino flux to the pp neutrino flux is fixed to high accuracy because they have the same nuclear matrix element. We have constrained this ratio to match the average of the SFII GS98 and AGSS09 model values, with 1σ Gaussian uncertainty given by the difference between the values in the two models[1]

$$\frac{f_{\rm pep}}{f_{\rm pp}} = 1.006 \pm 0.013\,. \tag{2.48}$$

---

[1] We have verified that assuming a flat distribution over the 1σ uncertainty interval does not produce significant differences in the results of our analysis.

The number of independent fluxes is reduced when imposing the so-called "luminosity constraint", *i.e.*, the requirement that the sum of the thermal energy generation rates associated with each of the solar neutrino fluxes coincides with the solar luminosity [80]:

$$\frac{L_\odot}{4\pi\,(\text{A.U.})^2} = \sum_{i=1}^{8} \alpha_i \Phi_i\,. \tag{2.49}$$

Here the constant α_i is the energy provided to the star by the nuclear fusion reactions associated with the i^{th} neutrino flux; its numerical value is independent of details of the solar model to an accuracy of one part in 10^4 or better [9]. A detailed derivation of this equation and the numerical values of the coefficients α_i, which we reproduce for convenience in Table 2.3, is presented in Ref. [9]. In terms of the reduced fluxes Eq. (2.49) can be written as:

$$1 = \sum_{i=1}^{8} \beta_i f_i \quad \text{with} \quad \beta_i \equiv \frac{\alpha_i \Phi_i^{\text{ref}}}{L_\odot \big/ [4\pi\,(\text{A.U.})^2]} \tag{2.50}$$

where β_i is the fractional contribution to the total solar luminosity of the nuclear reactions responsible for the production of the Φ_i^{ref} neutrino flux, and $L_\odot \big/ [4\pi\,(\text{A.U.})^2] = 8.5272 \times 10^{11}\,\text{MeV}\,\text{cm}^{-2}\,\text{s}^{-1}$ [9]. The analysis performed incorporating the priors in Eqs. (2.44–2.49) will be named "analysis with luminosity constraint", $\mathcal{P} = L_\odot$, and for this case the prior probability distribution is:

$$\pi(\boldsymbol{\omega}'|L_\odot) = \begin{cases} \dfrac{1}{N} \exp\left[-\dfrac{\big(f_{\text{pep}}/f_{\text{pp}} - 1.006\big)^2}{2\sigma^2} \right] & \text{if Eqs. (2.44–2.47) and (2.49) are verified,} \\ 0 & \text{otherwise,} \end{cases} \tag{2.51}$$

where N is a normalization factor and $\sigma = 0.010$. When only Eqs. (2.44–2.48) are imposed we will speak of "analysis without luminosity constraint", $\mathcal{P} = \not{L}_\odot$, so:

$$\pi(\boldsymbol{\omega}'|\not{L}_\odot) = \begin{cases} \dfrac{1}{N} \exp\left[-\dfrac{\big(f_{\text{pep}}/f_{\text{pp}} - 1.006\big)^2}{2\sigma^2} \right] & \text{if Eqs. (2.44–2.47) are verified,} \\ 0 & \text{otherwise.} \end{cases} \tag{2.52}$$

Let us notice that the conditions in Eqs. (2.44–2.47) and Eq. (2.49) are constraints on some linear combinations of the solar fluxes and they are model independent, *i.e.*, they do not impose any prior bias favoring either of the SSMs. Furthermore we have chosen to center the condition (2.48) at the average of the SFII GS98 and AGSS09 values, with 1σ Gaussian uncertainty given by the difference between the values in the two models, to avoid the introduction of a bias towards one of the models. In the next sections we will comment on how our results are affected when this prior is centered about the GS98 or the AGSS09 prediction.

2.3 Determination of Solar Neutrino Flux: Results

We are now ready to present the results of our multiparameter global analysis. We will first discuss in Sec. 2.3.1 the solar fluxes extracted within the luminosity constraint, Eq. (2.49). We then release this constraint in Sec. 2.3.2 which allows for directly determining the amount of solar energy produced in the *pp*-chain and the CNO-cycle. The directly determined solar neutrino fluxes can also be used to assess the two SSMs, and to forecast the experimental sensitivity needed to discriminate between them with future solar neutrino experiments as described in Sec. 2.3.3.

2.3.1 Solar Neutrino Flux with Luminosity Constraint

Our results for the analysis with luminosity constraint are displayed in Fig. 2.2, where we show the marginalized one-dimensional probability distributions $\Pr(f_i|\mathbf{D}, L_\odot)$ for the eight solar neutrino fluxes as well as the 90% and 99% CL two-dimensional allowed regions. The corresponding ranges at 1σ (and at the 99% CL in square brackets) on the oscillation parameters are:

$$\begin{aligned} \Delta m^2_{21} &= 7.5 \pm 0.2\,[^{+0.4}_{-0.5}] \times 10^{-5}\ \text{eV}^2\,, \\ \sin^2\theta_{12} &= 0.30 \pm 0.01\,[^{+0.04}_{-0.03}]\,, \\ \sin^2\theta_{13} &= 0.022 \pm 0.001\,[^{+0.002}_{-0.003}]\,. \end{aligned} \tag{2.53}$$

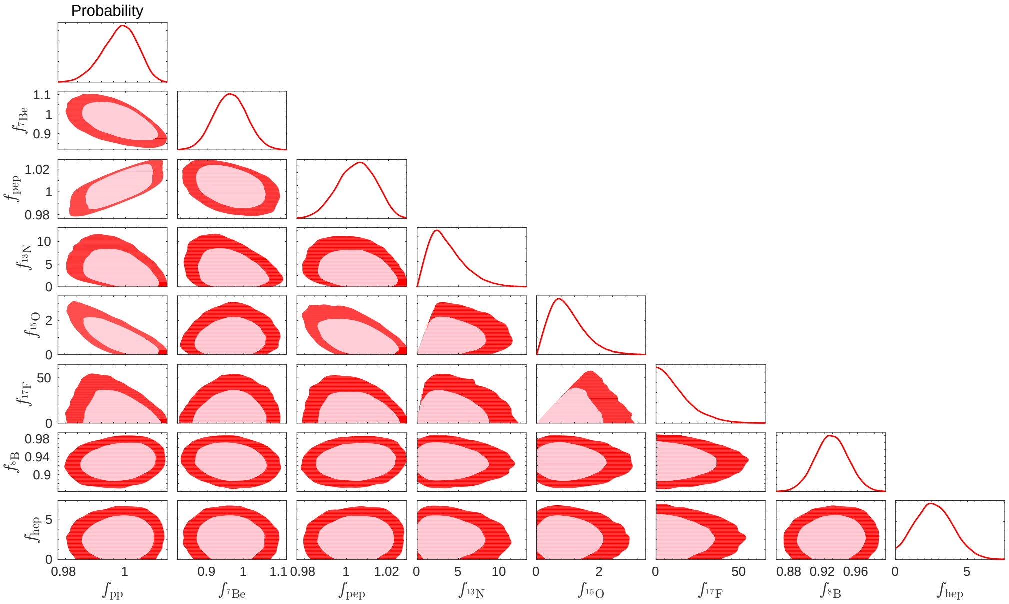

Figure 2.2: Constraints from our global analysis on the solar neutrino fluxes. The curves in the right-most panels show the marginalized one-dimensional probability distributions. The rest of the panels show the 90% and 99% CL two-dimensional credibility regions (see text for details).

while for the solar neutrino fluxes we get:

$$\begin{aligned}
f_{\text{pp}} &= 0.999^{+0.006}_{-0.005}\,\left[{}^{+0.012}_{-0.016}\right], & \Phi_{\text{pp}} &= 5.971^{+0.037}_{-0.033}\left[{}^{+0.073}_{-0.097}\right] \times 10^{10}\ \text{cm}^{-2}\ \text{s}^{-1}\,, \\
f_{^7\text{Be}} &= 0.96^{+0.05}_{-0.04}\,\left[{}^{+0.12}_{-0.11}\right], & \Phi_{^7\text{Be}} &= 4.80^{+0.24}_{-0.22}\,\left[{}^{+0.60}_{-0.57}\right] \times 10^{9}\ \text{cm}^{-2}\ \text{s}^{-1}\,, \\
f_{\text{pep}} &= 1.005 \pm 0.009\,\left[{}^{+0.019}_{-0.024}\right], & \Phi_{\text{pep}} &= 1.448 \pm 0.013\,\left[{}^{+0.028}_{-0.034}\right] \times 10^{8}\ \text{cm}^{-2}\ \text{s}^{-1}\,, \\
f_{^{13}\text{N}} &= 1.7^{+2.9}_{-1.0}\,\left[{}^{+8.4}_{-1.6}\right], & \Phi_{^{13}\text{N}} &\le 13.7\,[30.2] \times 10^{8}\ \text{cm}^{-2}\ \text{s}^{-1}\,, \\
f_{^{15}\text{O}} &= 0.6^{+0.6}_{-0.4}\,\left[{}^{+2.0}_{-0.6}\right], & \Phi_{^{15}\text{O}} &\le 2.8\,[5.8] \times 10^{8}\ \text{cm}^{-2}\ \text{s}^{-1}\,, \\
f_{^{17}\text{F}} &\le 15\,[46]\,, & \Phi_{^{17}\text{F}} &\le 8.5\,[25] \times 10^{7}\ \text{cm}^{-2}\ \text{s}^{-1}\,, \\
f_{^8\text{B}} &= 0.92 \pm 0.02\,[\pm 0.05]\,, & \Phi_{^8\text{B}} &= 5.16^{+0.13}_{-0.09}\,\left[{}^{+0.30}_{-0.26}\right] \times 10^{6}\ \text{cm}^{-2}\ \text{s}^{-1}\,, \\
f_{\text{hep}} &= 2.4^{+1.5}_{-1.2}\,[\le 5.9]\,, & \Phi_{\text{hep}} &= 1.9^{+1.2}_{-0.9}\,[\le 4.7] \times 10^{4}\ \text{cm}^{-2}\ \text{s}^{-1}\,.
\end{aligned} \tag{2.54}$$

We notice that with the exception of ^{17}F all other fluxes have a vanishing (or close to) probability for their corresponding $f = 0$. However, it is important to stress that for what concerns $f_{^{13}\text{N}}$ and $f_{^{15}\text{O}}$ this is mostly consequence of the inequalities in Eqs. (2.46) and (2.47), which effectively result into priors behaving as $\pi(f_i) \propto f_i$ for small f_i. For this reason the corresponding 1σ credible intervals for these fluxes, constructed as iso-posterior intervals and shown in the left column of Eq. (2.54), do not extend to $f_i = 0$ even though setting $f_{^{13}\mathrm{N}} = f_{^{15}\mathrm{O}} = f_{^{17}\mathrm{F}} = 0$ gives a reasonable fit to the data. With this in mind, in the right column in Eq. (2.54) we have chosen to quote only the 1σ and 99%CL upper boundaries for the corresponding solar neutrino fluxes, rather than the complete allowed range.

As mentioned above we have checked the stability of the results under changes in the assumption of the Gaussian prior in Eq. (2.48). We find that if we center this prior at the SFII-GS98 prediction ($f_{\mathrm{pep}}/f_{\mathrm{pp}} = 1$) the best fit value for pep neutrinos is changed to $f_{\mathrm{pep}} = 0.998$ ($\Phi_{\mathrm{pep}} = 1.437 \times 10^8\,\mathrm{cm}^{-2}\,\mathrm{s}^{-1}$), while if we center it at the SFII-AGSS09 prediction ($f_{\mathrm{pep}}/f_{\mathrm{pp}} = 1.013$) we get $f_{\mathrm{pep}} = 1.012$ ($\Phi_{\mathrm{pep}} = 1.457 \times 10^8\,\mathrm{cm}^{-2}\,\mathrm{s}^{-1}$). All other fluxes are unaffected.

As seen in Fig. 2.2 the most important correlation appears between the pp and pep fluxes, as expected from the relation (2.48). The correlation between the pp (and pep) and ^{7}Be flux is directly dictated by the luminosity constraint (see comparison with Fig. 2.3). All these results imply the following share of the energy production between the *pp*-chain and the CNO-cycle

$$\frac{L_{\text{pp-chain}}}{L_\odot} = 0.991^{+0.005}_{-0.004}\,{}^{[+0.008]}_{[-0.013]} \quad \Longleftrightarrow \quad \frac{L_{\text{CNO}}}{L_\odot} = 0.009^{+0.004}_{-0.005}\,{}^{[+0.013]}_{[-0.008]}\,, \qquad (2.55)$$

in perfect agreement with the SSMs which predict $L_{\text{CNO}}/L_\odot \leq 1\%$ at the 3σ level. Note that the same comment as on the $f_{^{13}\mathrm{N}}$ and $f_{^{15}\mathrm{O}}$ fluxes applies to the total CNO luminosity, so we can understand the result in Eq. (2.55) effectively as an upper bound on the contribution of the CNO-cycle to the Sun Luminosity: $L_{\text{CNO}}/L_\odot \leq 2.2\%$ at 99% CL.

2.3.2 Testing the Luminosity Constraint

In order to check the consistency of our results we have performed the same analysis without imposing the luminosity constraint, Eq. (2.49). The corresponding results for $\Pr(f_i|\mathbf{D}, \not{L}_\odot)$ and the two-dimensional allowed regions are shown in Fig. 2.3. As expected, the pp flux is the most affected by the release of this constraint. This is so because the pp reaction gives the largest contribution to the solar energy production, as can be seen in Table 2.3. Hence, using the luminosity constraint only as an upper bound would imply that the pp flux cannot exceed its SSM prediction by more than 9%, while completely removing this constraint allows for a much larger pp flux. The pep flux is also severely affected due to its strong correlation with the pp flux, Eq. (2.48). On a smaller scale the CNO fluxes are also affected, mainly as an indirect effect due to the modified contribution of the pp and pep fluxes to the Gal-

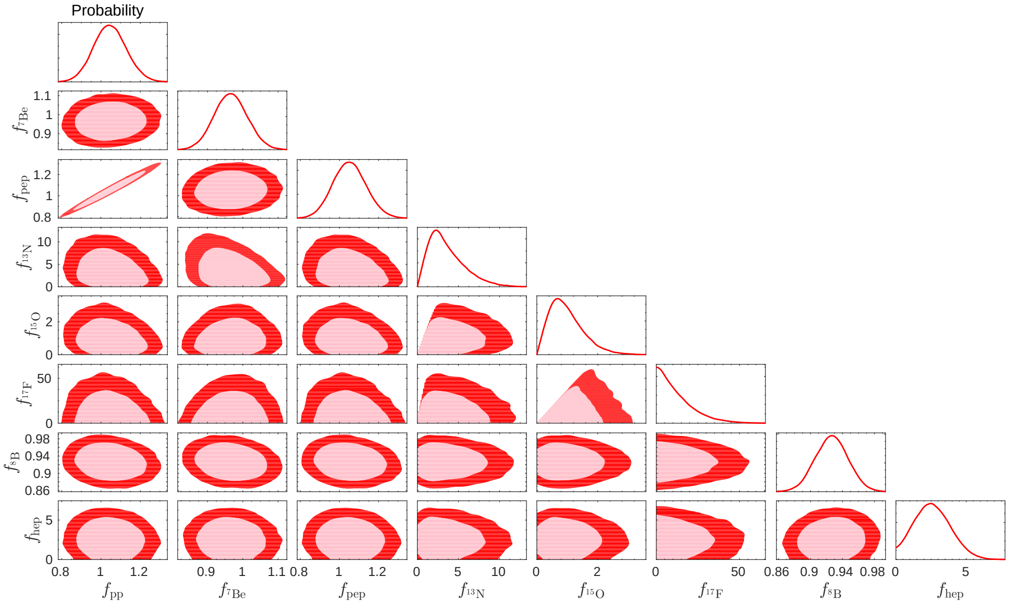

Figure 2.3: Same as Fig. 2.2 but without the luminosity constraint, Eq. (2.49).

lium and Chlorine experiments, which leads to a change in the allowed CNO contribution to these experiments. Thus in this case we get:

$$\begin{aligned}
f_{\mathrm{pp}} &= 1.04 \pm 0.08\,[^{+0.22}_{-0.20}]\,,\\
f_{^7\mathrm{Be}} &= 0.97^{+0.04}_{-0.05}\,[\pm 0.12]\,,\\
f_{\mathrm{pep}} &= 1.05 \pm 0.08\,[^{+0.23}_{-0.20}]\,,\\
f_{^{13}\mathrm{N}} &= 1.7^{+2.8}_{-1.0}\,[^{+8.4}_{-1.6}]\,,\\
f_{^{15}\mathrm{O}} &= 0.6^{+0.7}_{-0.4}\,[\leq 2.6]\,,\\
f_{^{17}\mathrm{F}} &\leq 15\,[47]\,.
\end{aligned} \tag{2.56}$$

The determination of the ^{8}B and hep fluxes (as well as the oscillation parameters) is basically unaffected by the luminosity constraint.

Interestingly, the idea that the Sun shines because of nuclear fusion reactions can be tested accurately by comparing the observed photon luminosity of the Sun with the luminosity inferred from measurements of solar neutrino fluxes. We find that the energy production in the *pp*-chain and the CNO-cycle without imposing the luminosity constraint are given by:

$$\frac{L_{\text{pp-chain}}}{L_\odot} = 1.03^{+0.08}_{-0.07}\,[^{+0.21}_{-0.18}] \qquad \text{and} \qquad \frac{L_{\text{CNO}}}{L_\odot} = 0.008^{+0.005}_{-0.004}\,[^{+0.014}_{-0.007}]\,. \tag{2.57}$$

Comparing Eqs. (2.55) and (2.57) we see that the luminosity constraint has

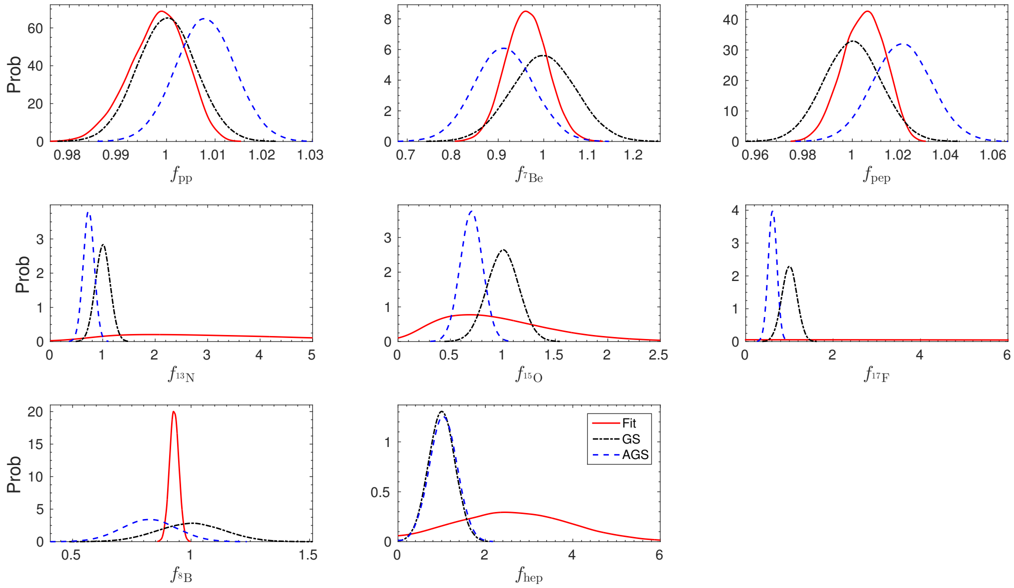

Figure 2.4: Marginalized one-dimensional probability distributions for the best determined solar fluxes in our analysis as compared to the predictions for the two SSMs in Ref. [2].

only a limited impact on the amount of energy produced in the CNO-cycle. However, as discussed above, the amount of energy in the *pp*-chain can now significantly exceed the total quantity allowed by the luminosity constraint. Altogether we find that the present value for the ratio of the neutrino-inferred solar luminosity, $L_\odot$(neutrino-inferred), to the photon luminosity $L_\odot$ is:

$$\frac{L_\odot(\text{neutrino-inferred})}{L_\odot} = 1.04\left[{}^{+0.07}_{-0.08}\right]\left[{}^{+0.20}_{-0.18}\right]. \tag{2.58}$$

Thus we find that, at present, the neutrino-inferred luminosity perfectly agrees with the measured one, and this agreement is known with a 1σ uncertainty of 7%, which is a factor two smaller than the previous best determination [81].

2.3.3 Comparison with Solar Models

Next we compare the results of our determination of the solar fluxes with the expectations from the solar models, SSM=GS (for SFII-GS98) and SSM=AGS (for SFII-AGSS09). To construct the prior distribution of the fluxes in the models we use the predictions $\langle f_i^{\rm SSM}\rangle$ for the fluxes, the relative uncertainties $\sigma_i^{\rm SSM}$ and their correlations $\rho_{ij}^{\rm SSM}$ in both models as obtained from Refs. [2]. The prior distribution $\pi(\boldsymbol{f}|\text{SSM})$ with maximum entropy (*i.e.*, minimum information) satisfying these constraints is a multivariate normal distribution. In Fig. 2.4 we show the marginalized one-dimensional probability distributions for the solar neutrino fluxes as determined by our analysis including the luminosity constraint, together with the corresponding prior distributions for the two SSMs.

Comparison between the two models can be achieved by calculating the posterior odds, given data $\boldsymbol{D}$, simply using Bayes' theorem. As described in Sec. 2.2.1 for models with equal prior distributions this is quantified in terms of the Bayes factor in Eq. (2.39) giving the ratio of the evidences. Here we compute the evidences $\mathcal{Z}_{\text{SSM}}$ as in Eq. (2.36) with the prior distributions for the f_i in each model described above and the likelihood function as in Eq. (2.43) where now $\mathcal{O}_i(\boldsymbol{\omega})$ are the model predicted values for all these observables obtained for a given set of values of the fluxes.

Our calculation shows that $\ln(\mathcal{B}) = \ln \mathcal{Z}_{\text{GS}}/\mathcal{Z}_{\text{AGS}} = 0.00 \pm 0.05$, meaning that the data has *absolutely* no preference for either model (as we will see in the next chapter this slightly changes with the new generation of B16 SSM's of Ref. [1]). Quantitatively this result is driven by the most precisely measured ^{8}B flux, which, as seen in Fig. 2.4, lies right in the middle of the predictions of SFII-GS98 and SFII-AGSS09. In what respects the possible discriminating power from the other precisely measured fluxes, in particular ^{7}Be and indirectly pp and pep, one must realize that within the SSMs the fluxes originating from the *pp*-chain are rather correlated among them; therefore, after the determination of the ^{8}B flux is imposed the posterior predictions of all the other *pp*-chain fluxes are also *pushed* towards the average of the two models, essentially making them indistinguishable with respect to measurements of these fluxes. In order to estimate how the correlations predicted by the SSM affect the comparison of the solar models, we define two new schemes GS′ and AGS′ where such correlations have been removed, *i.e.*, $\rho_{ij}^{\text{SSM}} = \delta_{ij}$. In this case we find $\ln(\mathcal{B}) = \ln \mathcal{Z}_{\text{GS}'}/\mathcal{Z}_{\text{AGS}'} = 0.2 \pm 0.1$, meaning that even without the effect of the *pp*-chain correlations present data are unable to break the degeneracy between models implied by the ^{8}B measurement.

On the other hand, the CNO fluxes are rather uncorrelated with the *pp*-chain fluxes, so even with the "democratic" ^{8}B flux result discussed above one could aim at discriminating between the solar models by measuring the CNO fluxes (also taking into account that their expectations strongly differ between the two models, as seen Fig. 2.4). To quantify this possibility we repeat our analysis including also an hypothetical future measurement of the total CNO flux, $\Phi_{\text{CNO}} = f_{^{13}\text{N}}\Phi^{\text{ref}}_{^{13}\text{N}} + f_{^{15}\text{O}}\Phi^{\text{ref}}_{^{15}\text{O}} + f_{^{17}\text{F}}\Phi^{\text{ref}}_{^{17}\text{F}}$, characterized by a given uncertainty σ_{CNO} and centered at the prior expectation of one of the models (for example the SFII-GS98 model, $\hat{\Phi}_{\text{CNO}} = 5.24 \times 10^8\,\text{cm}^{-2}\,\text{s}^{-1}$). We plot in Fig. 2.5 the result of this exercise where we show the log of the Bayes factor as a function of the assumed relative error on Φ_{CNO}. From this figure we read that within the present model uncertainties a moderate evidence in favor of the model whose CNO fluxes have been assumed (SFII-GS98 in this case) can be achieved by a measurement of such fluxes with $\sigma_{\text{CNO}} = 5\%$ accuracy.

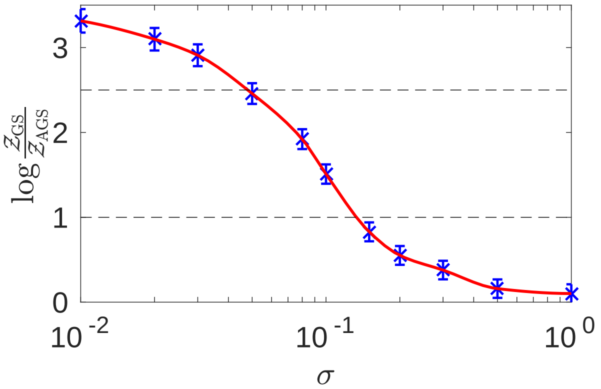

Figure 2.5: Bayes factor as a function of the assumed relative error on Φ_{CNO}. The bars give the numerical uncertainty of our calculations and the curve is a cubic interpolation. The dashed lines marks the limits for weak and moderate evidence of the Jeffreys scale, respectively.

2.4 Summary

The pioneering proposal of using neutrinos to verify the source of energy produced in the Sun has led to great experimental efforts in detecting solar neutrinos in their full energy spectrum. They also helped to establish the now-standard framework of three massive, flavour-mixed neutrinos because the apparent deficit in the rate of solar neutrinos detected compared to the expectations of solar models can be explained by neutrino flavour oscillations in the Sun with MSW matter effects. In this chapter we have used the latest data from both solar and non-solar neutrino experiments to perform an updated analysis which allows for the direct determination of the solar neutrino fluxes independent of solar model. In particular using a Bayesian statistical approach we have derived the neutrino oscillation parameters and solar fluxes which better describe the data. We have done so with and without imposing nuclear physics as the only source of energy generation (the so-called luminosity constraint).

We find that the 99% uncertainty in the ^{7}Be and *pp* (and correspondingly *pep*) fluxes is about a factor 2 smaller, and about 30% smaller in the ^{8}B flux compared with the previous analysis. The uncertainty on the total luminosity due to nuclear physics derived from neutrino data has been reduced by a factor two and is now, for the first time, below 10%. Furthermore, when comparing with SSM's, we have shown that present bounds on CNO neutrino fluxes are very close to the theoretical 3σ range, whether or not other sources of energy contribute to the energy generation. At present there are two sets of SSM's differing in the input solar composition data used in the construction of the model. Both variants lead to different predictions for the solar fluxes, in particular of those produced in the CNO cycle. Comparing those predictions with our extracted fluxes we confirm that with the present neutrino results both models yield comparable significance. We have finished by showing that a future CNO flux measurement with $\sigma_{\rm CNO} = 5\%$ uncertainty would be needed to yield a moderate evidence in favor of one of the two sets.

Chapter 3

Effects on Solar Modeling

Standard Solar Models (SSMs) are a snapshot in the evolution of a $1\,\mathrm{M}_\odot$ star, calibrated to match present-day properties of the Sun. As a prototype of main-sequence stars, the study of solar properties and solar modeling allows us to investigate the stars that are too far to observe. The SSMs built in 1990s demonstrated their great success in the agreement between SSMs and helioseismic observations, providing strong support to stellar evolution theory, as well as in the the solution of the solar neutrino problem within the theory of neutrino oscillation.

The solar surface composition, determined with spectroscopic techniques, is a fundamental constraint in the construction of SSMs. The development of three dimensional hydrodynamic models of the solar atmosphere, of techniques to study line formation under non-local thermodynamic conditions and the improvement in atomic properties (e.g. transition strengths) led since 2001 to a downward revision of solar metal abundances [11, 51, 82]. The SSMs based on the low-Z abundances, however, fail to reproduce all helioseismic probes of solar properties. This is the so called *solar abundance problem* [13, 50, 83]. Different proposed modifications to physical processes in SSMs offer, at best, only partial improvements in some helioseismic probes (e.g. [2, 84–87]). An alternative possibility is to consider modifications to the physical inputs of SSMs at the level of the constitutive physics, radiative opacities in particular.

In this chapter we present our contributions to this issue published in Refs. [1, 88]. We provide assessment of a new generation of SSMs and introduce a new nonparametric modeling of the solar opacity. It is important to stress that the original contribution of this thesis to the SSM's is limited to their statistical comparison with the data, the improvement in the modeling of the opacities as well as the development of the methodology to construct SSM's which match the heloseismological and neutrino observations. But for all the calculations presented in this chapter we were using results from the runs of the SSM codes of A. Serenelli which are an evolution of those developed by J. Bahcall and we are far from mastering all the details they contain.

3.1 New Generation of Standard Solar Models

In this section we describe the new generation of SSMs—B16 SSMs built in Ref. [1] incorporating the latest nuclear rates and standard model refinements. We will do this in Sec. 3.1.2. But for the sake of completeness, we first review in Sec. 3.1.1 the basic assumptions and equations generically used in building SSMs. Finally we provide a statistical comparison of B16 SSMs with solar data to address the status of the solar abundance problem in Sec. 3.1.3.

3.1.1 Introduction to Standard Solar Models

SSMs are built upon a series of basic assumptions: hydrostatic equilibrium, equation of state, thermonuclear reactions, energy conservation, energy transport and initial conditions. We shall discuss them below. The discussion is based on [8, 89, 90].

- *Hydrostatic equilibrium.* It is assumed that the Sun is spherically symmetric and the gravitational force and pressure are locally balanced everywhere. The condition of mass continuity implies that

  $$\frac{dm(r)}{dr} = 4\pi r^2 \rho \,, \tag{3.1}$$

  where $m(r)$ is the mass inside radius r. Consider a thin shell at radius r with thickness dr, the gravitational force on the shell is

  $$g(r) = -\frac{Gm(r)dm(r)}{r^2} \,, \tag{3.2}$$

  while the force induced by the pressure is

  $$f(r) = 4\pi r^2[-P(r+dr) + P(r)] \,. \tag{3.3}$$

  By equaling $g(r)$ and $f(r)$ and plugging in Eq. (3.1) we arrive at the hydrostatic equation

  $$\frac{dP(r)}{dr} = -\frac{Gm(r)\rho(r)}{r^2} \,. \tag{3.4}$$

dP/dr is always negative, implying that the pressure always decreases from the core to the surface of the Sun.

- *Equation of state.* The pressure in the Sun comes from the radiation of photons, and the thermal motion of electrons and ions called gas pressure. The radiation pressure can be obtained simply by the integral of the phase space distribution of photons, which yields

$$P_r = \frac{1}{3} C T^4 \,, \tag{3.5}$$

where C is the radiation density constant. When the temperature is high and the density is low enough, the electrons and ions can be treated as ideal gas. Their pressure can be approximated by

$$P_g = \frac{\rho(r) kT}{\mu(r)} \,, \tag{3.6}$$

where $\mu(r)$ is the mean molecular weight expressed as

$$\frac{1}{\mu(r)} = \frac{n(r)}{\rho(r)} = \frac{\sum\limits_i n_i (1 + Z_i)}{\sum\limits_i m_i n_i} \,, \tag{3.7}$$

where Z_i is the number of free electrons in atom i (1 denotes the number of nuclei) and m_i is the mass of the atom. Defining $X_i \equiv m_i n_i / \sum_j m_j n_j$ as the mass fraction of atom i, we have the relation

$$\frac{1}{\mu} = \sum_i \frac{1 + Z_i}{A_i m_{\rm H}} X_i \,, \tag{3.8}$$

where A_i is the atomic number and $m_{\rm H}$ is the mass of hydrogen atom. In astrophysics, X, Y, Z are often used to represent mass fraction of helium, hydrogen and metals respectively. It is straightforward to see from Eqs. (3.7) and (3.8) that for a completely ionized gas

$$\frac{m_{\rm H}}{\mu} \simeq 2X + \frac{3}{4} Y + \frac{1}{2} Z \,. \tag{3.9}$$

In the outer part of the Sun where temperature is relatively low, atoms may not be completely ionized. As a result, $\mu(r)$ increases from the core to the surface of the Sun. In the previous discussion we have treated electrons and ions as ideal gas. However, in the solar core the density is high enough to bring electrons to partially degenerate states. This requires special treatment of the equation of state.

- *Energy conservation.* It is assumed the Sun's luminosity mainly comes from the nuclear interactions in the solar core. Again consider a spherical shell of thickness dr at radius r, the contribution to local luminosity from the shell is

  $$dL(r) = 4\pi r^2 \rho(r) \epsilon dr \,, \tag{3.10}$$

  where $\epsilon = \epsilon_n + \epsilon_g - \epsilon_\nu$ summarizes the energy contribution from nuclear reactions and gravitational potential and energy loss from neutrinos. We shall only discuss the nuclear reactions which are dominant in the Sun.

- *Thermonuclear reactions.* The solar chemical compositions evolve with the nuclear reactions in the Sun. Consider a typical two-body interaction

  $$a + b \rightarrow c + d \,, \tag{3.11}$$

  and define $R \equiv \langle \sigma v \rangle$ (v is the relative velocity between nuclei a and b), the number of interactions per unit time and unit volume is $r = n_a n_b R$. The evolution of the number density of a is thus given by

  $$\dot{n}_a = -n_a \sum_{b,c} n_b R_{bc} + \sum_{c,d} \frac{n_c n_d}{f_{cd}} R_{cd} \,, \tag{3.12}$$

  where $f_{cd} = 2$ if c and d are identical nuclei and $f_{cd} = 1$ otherwise. Eq. (3.12) can also be written in terms of $X_{a,b,c,d}$ when we transform number density to mass fraction. If energy Q is generated from this reaction, by definition the energy coefficient $\epsilon_n = rQ/\rho$. The typical thermal energy of nuclei in the Sun is several keV. Nevertheless, the nuclei have to overcome the Coulomb barrier of MeV for the reactions to happen. It seems impossible, but Gamow [91] showed that quantum tunneling effects are able to penetrate through the barrier with much lower energy. The tunneling probability is

  $$\text{Prob} = p_0 E^{-1/2} e^{-2\pi\eta} \,, \tag{3.13}$$

  where $\eta = Z_a Z_b e^2/(\hbar v)$ and p_0 is a constant depending on the relative angular momentum of reduced mass of the two nuclei. In astrophysics one often introduces the astrophysical factor (S-factor) defined as

  $$S(E) \equiv \sigma(E) E e^{+2\pi\eta} \tag{3.14}$$

which contains the information of nuclear structure. Following Maxwell distribution we can write R as

$$\begin{aligned} R &= \frac{2^{3/2}}{(\mu\pi)^{1/2}(kT)^{3/2}} \int_0^\infty \sigma(E) E e^{-E/kT} dE \\ &= \frac{2^{3/2}}{(\mu\pi)^{1/2}(kT)^{3/2}} \int_0^\infty S(E) E e^{-E/kT-2\pi\eta} dE\,. \qquad (3.15) \end{aligned}$$

where $E = \mu v^2/2$ has been used with μ as the reduced mass of the colliding nuclei. There are two competing effects in determining the reaction rate. One is the small tail of Maxwell distribution and the other is the increasing tunneling probability at large E. The maximum rate is reached when the exponential in Eq. (3.15) reaches its maximum at $E = (Z_a Z_b \sqrt{m/8\hbar^2} e^2 kT)^{2/3}$. This maximum is known as the Gamow peak. The S-factor $S(E)$ is usually expressed as a Taylor series around $E = 0$ [92], i.e.

$$S(E) = S(0) + S'(0) \cdot E + \frac{1}{2} S''(0) \cdot E^2 + \mathcal{O}(E^3)\,, \qquad (3.16)$$

and is determined by laboratory measurements for many thermonuclear reactions.

- *Energy transport.* There are three different ways of energy transport in stars: radiation, convection and conduction. Conduction plays a role in the high density stars and supernova cores, but is considered to be less relevant in the Sun. In the central part of the Sun radiation is the most efficient transport process while in the outer part convection becomes important.

  The radiative transport is caused by the interaction of photons with electrons, atoms, ions and molecules. Consider a photon flux F_r penetrating a slab of unit area and thickness dr at the radius r, the momentum transfer from the photons to the slab is

  $$dp = \frac{dF_r}{c} = \frac{F_r dr}{\lambda c}\,, \qquad (3.17)$$

  where λ is the mean free path of photons. The momentum transfer is just the loss of radiation pressure P_r in the slab. We can define the opacity coefficient $\kappa \equiv 1/(\rho\lambda)$ which describes the probability of photons experiencing one interaction per unit length. In terms of this definition we can write

$$\frac{dP_r}{dr} = -\frac{\kappa \rho F_r}{c} \,. \tag{3.18}$$

The radiative opacity κ depends on temperature, density and chemical compositions explicitly. We will discuss the solar opacity profile and how we have improved the modeling of the opacity profile in Sec. 3.2. Given the local luminosity $L(r) = 4\pi r^2 F_r$ and Eq. (3.5) we have

$$\frac{dT}{dr} = -\frac{3\kappa\rho}{4acT^3}\frac{L}{4\pi r^2} \,. \tag{3.19}$$

This is the equation responsible for radiation energy transport.

When the radiative opacity increases too much, the radiative temperature gradient increases so much that the solar matter becomes convectively unstable. In the Sun there is a large convective region below the photosphere. The treatment of convective transport is extremely complicated because the gas flow in the convective region is turbulent and varies in a chaotic way. A detailed descripion of convection is beyond the scope of this thesis, but we refer readers who are interested to [90].

- *Initial conditions.* It is assumed that the Sun was initially chemically homogeneous and that mass loss is negligible at all times during its evolution up to the present solar age, $\tau_\odot = 4.57\,\mathrm{Gyr}$. As part of the initial conditions we also need the initial solar composition. It can be inferred from the observations of present solar photosphere and from meteorites. By analysis of the light spectrum from the Sun we can infer the chemical composition in the photosphere. However, the photospheric values may not represent the initial composition in the protosolar nebula. On the one hand, light elements are burned in the low temperature photosphere. On the other hand, gravitational diffusion causes heavier metals to sink relative to hydrogen, and the temperature gradient also causes lighter elements to rise relative to heavier ones which is called thermal diffusion [47]. As for the abundances which are inferred from meteorites the problem is that volatile elements (H, He, C, N, O) have been depleted in the meteorites and only refractory elements remain so one does not have the complete set of relative abundances using meteorite data only. But using the measured abundance of some of the refractory elements (Mg, Al, Si) both in the photosphere and in the meteorite one can then normalize the meteorite data. Up to now there has been very good agreement between the photospheric and meteoritic determination of element abundances, especially for refractory elements [89].

- Adjustable quantities and constraints. The SSM is required to match, at $\tau_\odot$, the solar luminosity $L_\odot$, the solar radius $R_\odot$, and the photospheric (surface) metal-to-hydrogen mass fraction $(Z/X)_\odot$. The three adjustable quantities in the model are the initial helium and metal mass fractions $Y_{\rm ini}$ and $Z_{\rm ini}$ respectively, and the parameter $\alpha_{\rm MLT}$ of the mixing length theory (or its equivalent in other prescriptions of convection). $\alpha_{\rm MLT}$ is mostly related to $R_\odot$, $Y_{\rm ini}$ to $L_\odot$ and $Z_{\rm ini}$ to $(Z/X)_\odot$, although the three adjustable quantities depend on the three observational constraints and are therefore correlated with each other.

In summary, to solve the above equations and build SSMs, one needs the following input quantities: the solar age, diffusion, luminosity, important nuclear rates, and element abundances. We shall list them in the next section when we introduce a new generation of SSMs.

3.1.2 B16 Standard Solar Models

In [2] a generation of SSMs was built using the nuclear reaction rates recommended in the Solar Fusion II paper ([92]; hereafter A11). For simplicity, we refer to them as the SFII SSMs. Here we present the new generation of SSMs, Barcelona 2016 or B16 for short. B16 models share with the SFII models much of the physics. However, important changes include updates in some nuclear reaction rates and, most notably, a new treatment of uncertainties due to radiative opacities. Below we describe in some detail the differences between the older SFII and the new B16 generations of SSMs. This section is based on our work [1].

Composition: The two central sets of solar abundances we use in this work are the same employed in [2]:

- GS98: Photospheric (volatiles) + meteoritic (refractories) abundances from [10]. The metal-to-hydrogen ratio used for the calibration is $(Z/X)_\odot = 0.0229$,

- AGSS09met: Photospheric (volatiles) + meteoritic (refractories) abundances from [11]. The metal-to-hydrogen ratio used for the calibration is $(Z/X)_\odot = 0.0178$.

Individual abundances of the most relevant elements for solar modeling for the different compositions we use are given in Table 3.1.

Equation of state: SFII models used the equation of state (EoS) by OPAL [93] in its 2005 version. This EoS has one slight disadvantage: the mixture of metals includes only C, N, O and Ne and their relative abundances

Element	GS98	AGSS09met
C	8.52 ± 0.06	8.43 ± 0.05
N	7.92 ± 0.06	7.83 ± 0.05
O	8.83 ± 0.06	8.69 ± 0.05
Ne	8.08 ± 0.06	7.93 ± 0.10
Mg	7.58 ± 0.01	7.53 ± 0.01
Si	7.56 ± 0.01	7.51 ± 0.01
S	7.20 ± 0.06	7.15 ± 0.02
Ar	6.40 ± 0.06	6.40 ± 0.13
Fe	7.50 ± 0.01	7.45 ± 0.01
$(Z/X)_\odot$	0.02292	0.01780

Table 3.1: Solar abundances from Ref. [10] and Ref. [11] given as $\log \epsilon_i \equiv \log N_i/N_H + 12$. Only elements that most strongly contribute to uncertainties in SSM modeling are included.

	$S(0)$	Uncert. %	$\Delta S(0)/S(0)$	Ref.
S_{11}	$4.03 \cdot 10^{-25}$		0.5%	[95–97]
S_{17}	$2.13 \cdot 10^{-5}$	4.7	+2.4%	[98]
S_{114}	$1.59 \cdot 10^{-3}$	7.5	-4.2%	[99]

Table 3.2: Astrophysical S-factors (in units of MeV b) and uncertainties updated in Ref. [1].

are hardwired in the tables provided and cannot be modified. FreeEOS, the EoS developed by A. Irwin [94], allows us to overcome this difficulty. Due to its flexibility, and its excellent performance when compared to OPAL EoS, we adopt FreeEOS as our standard EoS for the B16 SSMs. For the first time, EoS tables calculated consistently for each of the compositions used (GS98 and AGSS09met) are used in the solar calibrations.

Nuclear rates: The most relevant changes in the B16 SSMs compared to SFII models arise from updates in the nuclear reaction rates. Updates in the reaction rates are generally introduced as changes in $S(0)$ and, eventually, the first and higher order derivatives. New $S(0)$ values and errors are summarized in Table 3.2 together with the fractional changes in $S(0)$ with respect to A11. Rates not listed in Table 3.2 are taken from A11 and remain unchanged with respect to the SFII SSMs. We also present in Table 3.3 a summary of other main cross sections and input parameters used to construct the SSMs.

Treatment of opacity uncertainties: We postpone the discussion until Sec 3.2. We simply mention here that the results presented in this section correspond to the linear parametrization of the opacity uncertainty.

Qnt.	Central value	σ (%)	Ref.
$^3\mathrm{He}(^3\mathrm{He},2\mathrm{p})^4\mathrm{He}$	5.21 MeV b	5.2	1
$^3\mathrm{He}(^4\mathrm{He},\gamma)^7\mathrm{Be}$	$5.6\cdot10^{-4}$ MeV b	5.2	1
$^7\mathrm{Be}(\mathrm{e}^-,\nu_\mathrm{e})^7\mathrm{Li}$	Eq (40) SFII	2.0	1
$^3\mathrm{He}(\mathrm{p},\mathrm{e}^+\nu_\mathrm{e})^4\mathrm{He}$	$8.6\cdot10^{-20}$ MeV b	30.2	1
$^{16}\mathrm{O}(\mathrm{p},\gamma)^{17}\mathrm{F}$	$1.06\cdot10^{-2}$ MeV b	7.6	1
$\tau_\odot$	$4.57\cdot10^9$ yr	0.44	2
diffusion	1.0	15.0	2
$\mathrm{L}_\odot$	$3.8418\cdot10^{33}$ erg s^{-1}	0.4	2

Table 3.3: Central values for the main input parameters and the corresponding standard deviation. (1) A11, (2) [12].

Next we present the main results of the B16 SSMs for GS98 and AGSS09met compositions and discuss differences with respect to the previous SFII models.

Helioseismology: Two helioseismic quantities widely used in assessing the quality of SSMs are the surface helium abundance Y_S and the location of the bottom of the convective envelope R_CZ. Both are listed in Table 3.4 together with the corresponding values inferred from seismic observations. The model errors associated to these quantities are larger in B16 models than previously computed [12] generations of SSMs because of the different treatment of uncertainties in radiative opacities. Compared to SFII models, we find a small decrease in the predicted Y_S by 0.0003 for both compositions and a decrease in the theoretical R_CZ by 0.0007 $\mathrm{R}_\odot$, also for both compositions. The correlation between these quantities in SSMs is $\rho(Y_\mathrm{S}, R_\mathrm{CZ}) = -0.35$ and -0.41 for B16-GS98 and B16-AGSS09met models respectively, as obtained from the MC calculations.

Fig. 3.1 shows the fractional sound speed difference as a function of solar radius. The solar sound speed differences have been obtained for each of the two SSMs by performing new sound speed inversions, using the appropriate reference solar model, based on the BiSON-13 dataset (a combination of BiSON+MDI data) as described in [100]. The resulting $\delta c/c$ curves are not too different with respect to SFII models.

Neutrino fluxes: The most relevant updates in the B16 SSMs are related to updates in several key nuclear reaction rates that have a direct effect on the predicted solar neutrino fluxes. The detailed results for all the neutrino fluxes are summarized in Table 3.5.

SSM predictions for $\Phi(^8\mathrm{B})$ and $\Phi(^7\mathrm{Be})$ are reduced for both GS98 and AGSS09met compositions by about 2% with respect to previous SFII SSM

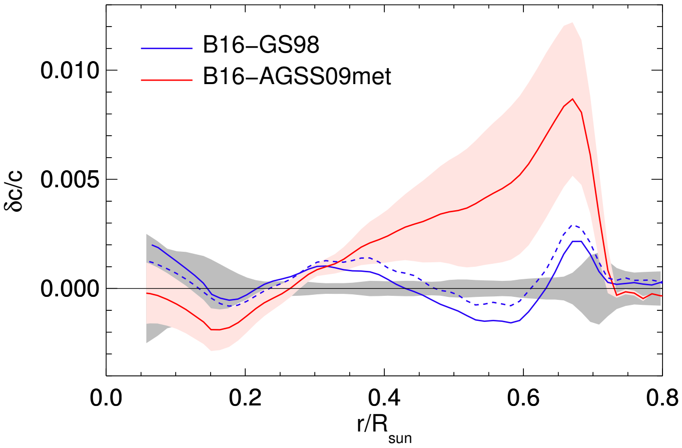

Figure 3.1: Fractional sound speed difference $\delta c/c = (c_\odot - c_{\rm mod})/c_{\rm mod}$. Grey shaded regions corresponds to errors from the inversion procedure. Red shaded region corresponds to errors from the model variation which we chose to plot around the AGSS09met central value (solid red line). An equivalent relative error band holds around the central value of the GS98 central value (solid blue line) which we do not plot for the sake of clarity (it is shown in the left panel in Fig. 3.3, linear opacity band) . Dashed line shows, for comparison, results for the older SFII-GS98 SSM.

Qnt.	B16-GS98	B16-AGSS09met	Solar
$Y_{\rm S}$	0.2426 ± 0.0059	0.2317 ± 0.0059	0.2485 ± 0.0035
$R_{\rm CZ}/{\rm R}_\odot$	0.7116 ± 0.0048	0.7223 ± 0.0053	0.713 ± 0.001
$\langle \delta c/c \rangle$	$0.0005^{+0.0006}_{-0.0002}$	0.0021 ± 0.001	0^a
$\alpha_{\rm MLT}$	2.18 ± 0.05	2.11 ± 0.05	-
$Y_{\rm ini}$	0.2718 ± 0.0056	0.2613 ± 0.0055	-
$Z_{\rm ini}$	0.0187 ± 0.0013	0.0149 ± 0.0009	-
$Z_{\rm S}$	0.0170 ± 0.0012	0.0134 ± 0.0008	-
$Y_{\rm C}$	0.6328 ± 0.0053	0.6217 ± 0.0062	-
$Z_{\rm C}$	0.0200 ± 0.0014	0.0159 ± 0.0010	-

Table 3.4: Main characteristics for the different SSMs with the correspondent model errors and the values for the observational values (when available) and their error. The observational values of $Y_{\rm S}$ is taken from [13] and $R_{\rm CZ}$ from [14]. The solar value of $\delta c/c.$ is zero, by construction.

due to the larger $\rm p(p, e^+\nu_e)d$ rate (for $\Phi(^8\rm B)$ this is partially compensated by the increase in the $^7\rm Be(p,\gamma)^8B$ rate). But the most important changes in the neutrino fluxes occur for $\Phi(^{13}\rm N)$ and $\Phi(^{15}\rm O)$, in the CN-cycle. These fluxes are potentially excellent diagnostics of properties of the solar core. In particular, their dependence on the metallicty is two-fold: through opacities much in the same manner as pp-chain fluxes, and also through the influence of the added C+N abundance in the solar core. This latter dependence makes these fluxes a unique probe of the metal composition of the solar core. The expectation values in the B16 SSMs are about 6% and 8% lower than for the previous SFII models for $\Phi(^{13}\rm N)$ and $\Phi(^{15}\rm O)$ respectively. This results from the combined changes in the p+p and ^{14}N+p reaction rates (Table 3.2).

3.1.3 Statistical Comparison of B16 Models

The general procedure which we will follow is to use MC generated sets of SSMs obtained for different choices of the model input parameters. These are 20 quantities: the Sun luminosity – $L_\odot$– , the Sun diffusion, the Sun age –$\tau_\odot$– , 8 Nuclear Rates – S_{11}, S_{33}, S_{34}, S_{17}, S_{e7}, S_{114}, $S_{\rm hep}$, S_{116} –, and 9 Element Abundances – C, N, O, Ne, Mg, Si, S, Ar, Fe –.

The sets of models are generated according to priors for these inputs which reflect our knowledge of those (knowledge which is independent of the data used in our analysis). Generically the priors are assumed to be Gaussian distributed. The assumed priors for the first 11 inputs are common to all models generated, while for the abundances there are two different sets of priors corresponding to high-Z and low-Z compositions leading to the B16-

Flux	B16-GS98	B16-AGSS09met	Solar^a	Chg.
$\Phi(\mathrm{pp})$	$5.98(1 \pm 0.006)$	$6.03(1 \pm 0.005)$	$5.97^{(1+0.006)}_{(1-0.005)}$	0.0
$\Phi(\mathrm{pep})$	$1.44(1 \pm 0.01)$	$1.46(1 \pm 0.009)$	$1.45^{(1+0.009)}_{(1-0.009)}$	0.0
$\Phi(\mathrm{hep})$	$7.98(1 \pm 0.30)$	$8.25(1 \pm 0.30)$	$19^{(1+0.63)}_{(1-0.47)}$	-0.7
$\Phi(^7\mathrm{Be})$	$4.93(1 \pm 0.06)$	$4.50(1 \pm 0.06)$	$4.80^{(1+0.050)}_{(1-0.046)}$	-1.4
$\Phi(^8\mathrm{B})$	$5.46(1 \pm 0.12)$	$4.50(1 \pm 0.12)$	$5.16^{(1+0.025)}_{(1-0.017)}$	-2.2
$\Phi(^{13}\mathrm{N})$	$2.78(1 \pm 0.15)$	$2.04(1 \pm 0.14)$	≤ 13.7	-6.1
$\Phi(^{15}\mathrm{O})$	$2.05(1 \pm 0.17)$	$1.44(1 \pm 0.16)$	≤ 2.8	-8.1
$\Phi(^{17}\mathrm{F})$	$5.29(1 \pm 0.20)$	$3.26(1 \pm 0.18)$	≤ 85	-4.2

Table 3.5: Model and solar neutrino fluxes. Units are: 10^{10} (pp), 10^9 (^{7}Be), 10^8 (pep, ^{13}N, ^{15}O), 10^6 (^{8}B,^{17}F) and 10^3(hep) cm^{-2}s^{-1}. Solar values from Eq.(2.54). Last column corresponds to the relative changes (in %) with respect to SSMs based on SFII nuclear rates, which are almost independent of the reference composition.

GS98 and B16-AGSS09met model subsets respectively.

Following the procedure outlined in Sec. 2.2.1 we confront these models with the data from helioseismology and neutrino oscillation experiments. They amount to an effective number of 32 data points from helioseismic data plus a large number of points from the global analysis of neutrino oscillation data as described in Sec. 2.2.2 with which we build the likelihood function

$$-2\ln\mathcal{L}(\boldsymbol{\Theta}) = \sum_{i,j} \frac{(\mathcal{O}_i^{\mathrm{mod}}(\boldsymbol{\Theta}) - \mathcal{O}_i^{\mathrm{dat}})}{\sigma_i^{\mathrm{dat}}} (\rho^{\mathrm{dat}})^{-1}_{ij} \frac{(\mathcal{O}_j^{\mathrm{mod}}(\boldsymbol{\Theta}) - \mathcal{O}_j^{\mathrm{dat}})}{\sigma_j^{\mathrm{dat}}} \tag{3.20}$$

where $\mathcal{O}_i^{\mathrm{mod}}(\boldsymbol{\Theta})$ are the model predicted values for all these observables obtained by MC generation for a given set of values of the model inputs $\boldsymbol{\Theta}$. The correlation matrix $\rho_{ij}^{\mathrm{dat}} = \delta_{ij}$ for $i, j = 1, 32$ but it is not diagonal for all the other entries which correspond to the neutrino oscillation data.

With these likelihood functions we can obtain the posterior distribution for some (or all) of the input parameters. These posterior distributions will quantify how the inclusion of this additional data affects our knowledge of those properties of the Sun.

Also, as described in Sec. 2.2.1, we can use the prior predictive distribution corresponding to the two variants of the SSM's to carry out a test of significance and to obtain their corresponding p-values. For this, we define the statistical test $\mathcal{T}(\boldsymbol{\mathcal{O}})$ (where $\boldsymbol{\mathcal{O}}$ is an n-dimensional vector containing possible values for the n observables):

$$\mathcal{T}(\boldsymbol{\mathcal{O}}) = (\boldsymbol{\mathcal{O}} - \langle \boldsymbol{\mathcal{O}}^{\mathrm{mod}} \rangle)^T (C_{\mathrm{dat}} + C_{\mathrm{mod}})^{-1} (\boldsymbol{\mathcal{O}} - \langle \boldsymbol{\mathcal{O}}^{\mathrm{mod}} \rangle) \tag{3.21}$$

where $C_{\mathrm{dat},ij} = \rho_{ij}^{\mathrm{dat}} \sigma_i^{\mathrm{dat}} \sigma_j^{\mathrm{dat}}$ is the covariance matrix associated to the experimental uncertainties, and

$$\begin{aligned} C_{\mathrm{mod},ij} &= \langle (\mathcal{O}_i^{\mathrm{mod}} - \bar{\mathcal{O}}_i^{\mathrm{mod}})(\mathcal{O}_j^{\mathrm{mod}} - \bar{\mathcal{O}}_j^{\mathrm{mod}}) \rangle \\ &\equiv \langle (\mathcal{O}_i^{\mathrm{mod}} - \bar{\mathcal{O}}_i^{\mathrm{mod}}) \rangle \rho_{\mathrm{mod},ij} \langle (\mathcal{O}_i^{\mathrm{mod}} - \bar{\mathcal{O}}_i^{\mathrm{mod}}) \rangle \end{aligned} \tag{3.22}$$

is the model covariance matrix obtained from the MC generated model predictions by sampling over the model input priors about their means $\bar{\mathcal{O}}_i^{\mathrm{mod}} \equiv \langle \mathcal{O}_i^{\mathrm{mod}} \rangle$.

The probability distribution of $\mathcal{T}(\boldsymbol{\mathcal{O}})$ can be determined from the MC model predictions by generating pseudo experimental results $\boldsymbol{\mathcal{O}}$ normally distributed according to C_{dat} around each $\boldsymbol{\mathcal{O}}^{\mathrm{mod}}$ in the MC generated model samples, and computing for each pseudo experimental result the corresponding value of $\mathcal{T}$. We find that, as expected, the probability distribution of $\mathcal{T}(\boldsymbol{\mathcal{O}})$ follows very closely a χ_n^2-distribution.

A comparison of B16 SSMs and data is summarized in Table 3.6 (see also LIN-OP sections of Tables. 3.7 and 3.8).

Considering the surface helium abundance Y_{S} and the location of the bottom of the convective envelope R_{CZ} only, the comparison yields $\mathcal{T}(\boldsymbol{\mathcal{O}}) = 0.91$ and $\mathcal{T}(\boldsymbol{\mathcal{O}}) = 6.45$ for GS98 and AGSS09met compositions that translate into 0.5σ and 2.1σ differences between models and data.

		GS98		AGSS09met	
Case	dof	$\mathcal{T}(\boldsymbol{\mathcal{O}})$	p-value (σ)	$\mathcal{T}(\boldsymbol{\mathcal{O}})$	p-value (σ)
$Y_{\mathrm{S}} + R_{\mathrm{CZ}}$ only	2	0.9	0.5	6.5	2.1
$\delta c/c$ only	30	58.0	3.2	76.1	4.5
$\delta c/c$ no-peak	28	34.7	1.4	50.0	2.7
$\Phi(^7\mathrm{Be}) + \Phi(^8\mathrm{B})$	2	0.2	0.3	1.5	0.6
all ν-fluxes	8	6.0	0.5	7.0	0.6
global	40	65.0	2.7	94.2	4.7
global no-peak	38	40.5	0.9	67.2	3.0

Table 3.6: Comparison of B16 SSMs against different ensembles of solar observables.

A quantitative assessment of the agreement between model and solar sound speeds is not straightforward. It requires a proper evaluation of model errors and correlations. Also, given a set of observed frequencies, extraction of the sound speed profile is sensitive to uncertainties in the measured frequencies, numerical parameters inherent to the inversion procedure and the solar model used as a reference model for performing the inversion. Such detailed analysis was carried out in [101], in which the SSM response to varying input parameters was modeled using power-law expansions and the three uncertainties related to the extraction of $\delta c/c$ from observed data were taken directly from [102].

Using model and inversion uncertainties as described above, we compare how well the predicted sound speed profiles of B16-GS98 and B16-AGSS09met agree with helioseismic inferences. For this, we use the same 30 radial points employed in [101] (shown in Fig. 3.3). We use the models in the MC simulations to obtain the covariance matrix for these 30 points and assume inversion uncertainties at different radii as uncorrelated. The model predicted values are however strongly correlated as shown in the lower left panel in Fig. 3.3 where we plot a graphical display of the correlations between the 30 values of the sound speed as predicted by the models for the linear parametrization of the intrinsic opacity uncertainty assumed in this section. Results are shown in the second row of Table 3.6. For 30 degrees-of-freedom (dof), B16-GS98 gives $\mathcal{T}(\boldsymbol{\mathcal{O}}) = 58$, or a 3.2σ agreement with data. For B16-AGSS09met results are $\mathcal{T}(\boldsymbol{\mathcal{O}}) = 76.1$, or 4.5σ. Below we analyze in some detail the significance of these results.

It seems apparent from Fig. 3.1 that, at almost all radii, the sound speed profile of B16-GS98 fits well within the 1σ uncertainties. This is true even for the peak right below the convective zone at $r/\mathrm{R}_\odot \approx 0.6 - 0.7$. But looks can be deceiving. The difference between B16-GS98 and the Sun is dominated by wiggles of relatively small amplitude. However, changes in input quantities, including radiative opacities, do not lead to variations in SSM sound speeds on small radial scales, so values of the sound speed at different radii in solar models are strongly correlated as shown in lower left panel in Fig. 3.3. Including these correlations by means of a covariance matrix in the calculation of $\mathcal{T}(\boldsymbol{\mathcal{O}})$ explains why the large value $\mathcal{T}(\boldsymbol{\mathcal{O}}) = 58$ is obtained for the B16-GS98 which, apparently, fits well within 1σ contours. This results reflects the fact that, within the framework of SSMs and the treatment of uncertainties used here, particularly of opacities, it is not possible to find a combination of input parameters that would make the wiggles go away. To confirm this, we checked that when the covariance matrix is assumed diagonal, i.e. correlations are neglected, $\mathcal{T}(\boldsymbol{\mathcal{O}}) = 23.6$ for the sound speed profile of B16-GS98, well within a 1σ result as expected by a naive look at Fig. 3.1.

For B16-AGSS09met, the discrepancy with the solar sound speed is dominated by the large and broad peak in $0.35 < r/\mathrm{R}_\odot < 0.72$. In this case, curiously, correlations in the model sound speed improve somehow the agreement with the data (but it is still rather bad). If, as a test, sound speed correlations are neglected for this model, we obtain a larger $\mathcal{T}(\boldsymbol{\mathcal{O}}) = 100.4$, i.e. the opposite behavior than for B16-GS98.

It is important to notice that in the case of B16-GS98, the largest contribution to the sound speed $\mathcal{T}(\boldsymbol{\mathcal{O}})$ comes from the narrow region $0.65 < r/\mathrm{R}_\odot < 0.70$ that comprises 2 out of all the 30 points. If these two points are removed from the analysis $\mathcal{T}(\boldsymbol{\mathcal{O}})$ is reduced from 58 to 34.7, equivalent to a 1.4σ agreement with the solar sound speed (entry identified as $\delta c/c$ no-peak in Table 3.6). For B16-AGSS09met this test leads to a 2.7σ result. This exercise highlights the qualitative difference between SSMs with different compositions; it shows that for GS98 the problem is highly localized whereas for AGSS09met the disagreement between SSMs and solar data occurs at a global scale, i.e. the *solar abundance problem*.

On the other hand, current determination of solar neutrino fluxes are well described by models with any of the two solar compositions. This is not very different from what we had with the SFII model fluxes described in the previous chapter. We find now that $\mathcal{T}(\boldsymbol{\mathcal{O}})$ values are 6.01 (0.5σ) and 7.05 (0.6σ) for B16-GS98 and B16-AGSS09met models respectively for all neutrino fluxes. This comparison is clearly dominated by the best-determined $\Phi(^8\mathrm{B})$ and $\Phi(^7\mathrm{Be})$ fluxes, where we find $\mathcal{T}(\boldsymbol{\mathcal{O}})(\mathrm{GS98}) = 0.2\,(0.3\sigma)$ and $\mathcal{T}(\boldsymbol{\mathcal{O}})(\mathrm{AGSS09met}) = 1.45\,(0.6\sigma)$ for these two fluxes(see Table 3.6).

What is the performance of both B16 SSMs when all the observables discussed before are used for the comparison? The results for global analysis are summarized in the last two rows of Table 3.6 when the two sound speed points in the region $0.65 < r/\mathrm{R}_\odot < 0.70$ are excluded or not. The final $\mathcal{T}(\boldsymbol{\mathcal{O}})$ values are dominated by the sound speed for both models, although Y_S and R_CZ are also relevant for B16-AGSS09met. The global analysis yields a not too good 2.7σ result for B16-GS98. However, this is strongly linked to the behaviour of the sound speed profile right below the convective zone, as explained in Sect. 3.1.2. Excluding two points in the sound speed lead to an overall, comforting, 0.9σ agreement of this model with solar data. In the case of B16-AGSS09met, the overall agreement with the data is quite poor, at 4.7σ, which improves to only 3.0σ if the critical points in the sound speed profile are excluded. This is still a poor agreement with data.

The corresponding Bayes factors for the two models are given in the first column in Table 3.8. From the table we conclude that the B16-AGSS09met models are always somewhat disfavoured with respect to the B16-GS98 model by all data sets but the most statistical significant effect is driven by the sound speed profile data.

3.2 Improving Solar Opacity Modeling

We have seen in the previous section that B16-GS98 model is not in very good agreement with the global analysis combining both helioseismic and solar neutrino neutrino data and the agreement of B16-AGSS09met model is much worse. We conclude that the solar abundance problem still exists in the new generation of SSMs. Motivated by the persistence of the problem we then move to discuss possible improvements on the methodology in solar model construction. For sake of illustration we make an introduction to the solar opacity profile in Sec. 3.2.1. After that we show in Sec. 3.2.2 the treatment of opacity profile in constructing B16 SSMs as well as a new nonparametric modeling of the solar opacity. Finally we discuss how it can affect the statistical comparison between the models and with the helioseismic data in Sec. 3.2.3.

3.2.1 Introduction to Solar Opacity Profile

A fundamentally important physical ingredient in solar models that cannot be quantified by just one parameter is the radiative opacity, which is a complicated function of temperature (T), density (ρ) and chemical composition of the solar plasma expressed here in terms of the helium (Y) and heavy elements mass fractions (Z_i, where i runs over all metals included in opacity calculations). In the B16 calculations, we used as a reference the atomic opacities from OP [103] complemented at low temperatures by molecular opacities from Ref. [104]. The magnitude and functional form of its uncertainty is currently not well constrained in available opacity calculations. As a result, representation of the uncertainty in radiative opacity by a single parameter [105] or by taking the difference between two alternative sets of opacity calculations [12, 101] are strong simplifications, at best. In the construction of the B16 models we followed a general and flexible approach based on opacity kernels originally developed by Ref. [106] and later on by Ref. [107], which we describe next. This section is mainly based on our work Ref. [88].

The reference opacity calculation $\overline{\kappa}(\rho, T, Y, Z_i)$ can be modified by a generic function of T, ρ, Y and Z_i. For simplicity, we assume that opacity variations are parametrized as a function of T alone such that

$$\kappa(\rho,\, T,\, Y,\, Z_{\rm i}) = [1 + \delta\kappa_{\rm I}(T)]\; \overline{\kappa}(\rho,\, T,\, Y,\, Z_{\rm i}) \tag{3.23}$$

where $\delta\kappa_{\rm I}(T)$ is an arbitrary function that we call *intrinsic opacity change*. The Sun responds linearly even to relatively large opacity variations $\delta\kappa_{\rm I}(T)$

[106, 107]. Thus, the fractional variation of a generic SSM prediction

$$\delta Q \equiv Q/\bar{Q} - 1, \tag{3.24}$$

where Q ($\bar{Q}$) corresponds to the modified (reference) value, and can be described as

$$\delta Q = \int \frac{dT}{T} K_Q(T) \delta\kappa_{\rm I}(T) \tag{3.25}$$

by introducing a suitable kernel $K_Q(T)$ that describes the response of Q to changes in the opacity at a given temperature. We determine the kernels $K_Q(T)$ numerically by studying the response of solar models to localized opacity changes as it was done in Ref. [106].

The evaluation of δQ is subject to the choice we make for $\delta\kappa_{\rm I}(T)$. In Ref. [108] and Ref. [105] the opacity error was modeled as a 2.5% constant factor at 1σ level, comparable to the maximum difference between the OP and OPAL [109] opacities in the solar radiative region. Ref. [107] showed that this prescription underestimates the contribution of opacity uncertainty to the sound speed and convective radius error budgets because the opacity kernels for these quantities are not positive definite and integrate to zero for $\delta\kappa(T) =$ const. Later on, Ref. [101] considered the temperature-dependent difference between OP and OPAL opacities as 1σ opacity uncertainty. However, it is by no means clear that this difference is a sensible measure of the actual level of uncertainty in current opacity calculations.

Based on the previous reasons, in the B16 models we followed a different approach inspired by the most recent experimental and theoretical results and some simple assumptions. The contribution of metals to the radiative opacity is larger at the bottom of the convective envelope ($\sim$ 70%) than at the solar core ($\sim$ 30%). Moreover, at the base of the convective envelope, relevant metals like iron are predominantly in an L-shell configuration, for which atomic models are more uncertain than for the K-shell configuration that predominates at solar core conditions. Also, in a recent theoretical analysis of line broadening modeling in opacity calculations, Ref. [110] has found that uncertainties linked to it are larger at the base of the convective envelope than in the core. These arguments suggest that opacity calculations are more accurate at the solar core than in the region around the base of the convective envelope. It is thus natural to consider an uncertainty parametrization that allows opacity to fluctuate by a larger amount in the external radiative region than in the center of the Sun.

3.2.2 Linear Parametrization vs Gaussian Process

In building B16 SSMs described in the previous section we adopted the following parametrization for the intrinsic opacity change (relative to some reference value):

$$\delta\kappa_I(T) = a + b\,\frac{\log_{10}(T_\mathrm{C}/T)}{\Delta_T} \tag{3.26}$$

where $\Delta_T = \log_{10}(T_\mathrm{C}/T_\mathrm{CZ}) = 0.9$, T_C and T_CZ are the temperatures at the solar center and at the bottom of the convective zone respectively. This equation is applied only up to the lower regions of the convective envelope, where convection is adiabatic and changes in the opacity do not modify the solar structure. Opacity changes in the uppermost part of the convective envelope and atmosphere are absorbed in the solar calibration by changes in the mixing length parameter and, in sound speed inversions, by the surface term. In the context of SSMs, they will not produce changes in the solar properties considered in the present work.

Technically, the opacity uncertainty is incorporated in our model generation by extending the parameter space with 2 more independent inputs, a and b, each with a gaussian prior with zero mean and variances σ_a and σ_b, respectively. This corresponds to assuming that the opacity error at the solar center is $\sigma_\mathrm{min} = \sigma_a$, while it is given by $\sigma_\mathrm{out} \simeq \sqrt{\sigma_a^2 + \sigma_b^2}$ at the base of the convective zone. We fix $\sigma_\mathrm{in} = \sigma_a = 2\%$ which is the average difference of the OP and OPAL opacity tables. This is also comparable to differences found with respect to the new OPAS opacity tables [111] for the AGSS09 solar composition, the only one available in OPAS. The more recent OPLIB tables from Los Alamos [112] show much larger differences in the solar core, about 10 to 12% lower than OP and up to 15% lower than OPAS. However, OPLIB opacities lead to solar models that predict too low Y_S and $\Phi(^7\mathrm{Be})$ and $\Phi(^8\mathrm{B})$ fluxes that cannot be reconciled with data. For σ_out we choose 7% (i.e. $\sigma_b = 6.7\%$), motivated by the recent experimental results of [113] that have measured the iron opacity at conditions similar to those at the base of the solar convective envelope and have found a $7\% \pm 4\%$ increase with respect to the theoretical expectations. The resulting prior for the intrinsic opacity profile uncertainty is shown in the upper left panel in Fig. 3.2 for both B16 models. Given the generated values for those two parameters we construct the function $\delta\kappa_I(T)$ as in Eq. (3.26) and with that we compute the corresponding change in the output quantities as in Eq. (3.25).

As we have seen in the previous section it turns out that this ad-hoc linear parametrization of the intrinsic opacity uncertainty is not flexible enough to accommodate the tension between B16-AGSS09met model and data (especially sound speed data). This parametrization was chosen for its simplicity, whereas in fact the shape of the opacity uncertainty function is unknown. Thus, next we turn to a more general modeling of the intrinsic opacity uncertainty based on a Gaussian Process approach.

Our goal is to define the uncertainty of the opacity profile without using parametrized functions and to reconstruct the intrinsic opacity change $\delta\kappa_{\rm I}(T)$ that can lead to a better agreement with the data. In order to do this, following the discussion for linear opacity, we assume that $\delta\kappa_{\rm I}(T)$ is a gaussian variable with mean $\mu_P(T) \equiv 0$ and with a temperature dependent variance $\sigma(T)$ which allows for 2% uncertainty in the solar center and 7% at the base of the convective zone, i.e.:

$$\sigma(T) = 0.02 + (0.07 - 0.02) \cdot \frac{\log_{10}(T_{\rm C}/T)}{\Delta_T} \,. \tag{3.27}$$

As the values of the opacity at two different temperatures T and T' may be not independent, we introduce a prior covariance function $C_P(T, T')$. A possible choice is

$$C_P(T, T') = \sigma(T)\sigma(T')\rho(T, T'), \tag{3.28}$$

with

$$\rho(T, T') = \exp\left[-\frac{1}{2}\left(\frac{\log_{10} T - \log_{10} T'}{\Delta_T\, L}\right)^2\right] . \tag{3.29}$$

Here L determines the characteristic correlation length over which $\delta\kappa_{\rm I}(T)$ can vary significantly and it is the only hyperparameter in our analysis. According to the above definition, $L = 1$ means maximum correlation between the opacity at the edge of the convective zone and at the center. If L is too large the correlation is too strong and the model is over constrained. If, on the other hand, L is too small, we are allowing opacity errors to dominate the output of solar models, and we can barely learn anything from the data. Moreover, there is a physically motivated lower bound for L given by the temperature range over which the opacity can vary substantially. In the solar interior $|\partial \ln\kappa/\partial \ln T| < 2$ [112]. From this, the smallest temperature range over which $\Delta \ln\kappa \approx 1$ is $\Delta \ln T \approx 0.5$, i.e. $L_{\rm min} \approx 0.2$.

To implement the Gaussian Process intrinsic opacity uncertainty in our analysis we start by choosing a set of N points in which we evaluate the function $\delta\kappa_{{\rm I}i} = \delta\kappa_{\rm I}(T_i)$. We take $N = 11$ and choose the points to be uniformly distributed in $\log_{10} T$ between 6.3 and 7.2. The parameter space for model generation is thus extended with 12 more input parameters: the length L and the 11 $\delta\kappa_{{\rm I}i}$ values. For the correlation length we assume a uniform prior in $\log_{10} L$ between $\log_{10} 0.2$ and $\log_{10} 1$. The values $\delta\kappa_{{\rm I}i}$ are generated according

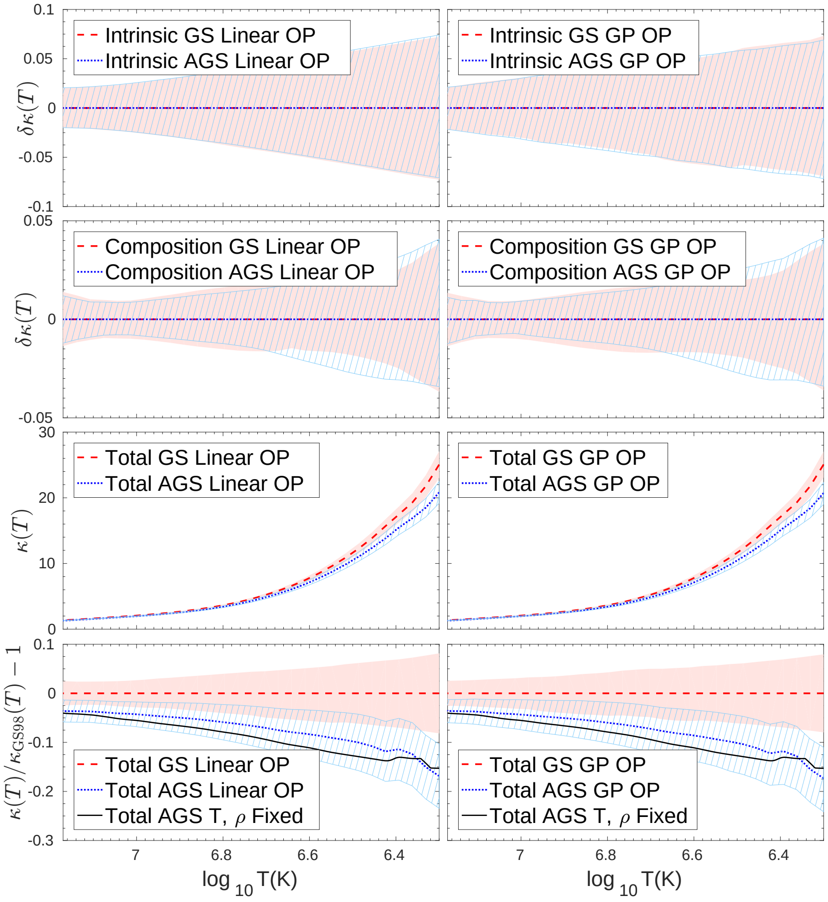

Figure 3.2: Priors for the intrinsic opacity change (upper panels), the composition opacity change, Eq. (3.33) (second row panels), and the total opacity profile in absolute value (third row panels) and relative to the central value for the GS98 model (lower panels). Left correspond to the linear parametrization of the intrinsic opacity uncertainty while right corresponds to the Gaussian Process one. The lower panels also show the curve (same in both panels) with the opacity difference due to the different compositions at fixed physical properties (T and ρ) (the fixed values of T and ρ are those of the GS98 model so the reference GS98 opacity profile is common to all curves in the lower panels).

.

to prior distribution defined by Eqs. (3.27-3.29), together with $\mu_P(T) \equiv 0$[1]. Given a set of values for the 11 $\delta\kappa_{Ii}$'s we construct the full function $\delta\kappa_I(T)$ by linear interpolation between these values and with that we compute the corresponding change in the output predictions as in Eq. (3.25). The resulting prior distribution of the intrinsic opacity change is shown in the upper right panel of Fig. 3.2. As seen in the figure, the ranges of uncertainty profiles for the linear parametrization and the GP opacity are very similar. They do, however, lead to different conclusions when testing the SSM's models versus the data (in particular vs helioseismic data) as described in Sec. 3.2.3.

The properties of the Sun depend on its *opacity profile* $\kappa_{\rm SSM}(T)$ that we define as:

$$\kappa_{\rm SSM}(T) = \kappa(\rho(T),\, T,\, Y(T),\, Z_i(T)) \tag{3.30}$$

where $\rho(T)$, $Y(T)$ and $Z_i(T)$ describe the density, helium and heavy element abundances stratifications as a function of the temperature of the solar plasma in a given SSM. This is indeed the quantity that determines the efficiency of radiative energy transport and, thus, the temperature gradient at each point of the Sun and that is plotted in the panels in the third row of Fig. 3.2 for both B16 models. To better compare the range of prior uncertainty of the opacity profile with the difference between the central values of the priors of the two SSM's, we plot in the lower panels of Fig. 3.2 the same total opacity variation relative to the central value of the B16-GS98 model. The fractional opacity difference due to the change of composition only, i.e. compared at fixed T and ρ, is also shown for reference.

When considering an intrinsic opacity change $\delta\kappa_{\rm I}(T)$ and/or other input parameters in the SSMs are varied, the SSM needs to be recalibrated, thus obtaining different density and chemical abundances stratifications with respect to the reference SSM. As a consequence, the total variation of the solar opacity profile is given by:

$$\begin{aligned}\delta\kappa_{\rm SSM}(T) &\equiv \kappa_{\rm SSM}(T)/\overline{\kappa}_{\rm SSM}(T) - 1 \simeq \\ &\simeq \delta\kappa_{\rm I}(T) + \frac{\partial \ln\kappa}{\partial \ln\rho}\delta\rho(T) + \frac{\partial \ln\kappa}{\partial \ln Y}\delta Y(T) + \\ &\quad + \sum_i \frac{\partial \ln\kappa}{\partial \ln Z_i}\delta Z_i(T)\end{aligned} \tag{3.31}$$

where $\delta\rho(T)$, $\delta Y(T)$ and $\delta Z_i(T)$ are the fractional variations of density and elemental abundances in the perturbed Sun with respect to the reference SSM,

---

[1] We studied the number of points which maximized the smoothness of the output profile versus computing time and found that increasing N beyond 11 did not yield any better results.

evaluated at a fixed temperature T.

As discussed above, the metal abundances $Z_i(T)$ are derived quantities that have to be obtained as a results of numerical solar modeling. However, when we consider a modification of the surface composition $\{z_i\}$, expressed here in terms of the quantities $z_i \equiv Z_{i,\mathrm{S}}/X_\mathrm{S}$ where $Z_{i,\mathrm{S}}$ is the surface abundance of the $i-$element and X_S is that of hydrogen, we can approximately assume $\delta Z_i(T) \simeq \delta z_i$ where δz_i is the fractional variation of z_i with respect to some reference value. As a consequence, Eq. (3.31) can be rewritten as:

$$\delta\kappa_\mathrm{SSM}(T) = \delta\kappa_\mathrm{I}(T) + \delta\kappa_\mathrm{Z}(T) + \frac{\partial \ln\kappa}{\partial \ln\rho}\delta\rho(T) + \frac{\partial \ln\kappa}{\partial \ln Y}\delta Y(T) \qquad (3.32)$$

where the *composition opacity change* $\delta\kappa_\mathrm{Z}(T)$ is defined as:

$$\delta\kappa_\mathrm{Z}(T) \equiv \sum_i \frac{\partial \ln\kappa}{\partial \ln Z_i}\delta z_i \qquad (3.33)$$

We define the total opacity change $\delta\kappa(r)$ as:

$$\delta\kappa(T) = \delta\kappa_\mathrm{I}(T) + \delta\kappa_\mathrm{Z}(T), \qquad (3.34)$$

which groups together the contributions to $\delta\kappa_\mathrm{SSM}(T)$ directly related to the variations of the input parameters.

For completeness, we show in the middle panels of Fig. 3.2 the prior distributions of the composition opacity changes for both B16-SSMs, calculated by considering the relative variations of the individual abundances δz_j around their mean values for GS98 and AGSS09met surface compositions. The logarithmic derivatives $\partial \ln\kappa/\partial \ln Z_i$ can be found in the left panel of Figure 10 in Ref. [101]. The prior distributions for $\delta\kappa_\mathrm{Z}(T)$ are identical in the left and right (middle) panels because the adopted procedure for describing the intrinsic opacity uncertainty does not alter the sampling in surface composition.

3.2.3 Effects on Statistical Tests of Models

We start by performing a test of significance of the two B16 SSMs using the linear and GP models of the opacity uncertainty described in the previous section. Results are given in Table 3.7 where we show the value of the test statistics $\mathcal{T}$ for different combination of observables. The results for the LIN-OP parametrization are the same as already shown in Table 3.6 but we repeat them here for clarity in the comparison with the GP-OP case. As seen in the table and previously discussed, global p-values are dominated by the sound speed for both models, although Y_S and R_CZ are also relevant for

		LIN-OP				GP-OP			
		GS98		AGSS09met		GS98		AGSS09met	
$\boldsymbol{\mathcal{O}}$	n	$\mathcal{T}(\boldsymbol{\mathcal{O}})$	p-value (σ)	$\mathcal{T}(\boldsymbol{\mathcal{O}})$	p-value (σ)	$\mathcal{T}(\boldsymbol{\mathcal{O}})$	p-value (σ)	$\mathcal{T}(\boldsymbol{\mathcal{O}})$	p-value (σ)
$Y_{\rm S} + R_{\rm CZ}$	2	0.9	0.5	6.5	2.1	0.7	0.35	6.9	2.2
δc	30	58.0	3.2	76.1	4.5	35.6	1.2	40.2	1.6
all ν-fluxes	8	6.0	0.5	7.0	0.6	5.9	0.44	7.0	0.6
global	40	65.0	2.7	94.2	4.7	45.1	1.1	57.1	2.1

Table 3.7: Comparison of B16 SSMs against different ensembles of solar observables.

B16-AGSS09met. We also read from the table the previously shown results that that when using the linear opacity uncertainty parametrization the global analysis yields a not too good p-value of 2.7σ for B16-GS98 and considerably worse (4.7σ) for the B16-AGSS09met. However, as seen in the table the results are different when the GP opacity uncertainty is used which yields p-value of 1.1σ and 2.1 σ for B16-GS98 and B16-AGSS09met, respectively.

In Fig. 3.3 we plot the fractional sound speed difference $\delta c(r) \equiv (c_{\rm obs}(r) - c(r))/c(r)$, where $c_{\rm obs}(r)$ is the sound speed inferred from helioseismic data while $c(r)$ represent the sound speed profile predicted by the B16-GS98 (left) and B16-AGSS09met (right) model, respectively. The blue (lighter) hatched area and the red (darker) shaded area corresponds to the 1σ theoretical uncertainties in sound speed predictions obtained for linear and GP opacity uncertainty priors. As seen from the figure, and expected from the comparison of the top panels in Fig. 3.2, they are not very different in the two considered cases. Moreover, we observe from the figure that at almost all radii, independently of the adopted prescription, the sound speed profile of B16-GS98 fits well within the 1σ data uncertainties. This, as previously described in Sec. 3.1.3, may seem surprising that the B16-GS98 model is not providing a good p-value in the case of linear opacity uncertainty parametrization.

The reason for the bad p-value obtained for the B16-GS98 model is that, as discussed in Sec. 3.1.3 changes in input quantities do not lead to variations in SSM sound speeds on very small radial scales, so values of the sound speed at different radii in solar models are strongly correlated, i.e. the model correlation matrix is highly non-diagonal. The new point here is that the characteristic correlation length is very much dependent on the assumption for functional form of the intrinsic opacity uncertainty. This is explicitly illustrated in the lower panels of Fig. 3.3 where we graphically display the values for the entries of the correlation matrix between the predicted sound speeds at the 30 locations (the correlation matrix is the same for both B16 models). As seen in the figure, the characteristic correlation length (i.e. the distance $|r_i - r_j|$ over which correlations between the predicted values of the sound speeds are strong, say $|\rho_{\mathrm{mod},ij}| \gtrsim 0.5$) is much larger for the linear opacity profile parametrization than for the GP profile.

The more flexible implementation of the opacity profile uncertainty provided by the GP procedure permits to obtain a better description of the observational data for both B16-GS98 and B16-AGSS09met models. To illustrate this point, Fig. 3.4 shows the posterior distribution of L, the correlation length hyperparameter (Eq. (3.28)). As seen from the figure, the best possible description of the data is achieved with correlation lengths of average $\langle L \rangle \sim 0.2$, i.e. close to the lowest value permitted by the adopted prior that allows for short scale modifications of the sound speed profiles.

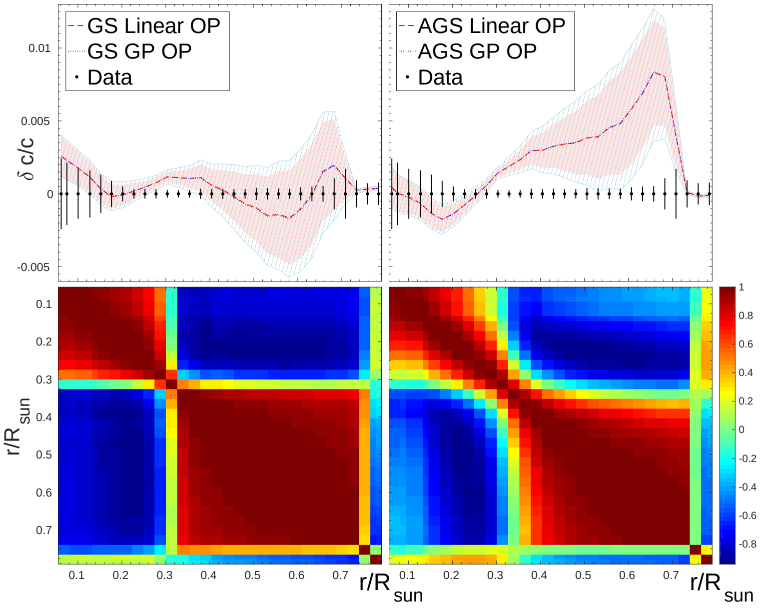

Figure 3.3: One σ range of variation of the fractional sound speed profiles as predicted by the priors of the B16 SSM models for both opacity profile priors discussed in the text (upper panels) compared with the 30 data points used in the analysis. The lower panels graphically display the values of the entries in the 30×30 model correlation matrix between the predicted sound speeds at the 30 points (which are the same for B16-GS98 and B16-AGSS09met models) for the linear opacity uncertainty parametrization (left) and the GP opacity uncertainty(right).

We finish this section by giving in Table 3.8 the Bayes factors for the two models as obtained with their posterior probability distributions after including the neutrino and helioseismic data for the two assumed opacity profile

	B16-AGSS09met/B16-GS98	
Data	LIN-OP	GP-OP
ν	-0.23	-0.27
$+Y_S$+R_{CZ}	-1.6	-2.2
+ sound speeds	-14.7	-4.1

Table 3.8: Bayes factor, ln($\mathcal{B}$), for the B16-AGSS09met vs B16-GS98 model obtained with the different data sets (see table 2.2.1 for interpretation).

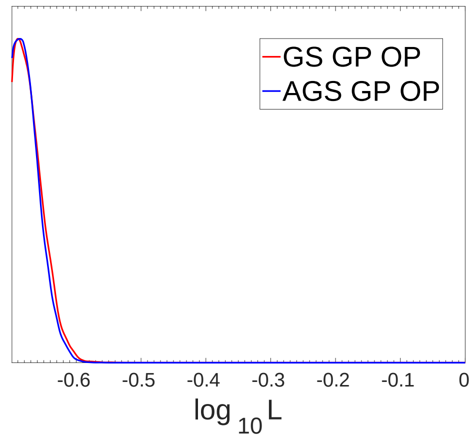

Figure 3.4: Posterior probability distribution for the correlation length hyperparameter L of the GP opacity uncertainty for runs with the models B16-GS98 and B16-AGSS09met priors for the abundances.

uncertainties. As we discussed in Sec. 3.1.3 the B16-AGSS09met models are always somewhat disfavoured with respect to the B16-GS98 model by all data sets but the most statistical significant effect is driven by the sound speed profile data. Here we now can see the dependence of these conclusion on the assumed functional form of the opacity uncertainty. For the linear opacity uncertainty profile the Bayes factor of -14.7 is enough for rejection of the model. Allowing for the most flexible GP form of the opacity uncertainty decreases the evidence against the B16-AGSS09met model to close to strong.

3.3 Neutrino and Helioseismic Data Driven SSM

We now turn to discuss an alternative approach to the abundance problem. Our aim is to use the information from helioseismic and neutrino observations to better determine the solar chemical composition and other solar properties. The technical complication arises from the fact that both neutrino and helioseismic results are *outputs* of the Standard Solar Model simulations while chemical composition and the other properties to be inferred are *inputs*. We are faced then with a common issue in multivariable analysis, the consistent estimation of the values of input parameters (some even with unknown functional dependence) which can provide a valid set of outputs within a given statistical level of agreement with some data. Before the advent of fast computing facilities this could only be attempted by partially reducing the number of inputs to be allowed to vary. For example, in Ref. [101] the problem was analyzed in terms of three continuous multiplicative factors (the abundance of volatiles, that of refractories and that of Ne) to parametrized the allowed departures of the Standard Solar Model inputs from the adopted priors of the two model versions.

In here what we are going to do instead is to make use of Bayesian inference methods described in Sec. 2.2.1 to obtain the posterior probability distribution of the abundance and opacity input parameters which better describe the data. Technically this is done by starting generating a composition unbiased set of models by using a top hat prior for the logarithmic abundances $\varepsilon_i \equiv \log_{10}(N_i/N_{\rm H}) + 12$ that accommodates both the AGSS09met and GS98 admixtures, i.e. with value 1 between the 3σ lower value of the AGSS09met composition and the 3σ upper value of the GS998 composition for all the nine elements relevant for solar model construction given in Table 3.9, and zero outside this range. And we will generate the models for the two parametrizations for the opacity uncertainty. For all other inputs we keep the gaussian priors as in the generation of the B16 models.

In this section we show the results of the inferred composition and other solar inputs in Sec. 3.3.1, the reconstructed solar opacity profile in Sec. 3.3.2 and the output solar neutrino fluxes in Sec. 3.3.3.

3.3.1 Inferred Composition

The results for the inferred composition are shown in Fig. 3.5 where we plot the posterior probability distributions for the nine abundance parameters centered for reference around the GS98 ones, i.e. $\Delta\varepsilon_j = \varepsilon_j - \varepsilon_{j,\rm GS98}$, and for the two choices of priors of the opacity uncertainties (Linear or GP). The window for each abundance corresponds to the allowed range, i.e. where prior=1. Outside each window the value of the prior is zero. For the sake of comparison we also show in the figure the corresponding prior distributions for the B16-GS98 and B16-AGSS09met models. Notice that the distributions are given in arbitrary units and have been normalized in such a way that the maximum of all distributions lays at the same height to help comparison.

We list in the last two columns of Table 3.9 the corresponding ±1-σ ranges

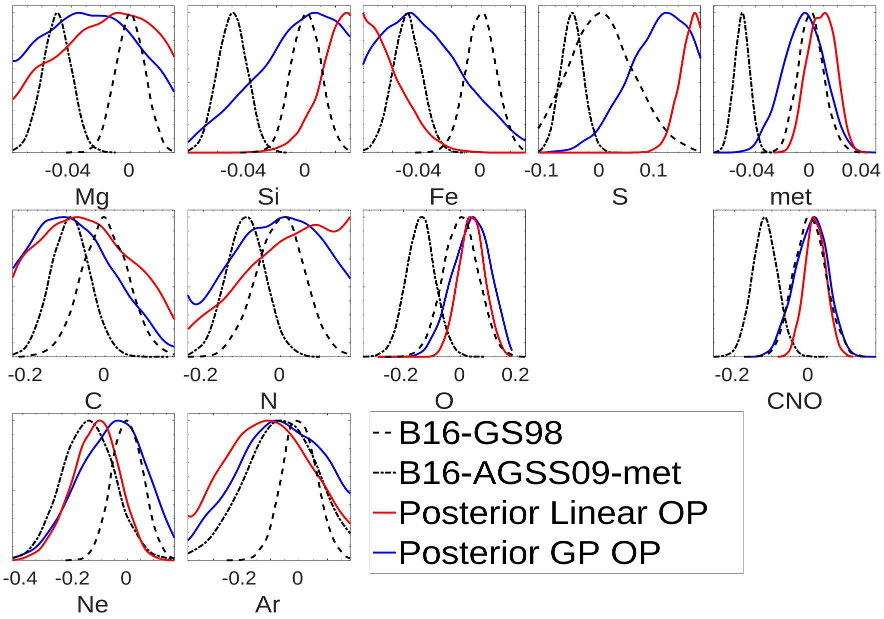

Figure 3.5: Posterior probability distribution for the logarithmic abundances ($\varepsilon_j - \varepsilon_{j,\mathrm{GS98}}$) from the analysis of neutrino and helioseismic data with uniform priors for the abundances and for the two choices of the prior opacity uncertainties. The distributions are given in arbitrary units and they have been normalized in such a way that the maximum of all distributions lays at the same height. See text for details.

for the logarithmic abundances ε_j extracted from these posterior distribution. These can be compared with the determination of the same quantities in GS98 and AGSS09met compilations reported in the first two columns of the same table. From the figure and table we see that the available data is not capable of setting tight constraints on all the elements simultaneously. However we find that the posterior for the combinations of CNO (C+N+O) and meteorite (Mg+Si+S+Fe) abundances [83, 101] have a comparable precision to GS98 and AGSS09met observational determinations for either choice of the opacity uncertainty parametrization. It is important to stress that, as mentioned above, these posterior distributions are not obtained for arbitrary prior values, but allowing only abundance values contained in the range shown in each window. But within this hypothesis the distributions for the abundances have been obtained without assuming any prior correlation between the individual elements. This is in contrast to previous work [83, 101], where abundances of all elements within a group were forced to have the same proportional change. Correlations among the posterior distributions of the abundances appear ex-

Element	GS98	AGSS09met	Linear	GP
C	8.52 ± 0.06	8.43 ± 0.05	[8.32, 8.56]	[8.31, 8.51]
N	7.92 ± 0.06	7.83 ± 0.05	[7.88, 8.10]	[7.81, 8.05]
O	8.83 ± 0.06	8.69 ± 0.05	[8.82, 8.91]	[8.80, 8.94]
Ne	8.08 ± 0.06	7.93 ± 0.10	[7.87, 8.06]	[7.90, 8.16]
Mg	7.58 ± 0.01	7.53 ± 0.01	[7.54, 7.60]	[7.52, 7.58]
Si	7.56 ± 0.01	7.51 ± 0.01	[7.57, 7.59]	[7.54, 7.59]
S	7.20 ± 0.06	7.15 ± 0.02	[7.35, 7.38]	[7.27, 7.37]
Ar	6.40 ± 0.06	6.40 ± 0.13	[6.14, 6.44]	[6.20, 6.50]
Fe	7.50 ± 0.01	7.45 ± 0.01	[7.42, 7.44]	[7.42, 7.48]
CNO	9.04 ± 0.04	8.92 ± 0.03	[9.03, 9.08]	[9.00, 9.09]
meteor.	8.09 ± 0.01	8.04 ± 0.01	[8.08, 8.10]	[8.07, 8.10]

Table 3.9: 1-σ ranges for the logarithmic abundances ε_j. The first two columns show the mean values and uncertainties of the GS98 and AGSS09met heavy element admixtures. The last two columns give the ranges of the posterior distributions from the analysis of neutrino and helioseismic data with uniform abundance priors and for the two choices of the prior opacity uncertainties.

clusively as output of the data analysis. For the sake of illustration we provide in Fig. 3.6 a graphic representation of the correlation among the posterior probability distributions of the different element abundances. As expected, the correlations are smaller for the run with the more flexible GP description of the opacity profile uncertainty. But in general for both GP and linear opacity uncertainties, the correlation among the posterior distributions of the abundances included either the CNO or the meteorite groups are not very large. The exception is provided by the large anticorrelation between the posterior distributions of C and O for the analysis with Linear opacity uncertainty. We have verified that because the allowed ranges of C and O are strongly anticorrelated in this case, the allowed range of CNO group abundance results to be more precise than any of the model priors as seen in the lower central panel in Fig. 3.5.

The posterior distributions for the other solar input parameters – luminosity, diffusion, age, and the eight nuclear rates, are shown in Fig. 3.7 together with their gaussian priors. From the figure we see that with the exception of S_{11} and diffusion coefficients, all others parameters do not get significantly modified with respect to the model priors by the inclusion of the neutrino and helioseismic data, irrespective of the form of the opacity uncertainty. We have verified that the sound speed data are the most relevant in driving the shift in S_{11}. This has to be interpreted as a variation in the effective rate of the

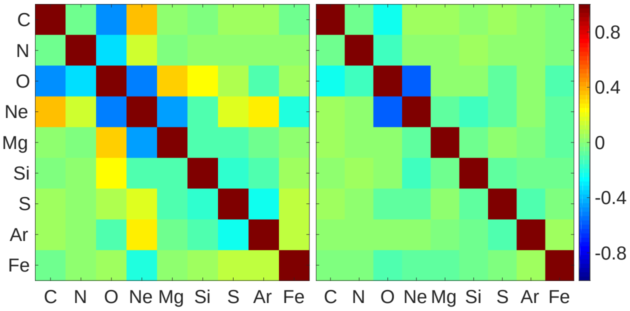

Figure 3.6: Graphical representation of correlations between the posterior distributions of individual elemental abundances for the linear (left) and GP (right) models of intrinsic opacity uncertainty.

proton-proton reaction, but it is not possible to ascribe this change specifically to $S_{11}(0)$ or its derivatives. We see from the figure that the posterior distributions for S_{11} show a preferred value about 1% lower than our prior central value taken from Ref. [95] and 1.5% lower than the newer determination of S_{11} by Ref. [97]. A reassessment of the p-p reaction cross section might be therefore important.

The helioseismic data – the surface helium abundance $Y_{\rm S}$ and the location of the bottom of the convective envelope $R_{\rm CZ}$ – are instead responsible for the preference of lower values of the diffusion coefficients. The reduction in diffusion efficiency that we obtain is in line with previous work [83, 101], and it might be related to the occurrence of macroscopic mixing below the convective envelope [114, 115]. Our analysis points towards a 30±10% reduction, larger in comparison with 12% found in Ref. [101] and closer to 21% found in Ref. [49].

3.3.2 Reconstructed Opacity Profile

We now turn to discuss the optimum profile for the opacity. The corresponding posterior distributions are shown in Fig. 3.8. In the upper left panel, we plot the 1σ range of the intrinsic opacity change $\delta\kappa_I(T)$. This is obtained from the posteriors of the parameters characterizing this function, i.e. the parameters a and b for the linear opacity parametrization given by Eq. (3.26), and the 11 values $\delta\kappa_{Ii} = \delta\kappa_I(T_i)$ that sample the function $\delta\kappa_I(r)$ (after marginalizing over the correlation length L) for GP. By construction, the intrinsic opacity change $\delta\kappa_I(T)$ is defined with respect to a reference opacity calculation $\overline{\kappa}(\rho, T, Y, Z_i)$ that in our analysis include the atomic opacities from OP [103] complemented at low temperatures by molecular opacities from Ref. [104].

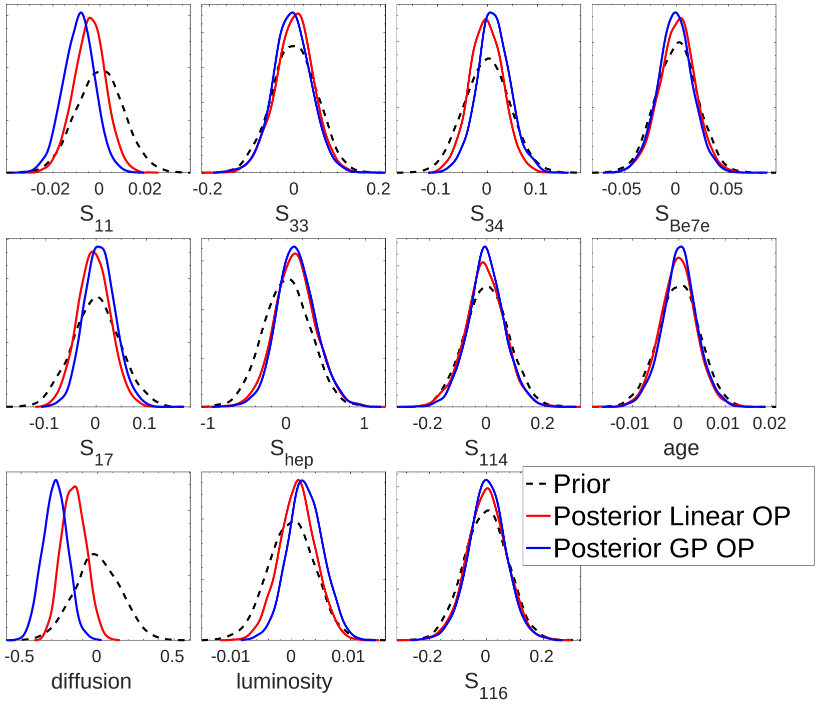

Figure 3.7: Posterior probability distribution for other parameters from the analysis of neutrino and helioseismic data with uniform priors for the abundances and for the two choices of the prior opacity uncertainties. For comparison we also show their prior distribution.

The fact that the posterior distribution of $\delta\kappa_I(T)$ is not centered at zero with a non-trivial T dependence indicates that there are features of the observational data, namely the wiggle in the sound speed profile for $0.3 < r/R_\odot < 0.6$, that cannot be optimally fitted by using the reference opacities, even with the freedom of varying the solar input parameters within their uncertainty ranges and the solar composition in a large intervals considered in here, that accommodate both AGSS09met and GS98 observational results.

As explained in Sec. 3.2.2, the quantity that is directly constrained by observational data is the SSM opacity profile $\kappa_{\rm SSM}(T)$, defined according to Eq. (3.30), that is affected by composition modifications (and solar model recalibration) in addition to the effects of the intrinsic opacity change $\delta\kappa_I(T)$. In the lower panels of Fig. 3.8, we show the posterior distributions for $\kappa_{\rm SSM}(T)$ for the linear (left) and GP (right) description of opacity uncertainty. The posterior distributions for $\kappa_{\rm SSM}(T)$ are compared with the opacity profiles of

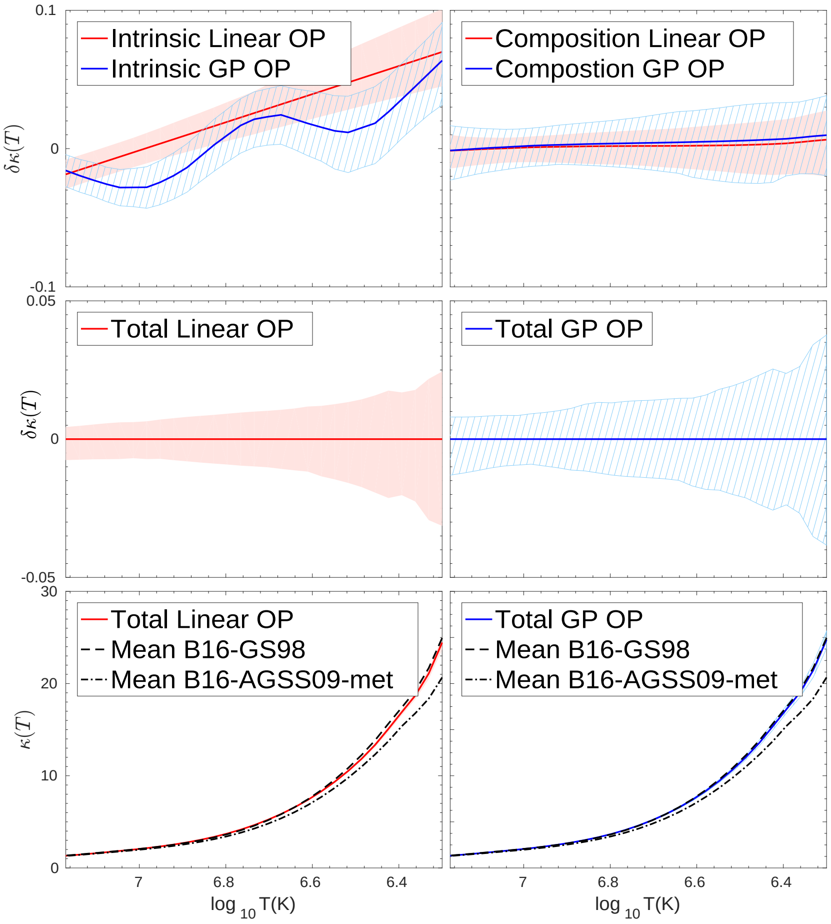

Figure 3.8: Posterior distribution for the opacity profiles for the analysis with uniform priors for the abundances and the two choices of priors of the opacity uncertainties. See text for discussion.

B16-GS98 and B16-AGSS09met models. We see that they are almost coincident with the the opacity profile of B16-GS98 model, as it is expected by considering that the best fit CNO and meteoritic elemental abundances, that drive the change in the opacity, are close to GS98 determinations. The optimal opacity profile is well defined by observational data, as it is seen in the central left (right) panels of Fig. 3.8 where we show the 1σ relative dispersion of $\kappa_{\rm SSM}(r)$ with respect to its mean posterior value. The uncertainty for $\kappa_{\rm SSM}(r)$ is somewhat larger for the GP opacity uncertainty description, ranging from 0.8% at the center to 4% at the base of the convective envelope, while for the linear uncertainty parametrization it varies from 0.5% to 2.5%.

Finally, we note that the uncertainty in $\kappa_{\rm SSM}(r)$ is smaller than that of

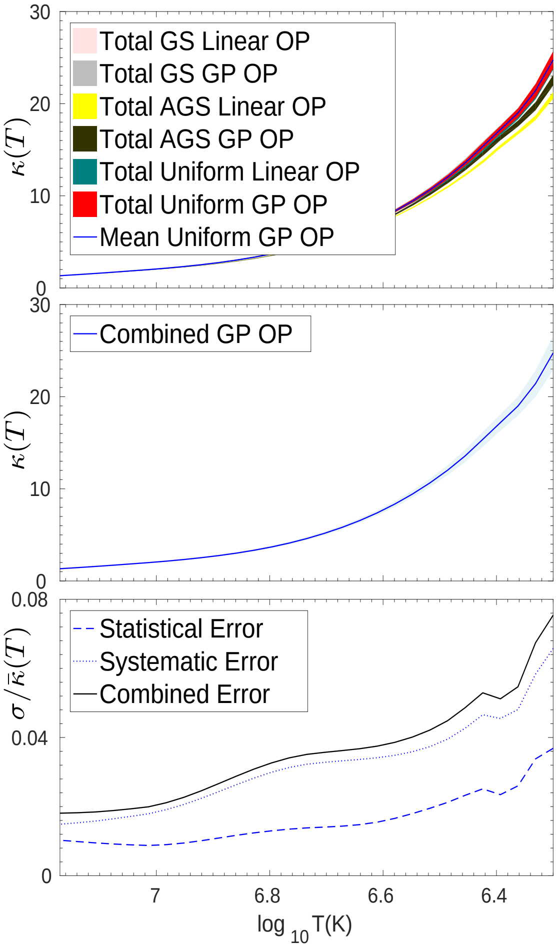

Figure 3.9: **Top**: 1σ ranges for the posteriors of the opacity profiles corresponding to the six choice of priors for the composition and intrinsic uncertainty variation used in this work. **Central**: Posterior distribution for the opacity profiles for the analysis with uniform priors for the abundances and the GP opacity uncertainty. The panel shows the mean and 1σ range of this distribution combining both statistical and systematic uncertainties. **Lower**: The panel shows its "statistical" 1σ uncertainty defined as the corresponding variance of the posterior (shown also as "total" in the central right panel in Fig. 3.8) and its "systematic" uncertainty defined defined as the standard deviation of the six profiles shown on the top window.

the intrinsic opacity change. In fact, $\delta\kappa_I(r)$ is not directly constrained by the observational properties of the Sun and its determination suffers from the degeneracy with the composition opacity change $\delta\kappa_{\rm Z}(T)$ that is quantified by Eq. (3.34). For completeness, we report in the upper (right) panel of Fig. 3.8, the 1σ range for the composition opacity change $\delta\kappa_Z(r)$, obtained from Eq. (3.33) with δz_j being the variance of the posterior distributions of the abundances in Fig. 3.5 defined relative to the mean of those posteriors. Being defined with respect to the mean of the posterior, the corresponding $\delta\kappa_Z$ are centered around zero.

The result obtained with the uniform composition and with GP opacity uncertainty prior represents our best estimate of the radiative opacity profile in the solar interior. On the other hand, the profiles obtained with other choices of priors, such us the uniform composition with linear opacity uncertainty, or the four cases with B16-GS98 and B16-AGSSmet composition priors with either choice of the opacity uncertainty prior presented in Sec. 3.2.3, can serve as a measure of the *systematic* uncertainty in this estimate that reflects dependence on the choice of priors. We show in the top panel in Fig. 3.9 the 1σ range of the posteriors for these six priors. From those we construct a systematic uncertainty in the opacity, at each temperature, defined as the standard deviation of the six reconstructed opacity profiles. The final opacity profile with both error sources added in quadrature is shown in the central panel in Fig. 3.9 and it ranges from 2% at the center to 7.5% at the bottom of the convective zone.

3.3.3 Neutrino Fluxes

Finally, for completeness, we show the resulting posterior distribution for the neutrino fluxes in Fig. 3.10. By construction they constitute the predicted solar neutrino fluxes by models which better describe both the helioseismic and neutrino data. We denote them as helioseismic and neutrino data driven fluxes, B17-HNDD. We list in Table 3.10 their best values and 1σ uncertainties and in Eq. (3.35) their correlations.

$$\rho = \begin{pmatrix} 1.00 & 0.80 & 0.03 & -0.41 & -0.02 & -0.27 & -0.27 & 0.12 \\ 0.80 & 1.00 & 0.06 & -0.33 & -0.05 & -0.28 & -0.29 & 0.01 \\ 0.03 & 0.06 & 1.00 & -0.01 & -0.01 & -0.02 & -0.02 & 0.01 \\ -0.41 & -0.33 & -0.01 & 1.00 & 0.13 & -0.03 & -0.02 & -0.03 \\ -0.02 & -0.05 & -0.01 & 0.13 & 1.00 & 0.04 & 0.06 & 0.06 \\ -0.27 & -0.28 & -0.02 & -0.03 & 0.04 & 1.00 & 0.99 & -0.14 \\ -0.27 & -0.29 & -0.02 & -0.02 & 0.06 & 0.99 & 1.00 & -0.12 \\ 0.12 & 0.01 & 0.01 & -0.03 & 0.06 & -0.14 & -0.12 & 1.00 \end{pmatrix} \tag{3.35}$$

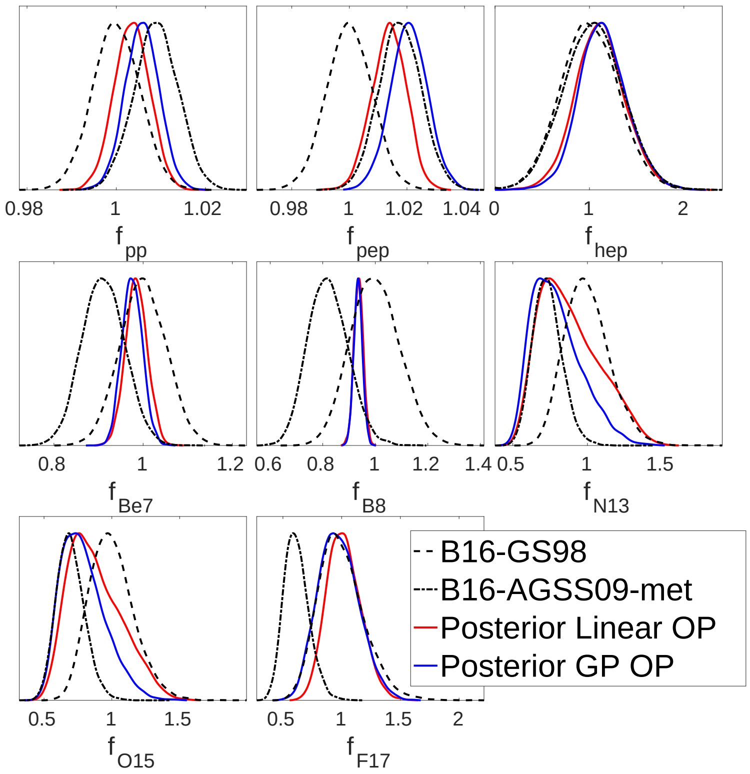

Figure 3.10: Posterior distributions for the neutrino fluxes for the analysis with uniform priors for the abundances and the two choices of priors of the opacity uncertainties. For the sake of comparison we show the corresponding priors for the B16-GS98 and B16-AGSS09met models. The distributions are given in arbitrary units and they have been normalized in such a way that the maximum of all distributions lays at the same height. The fluxes are shown normalized to the B16-GS98 prediction $f_i = \phi_i/\phi_i^{\rm B16-GS98}$.

As expected, we find that for those neutrino fluxes which are at present most precisely determined in solar neutrino experiments, ^{8}B and ^{7}Be, the B17-HNDD flux is very close to their experimental value used to construct the neutrino data part of the likelihood function (see last column in table 3.4) but with a smaller uncertainty because of the additional indirect constraints imposed by the helioseismic data. Interestingly we find that with the inclusion of the helioseismic data the precision of the predicted B17-HNDD CNO fluxes is only at most a factor $\mathcal{O}(2)$ weaker than those of the B16-GS98 or B16-AGSS09met composition models.

B17-HNDD ν-Fluxes

$\Phi(\mathrm{pp})$	$6.017\,(1^{+0.0033}_{-0.0041})$
$\Phi(\mathrm{pep})$	$1.470\,(1 \pm 0.0061)$
$\Phi(\mathrm{hep})$	$9.04\,(1^{+0.22}_{-0.21})$
$\Phi(^{7}\mathrm{Be})$	$4.79\,(1^{+0.027}_{-0.019})$
$\Phi(^{8}\mathrm{B})$	$5.10\,(1 \pm 0.018)$
$\Phi(^{13}\mathrm{N})$	$1.89\,(1^{+0.32}_{-0.14})$
$\Phi(^{15}\mathrm{O})$	$1.50\,(1^{+0.23}_{-0.20})$
$\Phi(^{17}\mathrm{F})$	$4.90\,(1^{+0.22}_{-0.18})$

Table 3.10: Posterior solar neutrino fluxes for uniform-GP models. Units are: 10^{10} (pp), 10^{9} (^{7}Be), 10^{8} (pep, ^{13}N, ^{15}O), 10^{6} (^{8}B, ^{17} F) and 10^{3}(hep) cm^{-2}s^{-1}.

3.4 Summary

In this chapter we have presented our contribution on possible improvements on the solar modeling which can lead to a better description of both neutrino and helioseismic results. As a start we have introduced the latest generation of solar models: B16-GS98 and B16-AGSS09met, the two variants differing in the set of solar abundances (with either lower metallicity or higher metallicity) used as inputs. They include recent updates on some important nuclear reaction rates and a more consistent treatment of the equation of state. They also include a novel and flexible treatment of the opacity uncertainties based on opacity kernels. We present detailed comparisons of the high and low metallicity models against different ensembles of solar observables including solar neutrinos, surface helium abundance, depth of convective envelope and sound speed profile. In particular, a global comparison including all observables yields a p-value of 2.7σ for the B16-GS98 model and 4.7σ for the B16-AGSS09met. The poor agreement mainly lies in the inability for the models to describe the sound speed data.

Motivated by this disagreement we have introduced a new non-parametric modeling of the solar opacity called Gaussian process. This more flexible modeling makes the preference of B16-GS98 model over B16-AGSS09 model less marked. Next we have studied how to “build” models which could better describe the helioseismic and neutrino data. We have done so by using Bayesian inference techniques. Starting from a composition unbiased set of SSMs we have reconstructed the solar opacity profile and other inputs in a data driven way. In this way we have estimated the total opacity uncertainty (data +

priors) to be 7.5% at the base of the convective envelope and 1.8% at the solar core. We have also determined the chemical composition and other solar inputs which better describe the helioseismic and neutrino observations. As an output of the study we have derived the corresponding data driven predictions for the solar neutrino fluxes.

Chapter 4

Astrophysical Neutrinos and Nonstandard Interactions

The detection of ultra-high energy neutrinos of astrophysical origin in IceCube [116–119] marks the onset of high energy neutrino astronomy. From the point of view of astronomy, the main open question resides in finding the sources of such neutrinos, an issue to which many suggestions have been contributed (for a recent review see Ref. [120]). More on the astrophysical front, one also questions what type of mechanisms are at work in those sources to produce such high energy neutrino flux. To address this question the measurement of the flavor composition of the observed neutrinos acquires a special relevance.

Neutrino oscillations modify the flavor composition of the neutrino flux by the time they reach the Earth. In the context of the well established framework of 3ν oscillations these modifications are well understood and quantifiable given the present determination of the neutrino oscillation parameters. Because of this, several studies to quantify the flavor composition of the IceCube events, even with the limited statistics data available, have been presented [121–128] but the results are still inconclusive.

It is well-known that new physics (NP) effects beyond 3ν oscillations in the neutrino propagation can alter the predicted flavor composition of the flux reaching the Earth, thus making the task of elucidating the production mechanism even more challenging. Examples of NP considered in the literature include Lorentz or CPT violation [129], neutrino decay [130, 131], quantum decoherence [132, 133] pseudo-Dirac neutrinos [134, 135], sterile neutrinos [136], non-standard neutrino interactions with dark matter [137], or generic forms of NP in the propagation from the source to the Earth parametrized by effective operators [138]. Besides modifications of the flavor ratios many of these NP effects also induce a modification of the energy spectrum of the arriving neutrinos.

In this chapter we consider an alternative form of NP, namely the possibility of non-standard interactions (NSI) of the neutrinos in the Earth matter. Unlike the kind of NP listed above, NSI in the Earth imply that neutrinos reach the Earth surface in the expected flavor combinations provided by the "standard" 3ν vacuum oscillation mechanism: in other words, NSI in the Earth affect only the flavor evolution of the neutrino ensemble from the entry point in the Earth matter to the detector. The goal of this chapter is to quantify the modification of the neutrino flavor composition at the detector because of this effect within the presently allowed values of the NSI parameters. To this aim we first briefly review in Sec. 4.1 the neutrino flavor composition at the Earth considering only vacuum oscillations. After that, in Sec. 4.2 we illustrate the formalism employed and in Sec. 4.2.1 derive the relevant flavor transition probabilities from the source to the detector including the effect of NSI in the Earth. We show that the resulting probabilities are energy independent while they depend on the zenith angle arrival direction of the neutrinos, in contrast with NP affecting propagation from the source to the Earth. We also present the quantitative results, where in particular we highlight for which source flavor composition the Earth-matter NSI can be most relevant. Next in Sec. 4.2.2 we discuss the incoherent effects arising from the inelastic interaction between neutrinos and the Earth matter in both quantitative and qualitative ways. Finally we give a brief summary in Sec. 4.3. This chapter is based on our work [139].

4.1 Flavor Composition of Astrophysical Neutrinos

Generically cosmic rays are assumed to be the main origin of ultra-high energy neutrinos. They originate from the protons undergoing astrophysical acceleration. Example of the astrophysical accelerators include active galactic nuclei (AGN) [140] and gamma-ray bursts (GRBs) [141]. The high energy protons can interact with ambient gas to produce not only the observed cosmic rays but also neutrinos. The interactions are associated with the production of pions and sometimes neutrons. As a result of their short lifetimes, π^+ and π^- decay into muons and muon neutrinos with muons subsequently decaying into leptons and neutrinos giving rise to the observed high-energy neutrinos. There may also exist other more exotic sources of ultra-high energy neutrinos like superheavy dark matter decay and topological defects (such as cosmic strings, monopoles and hybrid defects) [142]. A detailed discussion of them is beyond the scope of this thesis.

The universe is not fully transparent to high energy comic rays. If their energies exceed the threshold of 5×10^{19} eV, comic rays quickly lose their energies by interactions with the photons of the cosmic microwave background radiation (CMB). This is called the Greisen-Zatsepin-Kuzmin (GZK) limit [143, 144]. Neutrinos on the contrary can reach the Earth basically undeflected and provide us with fundamental information on the source and production mechanism of the cosmc rays.

The flavor composition of the neutrinos produced at the source depends on the production mechanism. For example, for the pion-muon decay chain, which is the most frequently considered, one expects $\phi^s_\mu = 2\phi^s_e$ while $\phi^s_\tau = 0$ [145] (denoting by ϕ^s_α the neutrino flux of flavor ν_α at source). Alternatively, if some of the muons lose energy very rapidly one would predict a single μ-flavor flux while $\phi^s_e = \phi^s_\tau = 0$ [146–150]. If neutrino production is dominated by neutron decay one expects also a single flavor flux but of electron neutrinos [147] so in this case $\phi^s_\mu = \phi^s_\tau = 0$. Decay of charm mesons contributes a flux with equal amounts of electron and muon neutrinos, $\phi^s_e = \phi^s_\mu$ and $\phi^s_\tau = 0$. If several of the above processes in the source compete, arbitrary flavor compositions of ϕ^s_e and ϕ^s_μ are possible but still with $\phi_\tau = 0$ [149]. If, in addition, ν_τ are also produced in the source [151–153], then generically $\phi^s_\alpha \neq 0$ for $\alpha = e, \mu, \tau$.

Next we need to quantify how the flavour composition is modified by oscillations. Our starting point is the initial neutrino (antineutrino) fluxes at the production point in the source which we denote as ϕ^s_α ($\bar{\phi}^s_\alpha$) for $\alpha = e, \nu, \tau$. The corresponding fluxes of a given flavor at the Earth's surface are denoted as $\phi^\oplus_\alpha$ ($\bar{\phi}^\oplus_\alpha$) while the fluxes arriving at the detector after traversing the Earth are ϕ^d_α ($\bar{\phi}^d_\alpha$). They are generically given by

$$\phi^\oplus_\beta(E) = \sum_\alpha \int dE' \mathcal{P}^{s\to\oplus}_{\alpha\beta}(E,E')\phi^s_\alpha(E')\,,\ \phi^d_\beta(E) = \sum_\alpha \int dE' \mathcal{P}^{s\to d}_{\alpha\beta}(E,E')\phi^s_\alpha(E') \tag{4.1}$$

and correspondingly for antineutrinos. $\mathcal{P}$ is the flavor transition probability including both coherent and incoherent effects in the neutrino propagation.

Let us start by considering first only the coherent evolution of the neutrino ensemble. In this case, the flavor transition probabilities from the source (s)

to the Earth entry point ($\oplus$) and to the detector (d) can be written as

$$\mathcal{P}^{s\to\oplus}_{\alpha\beta}(E,E') = P^{s\to\oplus}_{\alpha\beta}(E)\,\delta(E-E')\,, \quad \text{with}\, P^{s\to\oplus}_{\alpha\beta}(E) = \left|A^{s\to\oplus}_{\alpha\beta}(E)\right|^2\,, \tag{4.2}$$

$$\mathcal{P}^{s\to d}_{\alpha\beta}(E,E') = P^{s\to d}_{\alpha\beta}(E)\,\delta(E-E')\,, \quad \text{with}\, P^{s\to d}_{\alpha\beta}(E) = \left|\sum_\gamma A^{s\to\oplus}_{\alpha\gamma} A^{\oplus\to d}_{\gamma\beta}\right|^2\,, \tag{4.3}$$

In the case where astrophysical neutrinos experience vacuum oscillation only, the flavor transition probabilities from a source at distance L are

$$P^{s\to\oplus}_{\alpha\beta}(E) = \sum_{ij} U_{\beta i}U^*_{\beta j}U_{\alpha j}U^*_{\alpha i}\exp(-i\frac{\Delta m^2_{ij}}{2E}L)\,, \tag{4.4}$$

where U is the leptonic mixing matrix. Eq. (4.4) is nothing but a compact form of Eq. (2.15). Since for astrophysical neutrinos the propagation distance L is much longer than the oscillation wavelength, we can average out the vacuum oscillation terms:

$$P^{s\to\oplus}_{\alpha\beta}(E) = \sum_i |U_{\alpha i}|^2|U_{\beta i}|^2\,. \tag{4.5}$$

Flavor composition of the astrophysical neutrinos are usually parametrized in terms of the flavor ratios at the source and at the Earth surface, defined as:

$$\xi^s_\alpha \equiv \frac{\phi^s_\alpha(E)}{\sum_\gamma \phi^s_\gamma(E)}\,, \qquad \xi^\oplus_\beta \equiv \frac{\phi^\oplus_\beta(E)}{\sum_\gamma \phi^\oplus_\gamma(E)} = \sum_\alpha P^{s\to\oplus}_{\alpha\beta}(E)\xi^s_\alpha \tag{4.6}$$

and it has become customary to plot them in ternary plots.

The present determination of the leptonic mixing matrix from the measurements of neutrino oscillation experiments allows us to determine the astrophysical neutrino flavor content at detection given an assumption of the neutrino production mechanism. For completeness and reference we show in Fig. 4.1 the allowed regions of the flavor ratios at the Earth as obtained from the projection of the six oscillation parameter χ^2 function of the global NuFIT analysis of oscillation data [3, 68] in the relevant mixing combinations (see also [122, 138, 154]). We stress that in our plots the correlations among the allowed ranges of the oscillation parameters in the full six-parameter space are properly taken into account. The results are shown after marginalization over the neutrino mass ordering and for different assumptions of the flavor content at the source as labeled in the figure. Fig. 4.1 illustrates the well-known fact [145] that during propagation from the source neutrino oscillations lead to flavor content at the Earth close to $(\xi^\oplus_e : \xi^\oplus_\mu : \xi^\oplus_\tau) = (\frac{1}{3} : \frac{1}{3} : \frac{1}{3})$, with largest

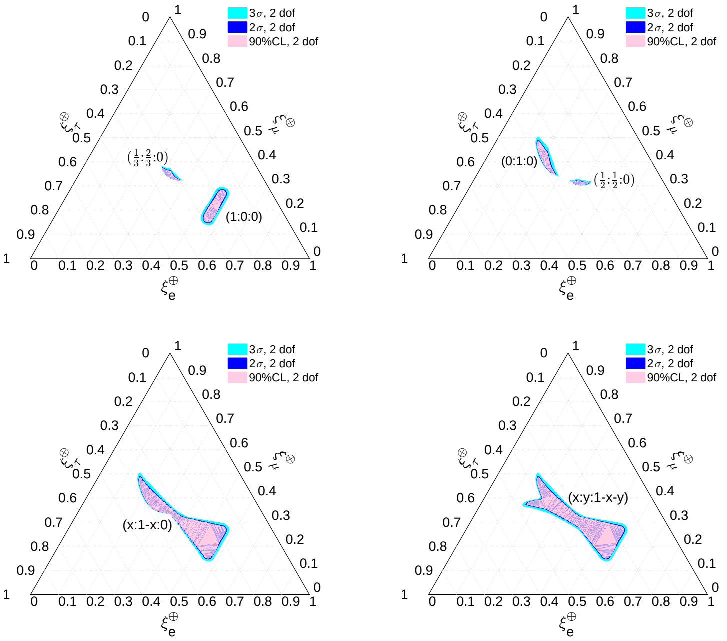

Figure 4.1: Two-dimensional projections of the allowed regions from the global analysis of oscillation data from Ref. [3] in the relevant combinations giving the flavor content at the Earth. The allowed regions are shown at 90%, 95% and 3σ CL. In the upper panels we show the regions for four initial flavor compositions $(\xi_e^s : \xi_\mu^s : \xi_\tau^s) = (\frac{1}{3} : \frac{2}{3} : 0)$, $(1 : 0 : 0)$, $(0 : 1 : 0)$, and $(\frac{1}{2} : \frac{1}{2} : 0)$. In the lower panel the regions are shown for the more general scenarios, $(\xi_e^s : \xi_\mu^s : \xi_\tau^s) = (x : 1 - x : 0)$ for $0 \leq x \leq 1$, and $(\xi_e^s : \xi_\mu^s : \xi_\tau^s) = (x : y : 1 - x - y)$ for $0 \leq x, y \leq 1$.

deviations for the case when the flavor content at the source is $(1 : 0 : 0)$ [155] and $(0 : 1 : 0)$.

4.2 Effect of NSI on the Flavor Composition

The standard theoretical framework for the NP considered here is provided by non-standard interactions affecting neutrino interactions in the Earth matter. They can be described by effective four-fermion operators of the form

$$\mathcal{L}_{\mathrm{NSI}} = -2\sqrt{2} G_F \varepsilon_{\alpha\beta}^{fP} (\bar{\nu}_\alpha \gamma^\mu L \nu_\beta)(\bar{f}\gamma_\mu P f)\,, \tag{4.7}$$

where f is a charged fermion, $P = (L, R)$ and $\varepsilon_{\alpha\beta}^{fP}$ are dimensionless parameters encoding the deviation from standard interactions. In here we only consider neutral current neutrino interactions since charged current interactions are subject to strong constraints from charged lepton processes. So Eq. (4.7) is a four-fermion interaction similar to the effective low energy limit of the standard electroweak interactions but where we have now introduced the possibility of lepton flavour and universality violation in the interactions.

For astrophysical neutrinos NSI can affect the flavour ratio at the detector via the coherent scattering of the neutrinos when crossing the Earth as well as via non-coherent interactions with the Earth matter as we describe next.

4.2.1 Modified Matter Potential

Coherent neutrino scattering involves only the vector part of the four fermion interactions. In the Standard Model this leads to the appearance of an effective potential difference for ν_e's when traversing matter as described in Sec. 2.1.3. In the presence of NSI we will have to introduce a non-standard matter potential [156]

$$V_{\mathrm{NSI}} = \sqrt{2} G_F \sum_{f=e,u,d} N_f(r) \begin{pmatrix} \varepsilon^f_{ee} & \varepsilon^f_{e\mu} & \varepsilon^f_{e\tau} \\ \varepsilon^{f*}_{e\mu} & \varepsilon^f_{\mu\mu} & \varepsilon^f_{\mu\tau} \\ \varepsilon^{f*}_{e\tau} & \varepsilon^{f*}_{\mu\tau} & \varepsilon^f_{\tau\tau} \end{pmatrix} . \tag{4.8}$$

in addition to the standard matter potential in Eq. (2.17). The non-standard interactions with fermion f are accounted by the $\varepsilon^f_{\alpha\beta}$ coefficients with $\varepsilon^f_{\alpha\beta} = \varepsilon^{fL}_{\alpha\beta} + \varepsilon^{fR}_{\alpha\beta}$. Here $N_f(r)$ is the number density of fermions f in the Earth matter. In practice, the PREM model [157] fixes the neutron/electron ratio to $Y_n = 1.012$ in the Mantle and $Y_n = 1.137$ in the Core, with an average $Y_n = 1.051$ all over the Earth. Thus we get an average up-quark/electron ratio $Y_u = 3.051$ and down-quark/electron ratio $Y_d = 3.102$. We can therefore define:

$$\varepsilon_{\alpha\beta} \equiv \sum_{f=e,u,d} \left\langle \frac{Y_f}{Y_e} \right\rangle \varepsilon^f_{\alpha\beta} = \varepsilon^e_{\alpha\beta} + Y_u\, \varepsilon^u_{\alpha\beta} + Y_d\, \varepsilon^d_{\alpha\beta} \tag{4.9}$$

so that the non-standard matter potential can be written as:

$$V_{\mathrm{NSI}} = \sqrt{2} G_F N_e(r) \begin{pmatrix} \varepsilon_{ee} & \varepsilon_{e\mu} & \varepsilon_{e\tau} \\ \varepsilon^*_{e\mu} & \varepsilon_{\mu\mu} & \varepsilon_{\mu\tau} \\ \varepsilon^*_{e\tau} & \varepsilon^*_{\mu\tau} & \varepsilon_{\tau\tau} \end{pmatrix} . \tag{4.10}$$

Generically the flavor transition amplitudes in Eq. (4.2) are obtained by solving the neutrino and antineutrino evolution equations for the flavor wave function

$\boldsymbol{\nu}(x) = \{\nu_e(x), \nu_\mu(x), \nu_\tau(x)\}^T$

$$i\frac{d\boldsymbol{\nu}(x)}{dx} = H_\nu^{s\to\oplus}\,\boldsymbol{\nu}(x)\,, \qquad i\frac{d\bar{\boldsymbol{\nu}}(x)}{dx} = H_{\bar{\nu}}^{s\to\oplus}\,\bar{\boldsymbol{\nu}}(x) \tag{4.11}$$

for evolution between the source and the Earth surface and

$$i\frac{d\boldsymbol{\nu}(x)}{dx} = H_\nu^{\oplus\to d}\,\boldsymbol{\nu}(x)\,, \qquad i\frac{d\bar{\boldsymbol{\nu}}(x)}{dx} = H_{\bar{\nu}}^{\oplus\to d}\,\bar{\boldsymbol{\nu}}(x)\,, \tag{4.12}$$

for evolution in the Earth matter. They are in a similar form as Eq. (2.19) but now we are dealing with three neutrino flavors.

In here we are interested in standard vacuum oscillation dominating the propagation from the source to the detector but allowing for new physics in the interactions of the neutrinos in the Earth matter. In this case

$$H_\nu^{s\to\oplus} = (H_{\bar{\nu}}^{s\to\oplus})^* = H_{\rm osc} = U D_{\rm vac} U^\dagger \quad \text{with} \quad D_{\rm vac} = \frac{1}{2E}\,{\rm diag}(0, \Delta m_{21}^2, \Delta m_{31}^2)\,. \tag{4.13}$$

While

$$H_\nu^{\oplus\to d} \simeq H_{\rm mat}\,, \qquad H_{\bar{\nu}}^{\oplus\to d} \simeq -H_{\rm mat}^* \tag{4.14}$$

where the $\simeq$ corresponds to neglecting vacuum oscillations inside the Earth which is a very good approximation for the relevant neutrino energies ($\gtrsim 1$ TeV).

As discussed above NSI introduce additional non-standard matter potential. So the matter Hamiltonian can be written as the sum of Eq. (4.10) and Eq. (2.17), i.e.

$$H_{\rm mat} = \sqrt{2}G_F N_e(r) \begin{pmatrix} 1+\varepsilon_{ee} & \varepsilon_{e\mu} & \varepsilon_{e\tau} \\ \varepsilon_{e\mu}^* & \varepsilon_{\mu\mu} & \varepsilon_{\mu\tau} \\ \varepsilon_{e\tau}^* & \varepsilon_{\mu\tau}^* & \varepsilon_{\tau\tau} \end{pmatrix} \equiv W D_{\rm mat} W^\dagger \tag{4.15}$$

where

$$D_{\rm mat} = \sqrt{2}G_F N_e(r)\,{\rm diag}(\varepsilon_1, \varepsilon_2, \varepsilon_3). \tag{4.16}$$

where W is a 3×3 unitary matrix containing six physical parameters, three real angles and three complex phases. So without loss of generality the matter potential contains eight parameters, five real and three phases (as only difference of ε_i enter the flavor transition probabilities, only differences in the $\varepsilon_{\alpha\alpha}$ are physically relevant for neutrino oscillation data). The standard model interactions are encoded in the first term of ee entry (i.e. the 1 in $1+\varepsilon_{ee}$) in Eq. (4.15).

Altogether the flavor transition probabilities from a source at distance L

are

$$P_{\alpha\beta}^{s\to d}(E) = \sum_{\gamma\eta kl} W_{\beta k} W_{\beta l}^* W_{\gamma l} W_{\eta k}^* \exp(-i d_e \Delta\varepsilon_{kl}) \sum_{ij} U_{\eta i} U_{\gamma j}^* U_{\alpha j} U_{\alpha i}^* \exp(-i \frac{\Delta m_{ij}^2}{2E} L)\,, \tag{4.17}$$

$$P_{\alpha\beta}^{s\to\oplus}(E) = \sum_{ij} U_{\beta i} U_{\beta j}^* U_{\alpha j} U_{\alpha i}^* \exp(-i \frac{\Delta m_{ij}^2}{2E} L) \tag{4.18}$$

where $\Delta\varepsilon_{kl} = \varepsilon_k - \varepsilon_l$. Again we can average out the vacuum oscillation terms:

$$\begin{aligned} P_{\alpha\beta}^{s\to d}(E) = &\sum_i |U_{\alpha i}|^2 |U_{\beta i}|^2 - 2 \sum_{\gamma\eta kli} \mathrm{Re}\left(W_{\beta k} W_{\beta l}^* W_{\gamma l} W_{\eta k}^* U_{\eta i} U_{\gamma i}^* |U_{\alpha i}|^2\right) \sin^2(d_e \frac{\Delta\varepsilon_{kl}}{2}) \\ &+ \sum_{\gamma\eta kli} \mathrm{Im}\left(W_{\beta k} W_{\beta l}^* W_{\gamma l} W_{\eta k}^* U_{\eta i} U_{\gamma i}^* |U_{\alpha i}|^2\right) \sin(d_e \Delta\varepsilon_{kl})\,, \end{aligned} \tag{4.19}$$

$$P_{\alpha\beta}^{s\to\oplus}(E) = \sum_i |U_{\alpha i}|^2 |U_{\beta i}|^2\,. \tag{4.20}$$

In these expressions we have introduced the dimensionless normalization for the matter potential integral along the neutrino trajectory in the Earth

$$d_e(\Theta_z) \equiv \int_0^{2R\cos(\pi-\Theta_z)} \sqrt{2} G_F N_e(r) dx\,, \quad \text{with} \quad r = \sqrt{R_\oplus^2 + x^2 + 2R_\oplus x \cos\Theta_z}\,, \tag{4.21}$$

which we plot in Fig. 4.2. The integral includes both the effect of the increase length of the path in the Earth and the increase average density which is particular relevant for trajectories crossing the core and leads to the higher slope of the curve for $\cos\Theta_z \lesssim -0.84$.

We have now rederived Eq. (4.5) as Eq. (4.20), but with a more general formalism. We notice that the total coherent flavor transition probability remains energy independent even in the presence of NSI. Also the last term in Eq. (4.19) does not change sign for antineutrinos since both the imaginary part of the combination of mixing matrices and the phase of the oscillating sin change sign for antineutrinos.[1] In other words, there is no CP violation even if all the phases in U and W are kept different from zero. These two facts render the flavor composition of the fluxes at the detector independent of the energy spectrum and the neutrino/antineutrino ratio at the source, as

---

[1] Indeed this term preserves CP but violates time reversal, as it is well known that Earth matter effects violate CPT.

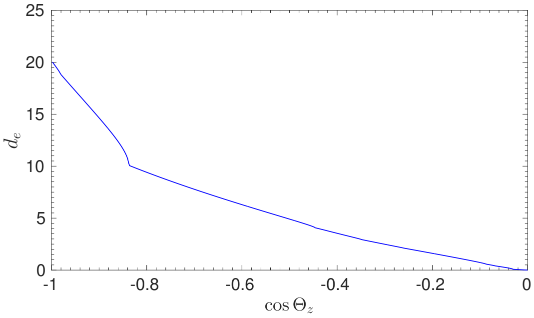

Figure 4.2: The normalized density integral d_e along the neutrino path as a function of the neutrino arrival zenith angle.

long as the flavor composition at the source is the same for both neutrinos and antineutrinos. This is just as the case for standard 3ν oscillations in the absence of NP.[2]

In brief, the effect of NSI in the Earth is to modify the flavor composition at the detector as compared to the standard case, in a way which depends on the zenith angle of the arrival direction of the neutrinos. Also, as expected, the effect only appears in presence of additional flavor mixing during propagation in the Earth, *i.e.*, for $W_{\alpha i} \neq C\delta_{\alpha i}$, which occurs only if some off-diagonal $\varepsilon_{\alpha\beta}$ (with $\alpha \neq \beta$) is different from zero.

In what follows we will present our results in terms of flavor ratios at the detector ξ^d_β, since, as we will demonstrate in the next section when discussing incoherent effects, they are good estimators of the reconstructed quantities $\xi^{\oplus,\mathrm{rec}}_\beta$ usually shown by the experimental collaborations. It is easy to show that:

$$\xi^d_\beta = \sum_\alpha P^{s\to d}_{\alpha\beta}(E)\xi^s_\alpha \tag{4.22}$$

where $P^{s\to d}_{\alpha\beta}(E)$ is obtained from Eq. (4.19). In principle, one may expect that the flavor ratios ξ^d_β would depend on the neutrino energy, either through the oscillation probability $P^{s\to d}_{\alpha\beta}(E)$ or though the intrinsic energy dependence of the flavor ratios at the source ξ^s_α. However, as we have seen in the previous discussion the expression in Eq. (4.19) is independent of E, and moreover we will assume (as it is customary to do) that the ratios ξ^s_α do *not* depend on the neutrino energy even though the fluxes $\phi^s_\alpha(E)$ do. Hence, the flavor ratios ξ^d_β are independent of energy and they can still be conveniently plotted in a ternary plot even in the presence of NSI.

---

[2] Relaxing the assumption of equal flavor composition for neutrinos and antineutrinos at the source can lead to additional interesting effects even in the case of standard oscillations as discussed in Ref. [154, 158].

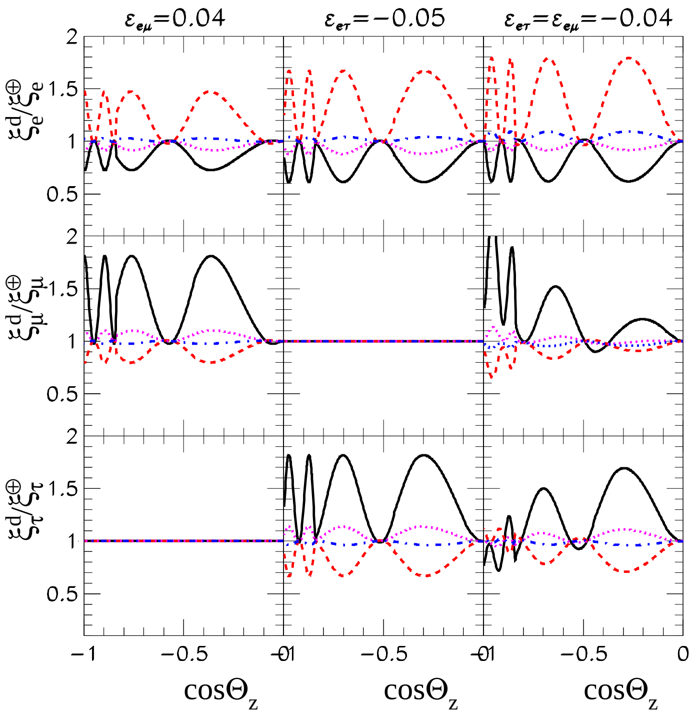

Figure 4.3: Flavor ratios at the detector as a function of the zenith angle of the neutrino normalized to the expectation in the absence of NSI and for oscillation parameters at the best fit of the global analysis ($\sin^2\theta_{12} = 0.305$, $\sin^2\theta_{13} = 0.0219$, $\sin^2\theta_{23} = 0.579$, and $\delta_{\rm CP} = 254°$). For the left (central) [right] panels the only non-vanishing NSI parameters are $\varepsilon_{e\mu} = 0.04$ ($\varepsilon_{e\tau} = -0.05$) [$\varepsilon_{e\mu} = \varepsilon_{e\tau} = -0.04$]. The different curves corresponds to different flavor composition at the source: $(\xi_e^s : \xi_\mu^s : \xi_\tau^s) = (1 : 0 : 0)$ (full black), $(0 : 1 : 0)$ (dashed red), $(\frac{1}{2} : \frac{1}{2} : 0)$ (dotted blue), and $(\frac{1}{3} : \frac{2}{3} : 0)$ (dash-dotted purple).

As discussed in the previous section NSI in the Earth modify these predictions and, unlike for NP effects in the propagation from the source, such Earth-induced modifications are a function of the arrival zenith angle of the neutrino. As illustration we show in Fig. 4.3 the variation of the flavor ratios at the detector as a function of the zenith angle of the neutrino for some values of the $\varepsilon_{\alpha\beta}$ well within the presently allowed 90% CL ranges. In our convention $\cos\Theta_z = -1$ corresponds to vertically upcoming neutrinos (which have crossed the whole Earth before reaching the detector) while $\cos\Theta_z = 0$ corresponds to horizontally arriving neutrinos (for which effectively no Earth matter is crossed so that $\xi^d_\beta(\cos\Theta_z = 0) = \xi^\oplus_\beta$). From Fig. 4.3 we can observe the main characteristics of the effect of NSI in the Earth matter. Deviations

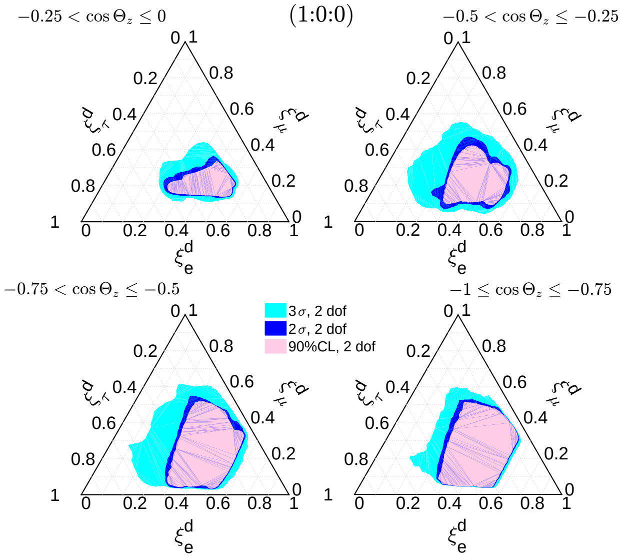

Figure 4.4: Allowed regions for the flavor ratios in the presence of NSI in the Earth at 90, 95% and 3σ CL for an initial flavor $(\xi^s_e : \xi^s_\mu : \xi^s_\tau) = (1 : 0 : 0)$. The four triangles correspond to averaging over neutrinos arriving with directions given in the range $0 \geq \cos\Theta_z > -0.25$ (upper left), $-0.25 \geq \cos\Theta_z > -0.5$ (upper right) $-0.5 \geq \cos\Theta_z > -0.75$ (lower left), and $-0.75 \geq \cos\Theta_z \geq -1$ (lower right).

are sizable for flavor α as long as $\varepsilon_{\beta\neq\alpha}$ is non-zero and ξ^s_α or ξ^s_β are non-zero. Larger effects are expected for source flavor compositions for which vacuum oscillations from the source to the Earth lead to "less equal" ratios at the Earth surface: $(1 : 0 : 0)$ and $(0 : 1 : 0)$. Finally the increase in frequency for almost vertical neutrino direction is a consequence of the increase of the integral density d_e for core crossing trajectories (see Fig. 4.2).

Next we show how the allowed regions in the ternary plots shown in Fig. 4.1 are modified when including the effect of the NSI presently allowed at given CL. In order to do so we project the χ^2 of the global analysis of oscillation data in the presence of arbitrary NSI on the relevant combinations entering in the flavor ratios within a given CL. The results are shown in Fig. 4.4, Fig. 4.5 and Fig. 4.6 for the flavor compositions at source $(\xi^s_e : \xi^s_\mu : \xi^s_\tau) = (1 : 0 : 0)$, $(0 : 1 : 0)$ and $(\frac{1}{3} : \frac{2}{3} : 0)$, respectively. The results are shown averaged over four zenith angular directions.

Comparing the allowed regions in Fig. 4.4 and Fig. 4.5 with the corresponding ones for $(1 : 0 : 0)$ and $(0 : 1 : 0)$ compositions in the case of standard 3ν oscillations given in Fig. 4.1 we see that the flavor ratios can take now much wider range of values in any of the zenith angle ranges considered.

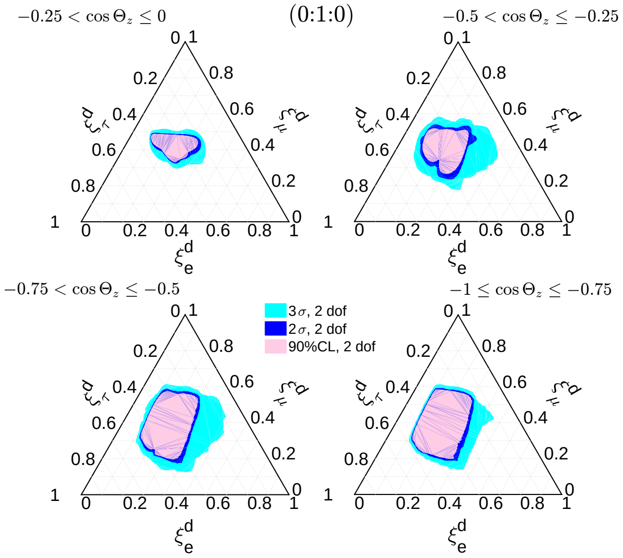

Figure 4.5: Same as Fig. 4.4 for $(\xi_e^s : \xi_\mu^s : \xi_\tau^s) = (0 : 1 : 0)$.

Moreover, although sizable deviations from $(\xi_e^d : \xi_\mu^d : \xi_\tau^d) = (\frac{1}{3} : \frac{1}{3} : \frac{1}{3})$ are possible, the allowed regions now extend to include $(\frac{1}{3} : \frac{1}{3} : \frac{1}{3})$ at CL of 3σ or lower. We also see that the larger CL region becomes smaller for most vertical arrival directions (see the relative size of the light blue regions in the two lower triangles on these figures). This is so because at those CL for the larger values of ε allowed the NSI-induced oscillations are fast enough to be averaged out $\langle \sin^2(\Delta\varepsilon_{ij}\frac{d_e}{2})\rangle \sim \frac{1}{2}$ for those trajectories while the value in the second most vertical angular bin can be in average larger than $1/2$. For contrast, as illustrated in Fig. 4.6, for the case of flavor composition at the source $(\xi_e^s : \xi_\mu^s : \xi_\tau^s) = (\frac{1}{3} : \frac{2}{3} : 0)$ NSI in the Earth never induce sizable modifications of the expectation $(\xi_e^d : \xi_\mu^d : \xi_\tau^d) = (\frac{1}{3} : \frac{1}{3} : \frac{1}{3})$.

4.2.2 Incoherent Effects

In addition to the coherent effects discussed so far, high-energy neutrinos propagating through the Earth can also interact inelastically with the Earth matter either by charged current or by neutral current interactions. In charged current interactions leptons are generated at a price of the loss of incoming neutrinos. Among these leptons, electrons are stable and can be absorbed into the Earth matter. Muons may radiate away energy through various reactions before decaying back to neutrinos. Taus, on the other hand, regenerate tau neutrinos with electron or muon neutrinos from decay because of their short lifetime. As a consequence of these inelastic processes the neutrino flux is at-

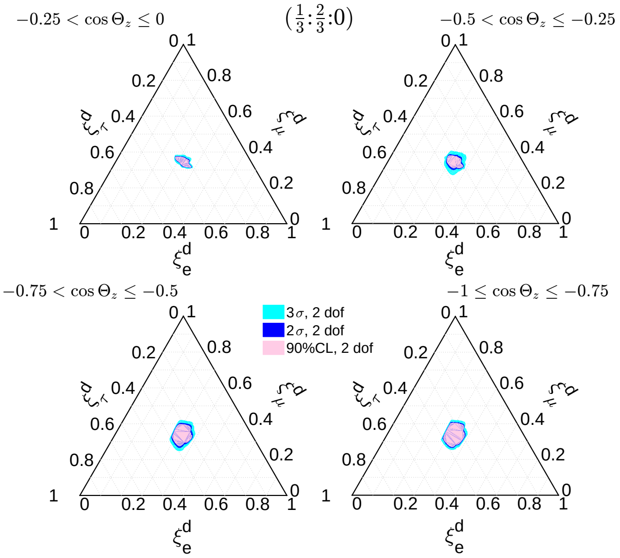

Figure 4.6: Same as Fig. 4.4 for $(\xi_e^s : \xi_\mu^s : \xi_\tau^s) = (\frac{1}{3} : \frac{2}{3} : 0)$.

tenuated, its energy is degraded, and secondary fluxes are generated in charged current interactions.

The most convenient way to describe neutrino flavor oscillation in the presence of the incoherent effects is the density matrix formalism which evolves the neutrino ensemble in terms of density matrix ρ. A careful treatment of the attenuation, regeneration and energy degradation of the high energy neutrino fluxes with the density matrix formalism can be found in Ref. [159] (see also Ref. [160]) where the evolution of neutrino fluxes is described by a set of integro-differential equations. Here instead we use the software package nuSQuIDS [161] with the integro-differential equations built in. Given the neutrino fluxes at the source and the physics during propagation, nuSQuIDS will output the neutrino fluxes at the detector. The nuSQuIDS code is then modified to be adapted to the new physics which we have introduced. With this tool at hand, we show the flavor ratios at the detector including incoherent effects in Fig. 4.7. This figure is not very different from Fig. 4.3 except that incoherent effects are included for the colored curves. Different curves correspond to different neutrino flux energies at the source. We only show the results for the case of the flavor composition $(\xi_e^s : \xi_\mu^s : \xi_\tau^s) = (1 : 0 : 0)$ at the source but the results for other flavor compositions are not very different. For comparison we also plot the detected flavor composition without incoherent effects as the black curve. The colored curves cluster together and it is hard to distinguish one from another. This means the dependence of incoherent effects on neutrino energy is only moderate. Though there is some difference between the colored and black curves, we don't observe drastic change when including incoherent effects. Thus we conclude our coherent scattering is still good approximation for the detected flavor composition.

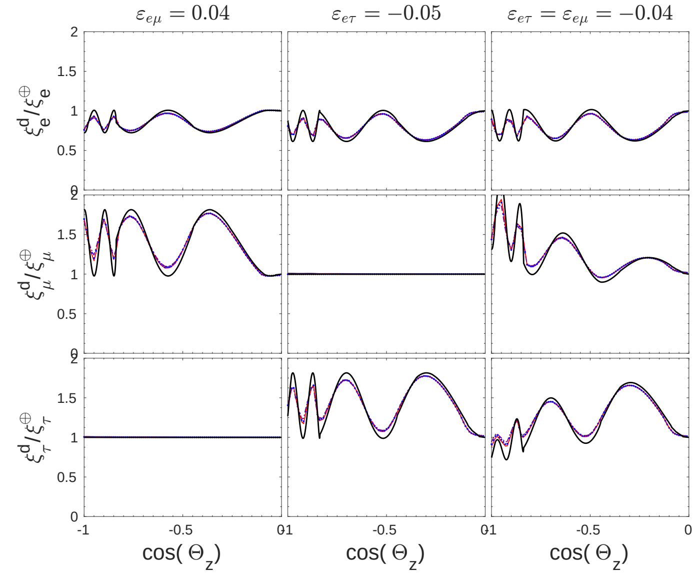

Figure 4.7: Same as Fig. 4.3 but including incoherent effects for the colored curves. Only the flavor composition of (1 : 0 : 0) at the source is shown in the figure. The full black curve is the same as the full black curve in Fig. 4.3. The dashed red, dotted blue and dash-dotted purple corresponds to neutrino fluxes with energy 10^4 GeV, 10^6 GeV and 10^8 GeV respectively. These three curves show the flavor ratios at the detector when considering both NSI and incoherent effects.

This conclusion can also be understood qualitatively. For simplicity, let us first neglect NSI and focus only on the usual 3ν oscillation framework. In the standard scenario, attenuation and regeneration effects can be consistently described by a set of coupled partial integro-differential equations. In this case the fluxes at the arrival point in the Earth are given by Eq. (4.1) and (4.2) while for the fluxes at the detector we have:

$$\text{SM:} \qquad \mathcal{P}^{s\to d}_{\alpha\beta}(E,E') = \sum_{\gamma} P^{s\to\oplus}_{\alpha\gamma}(E) F^{\oplus\to d}_{\gamma\beta}(E,E')\,, \tag{4.23}$$

where $F^{\oplus\to d}_{\gamma\beta}(E,E')$ is the function accounting for attenuation and regeneration effects, which depends on the trajectory of the neutrino in the Earth matter (*i.e.*, it depends on Θ_z). Attenuation is the dominant effect and for most energies is only mildly flavor dependent. So the dominant incoherent effects verify

$$\text{SM:} \qquad F_{\gamma\beta}^{\oplus\to d}(E,E') \simeq \delta_{\gamma\beta} F_{\text{att}}^{\oplus\to d}(E)\delta(E-E')\,. \tag{4.24}$$

When considering NSI in the Earth the simple factorization of coherent and incoherent effects introduced in Eq. (4.23) does not hold, since NSI-induced oscillations, attenuation, and regeneration occur simultaneously while the neutrino beam is traveling across the Earth's matter. In order to properly account for all these effects we need to replace the evolution equation in the Earth (4.12) with a more general expression including also the incoherent components. This can be done by means of the density matrix formalism and we have already shown the quantitative results in Fig. 4.7. However, if one neglects the subleading flavor dependence of these effects and focus only on the dominant attenuation term, as we did in Eq. (4.24) for the standard case, it becomes possible to write even in the presence of NSI-oscillations:

$$\text{NSI:} \qquad \mathcal{P}_{\alpha\beta}^{s\to d}(E,E') \simeq P_{\alpha\beta}^{s\to d}(E) F_{\text{att}}^{\oplus\to d}(E)\delta(E-E') \tag{4.25}$$

with $P_{\alpha\beta}^{s\to d}(E)$ given in Eq. (4.19). In other words, although the presence of NSI affects the flavor composition at the detector through a modification of the *coherent* part of the evolution in the Earth, the *incoherent* part is practically the same in both the standard and the non-standard case and does not introduce relevant flavor distortions.

Experimentally $\xi_\beta^\oplus$ are *reconstructed* from the measured neutrino fluxes in the detector ϕ_α^d by *deconvoluting* the incoherent effects due to SM interactions in the Earth matter:

$$\xi_\beta^{\oplus,\text{rec}} \equiv \frac{\phi_\beta^{\oplus,\text{rec}}(E)}{\sum_\gamma \phi_\gamma^{\oplus,\text{rec}}(E)} \quad \text{with} \quad \phi_\beta^{\oplus,\text{rec}}(E) \equiv \sum_\gamma \int dE' G_{\gamma\beta}^{\oplus\leftarrow d}(E,E')\phi_\gamma^d(E') \tag{4.26}$$

where the function $G_{\alpha\beta}^{\oplus\leftarrow d}(E,E')$ is the inverse of the Earth attenuation + degradation + regeneration function $F_{\alpha\beta}^{\oplus\to d}(E,E')$ introduced before:

$$\sum_\gamma \int dE'' F_{\gamma\beta}^{\oplus\to d}(E,E'')\, G_{\alpha\gamma}^{\oplus\leftarrow d}(E'',E') = \delta_{\alpha\beta}\,\delta(E-E') \tag{4.27}$$

Under the approximation described in Eq. (4.24) $G_{\alpha\beta}^{\oplus\leftarrow d}(E,E')$ reduces to:

$$G_{\alpha\beta}^{\oplus\leftarrow d}(E,E') \simeq \delta_{\alpha\beta}\frac{1}{F_{\text{att}}^{\oplus\to d}(E)}\delta(E-E') \tag{4.28}$$

so that

$$\xi_\beta^{\oplus,\mathrm{rec}} \simeq \frac{\phi_\beta^d(E) \,/\, F_{\mathrm{att}}^{\oplus\to d}(E)}{\sum_\gamma \phi_\gamma^d(E) \,/\, F_{\mathrm{att}}^{\oplus\to d}(E)} = \frac{\phi_\beta^d(E)}{\sum_\gamma \phi_\gamma^d(E)} \equiv \xi_\beta^d \tag{4.29}$$

where we have introduced the flavor ratios at the detector ξ_β^d. Thus we have shown that the reconstructed flavor ratios at the surface of the Earth ($\xi_\beta^{\oplus,\mathrm{rec}}$) are well approximated by the measured flavor ratios at the detector (ξ_β^d). This conclusion depends only on the validity of the approximation (4.24), and therefore applies both for standard oscillations and in the presence of new physics such as Earth NSI. The qualitative discussion of incoherent effects here is consistent with the quantitative results shown in Fig. 4.7, i.e. incoherent effects don't modify the flavor ratios at the detector in an essential way.

4.3 Summary

The measurement of the flavor composition of the detected ultra-high energy neutrinos can be a powerful tool to learn about the mechanisms at work in their sources. Such inference, however, relies on the understanding of the particle physics processes relevant to the neutrino propagation from the source to the detector. The presence of NP effects beyond those of the well established mass-induced 3ν oscillations alters the flavor composition at the detector and can therefore affect the conclusions on the dominant production mechanism.

In this work we have focused on NP effects associated with NSI of the neutrinos in the Earth matter. The relevant flavor transition probabilities accounting for oscillations from the source to the Earth plus NSI in the Earth are energy independent but depend on the zenith angle of the arrival direction of the neutrinos, which is a characteristic feature of this form of NP. Quantitatively, we have shown that within the presently allowed range of NSI large deviations from the standard 3ν oscillation predictions for the detected flavor composition can be expected, in particular for fluxes dominated by one flavor at the source. On the contrary we find that the expectation of equalized flavors in the Earth for sources dominated by production via pion-muon decay-chain is robust even in the presence of this form of NP. Our results are based on coherent forward scattering but show robustness when including incoherent effects.

Chapter 5

Cosmological Neutrinos and New Interactions

Besides in astrophysical sources, neutrinos were also produced in the early universe. For a good part of its history these *cosmological neutrinos* are maintained in equilibrium with the primordial plasma through electroweak interactions. As the universe cools down, their interactions become less efficient. Eventually when neutrinos are not able to maintain equilibrium they decouple from the plasma. Furthermore if the masses of neutrinos are larger than the neutrino temperature of about 1.9 K (or equivalently 1.7×10^{-4} eV), they must experience a transition from being relativistic to being non-relativistic sometime along the history of the universe. The thermalization between neutrinos and the plasma in the early universe predicts a number density of about 113 relic neutrinos per cm^3 today, making them the second most abundant species in the universe, right after photons. These relic neutrinos make up what is referred to as *the cosmic neutrino background*.

As an important component in cosmology, both the contribution of neutrinos to the total energy density and their effect on its perturbations leave imprints on the the evolution of the universe. Consequently current cosmological observations put important constraints on the properties of neutrinos.

Additional light neutrinos have been invoked to explain some anomalies in the short baseline oscillation experiments. Cosmological data however sets very tight constraints on the parameter space for additional neutrino species which results into severe tensions with those required to explain the short baseline oscillation anomalies. In this chapter, we will study the possibility of relieving the tension between eV sterile neutrinos and cosmological observations by introducing new interactions in the sterile sector.

5.1 A Neutrinoless Universe

To study the role of neutrinos in cosmology, we first present a brief review of the evolution history of the universe. For illustration purpose we don't include neutrinos here but rather restore them in the next section. We start with a homogeneous and isotropic universe in Sec. 5.1.1 and describe the perturbations on this background universe Sec. 5.1.2. This section is based on Refs. [162–164].

5.1.1 The Expanding Universe

You may have looked up at the clear night sky when you were a child and found that there are countless stars shinning above your head. Someone standing beside you may tell you the names of the constellations one by one. If at that time you are asked the question whether the universe is the same when comparing any two directions, you may answer no without hesitation. But wait! Think twice before you answer. If we average over scales way larger than galaxy clusters, any two directions become similar. This is even better illustrated by the comic microwave background (CMB) data, which shows that the spectrum of relic photons produced in the early universe is that of a black body with temperature of $T = 2.7255\text{K}$ in all directions. The temperature fluctuations of the CMB over that black body spectrum are of 1 part of 10^5, regardless of the direction where the photons come from. This indicates that the universe is *isotropic*, i.e., there is no preferred direction in the universe. Furthermore, it is hard to believe that we are at the center of the universe, so if the universe is isotropic everywhere, it is also *homogeneous*, i.e., there is no special point. Still, you see one constellation different from another, and this lies in the more profound idea of inhomogeneity and anisotropy. We shall treat them as perturbations over a homogeneous and isotropic background.

The universe is also *expanding*. We know this because the stars outside the Milky Way are receding away from us. We introduce the scale factor $a(t)$ to trace the expansion of the universe. The expanding, homogeneous and isotropic universe can be described by the Friedmann-Robertson-Walker (FRW) metric where the spacetime interval can be written as

$$ds^2 = dt^2 - a^2(t)\left[\frac{dr^2}{1 - Kr^2} + r^2 d\Omega^2\right] \tag{5.1}$$

in polar coordinates. K is the curvature of the universe, and positive, zero, and negative curvatures correspond to a closed, flat and open universe respectively.

In Cartesian coordinates the spacetime interval is instead

$$ds^2 = dt^2 - a^2(t)\gamma_{ij}dx^i dx^j = g_{\mu\nu}dx^\mu dx^\nu \,, \tag{5.2}$$

where

$$\gamma_{ij} = \delta_{ij} + K\frac{x_i x_j}{1 - Kx^2} \,, \tag{5.3}$$

and the sum over μ and ν from 0 to 3 is implicit following Einstein's convention. i and j from 1 to 3 are indices of spacial coordinates only. In general, the metric $g_{\mu\nu}$ in Eq. (5.2) characterizes the geometry of spacetime. Using this notation one can immediately find

$$g_{00} = 1, \quad g_{0i} = g_{i0} = 0, \quad \text{and} \quad g_{ij} = a^2\gamma_{ij} \,. \tag{5.4}$$

The coordinates x^i are the comoving coordinates, which means they are measured by the comoving observer who follows the expansion of the universe. Similarly the comoving distance is the distance as measured by the comoving observer. It is also convenient to introduce the conformal time

$$d\tau = dt/a(t) \tag{5.5}$$

which is the comoving distance that light ($c = 1$ here) can travel in a time interval dt. To measure how fast the universe expands, we define the Hubble parameter as

$$H(t) \equiv \frac{1}{a}\frac{da}{dt} = \frac{\dot{a}}{a} \,, \tag{5.6}$$

(not to be confused with the Hamiltonian which we have used in the previous chapters). The Hubble parameter today is usually denoted by H_0, which is sometimes called Hubble constant (certainly the Hubble parameter may not be a constant as the universe expands). It is often useful to define another expansion parameter in terms of the derivative with respect to the conformal time, which is

$$\mathcal{H} \equiv \frac{1}{a}\frac{da}{d\tau} = \frac{a'}{a} \,. \tag{5.7}$$

To avoid confusion throughout this chapter we use an overdot to denote the derivative with respect to time and a prime to denote the derivative with conformal time. Using Eq. (5.5) we are able to relate H and $\mathcal{H}$ as $\mathcal{H} = aH$.

Conservation of Energy Momentum

The universe consists of matter (e.g. dark matter and baryons), radiation (e.g. photons and relativistic neutrinos) and dark energy. The homogeneity and isotropy require the components to be described by a perfect fluid, i.e., their energy-momentum tensor has the form

$$T_{\mu\nu} = (\rho + P)U_\mu U_\nu - P g_{\mu\nu} \,, \tag{5.8}$$

where ρ and P are the energy density and pressure of the fluid and the four velocity is defined as

$$U_\mu \equiv \frac{dx_\mu}{ds} \,. \tag{5.9}$$

We will show later that our universe today is quite flat, so let's just "keep it flat" for the moment. In the rest frame of the fluid, $U_\mu = (1, 0, 0, 0)$, and we see from Eq (5.8)

$$T_{\mu\nu} = \begin{pmatrix} \rho & 0 & 0 & 0 \\ 0 & P & 0 & 0 \\ 0 & 0 & P & 0 \\ 0 & 0 & 0 & P \end{pmatrix} . \tag{5.10}$$

In general relativity, the partial derivative ∂_μ is promoted to the covariant derivative ∇_μ. When acting on a vector V^ν,

$$\nabla_\mu V^\nu = \partial_\mu V^\nu + \Gamma^\nu_{\mu\lambda} V^\lambda \,, \tag{5.11}$$

where the Christoffel symbols

$$\Gamma^\mu_{\alpha\beta} = \frac{1}{2} g^{\mu\lambda} (\partial_\alpha g_{\beta\lambda} + \partial_\beta g_{\alpha\lambda} - \partial_\lambda g_{\alpha\beta}) \,. \tag{5.12}$$

With the covariant derivative we can write the conservation of energy-momentum in general relativity as

$$\nabla_\mu T^\mu{}_\nu = \partial_\mu T^\mu{}_\nu + \Gamma^\mu_{\mu\lambda} T^\lambda{}_\nu - \Gamma^\lambda_{\mu\nu} T^\mu{}_\lambda = 0 \,. \tag{5.13}$$

where

$$T^\mu{}_\nu = g^{\mu\rho} T_{\rho\nu} = (\rho + P) U^\mu U_\nu - P \delta^\mu_\nu \,. \tag{5.14}$$

It is important to note that energy-momentum conservation holds for each component that doesn't interact with other components in the universe since there is no energy-momentum transfer. For example, the energy-momentum of dark matter is conserved separately. Introducing Eqs. (5.4), (5.12) and (5.10) in Eq. (5.13) and evaluating the $\nu = 0$ component, we find

$$\rho' + 3\mathcal{H}(\rho + P) = 0 \,. \tag{5.15}$$

This is the *continuity* equation in general relativity which describes the evolution of the energy density. In general, the energy density and pressure of a fluid are related by the equation of state $P = w\rho$ so the evolution will be different for components characterized by different values of w:

- *Matter*. The pressure of dark matter and baryons is so small that we can approximate it by $w = 0$. Eq. (5.15) thus yields

  $$\rho_m \propto a^{-3}\,. \tag{5.16}$$

  This simply says that the matter density is diluted by the expansion of the universe in all three spatial dimensions.

- *Radiation*. For radiations $w = 1/3$ holds. Eq. (5.15) gives

  $$\rho_r \propto a^{-4}\,. \tag{5.17}$$

  Thus in an expanding universe, radiation cools down faster than matter does.

- *Dark energy*. The source of dark energy still remains mysterious. One possible candidate is the vacuum energy in quantum field theory. In many cases the energy density and pressure has the relation $P = -\rho$. Given this relation

  $$\rho_\Lambda = const\,. \tag{5.18}$$

Einstein Equation

The evolution of the metric is determined by the *Einstein* equation

$$G_{\mu\nu} = R_{\mu\nu} - \frac{1}{2}Rg_{\mu\nu} = 8\pi G T_{\mu\nu}\,, \tag{5.19}$$

where the Ricci tensor is

$$R_{\mu\nu} = \partial_\lambda \Gamma^\lambda_{\mu\nu} - \partial_\nu \Gamma^\lambda_{\mu\lambda} + \Gamma^\lambda_{\lambda\rho}\Gamma^\rho_{\mu\nu} - \Gamma^\rho_{\mu\lambda}\Gamma^\lambda_{\nu\rho}\,, \tag{5.20}$$

and the Ricci scalar

$$R = g^{\mu\nu}R_{\mu\nu}\,. \tag{5.21}$$

Recalling Eq. (5.12) it is not difficult to calculate the Ricci tensor and $G_{\mu\nu}$.

With the energy-momentum tensor in Eq. (5.10) we get two equations:

$$H^2 = \frac{8\pi G}{3}\rho - \frac{K}{a^2}\,, \tag{5.22}$$

$$\frac{\ddot{a}}{a} = -\frac{4\pi G}{3}(\rho + 3P)\,, \tag{5.23}$$

which are known as the *Friedmann* equations. The density and pressure sum up the contributions from all components in the universe. We can define the critical density as the energy density which would correspond to a given H in a flat universe

$$\rho_c = \frac{3H^2}{8\pi G}\,. \tag{5.24}$$

The critical density is a function of time since the Hubble parameter is not a constant. The critical density today

$$\rho_{c,0} = \frac{3H_0^2}{8\pi G}\,, \tag{5.25}$$

where H_0 is the Hubble parameter today. It is also customary to define the fraction of each component today as

$$\Omega_j \equiv \frac{\rho_{j,0}}{\rho_{c,0}}\,, \tag{5.26}$$

where j can be m (matter), r (radiation) and Λ (dark energy). We can also define the curvature density parameter

$$\Omega_K \equiv -\frac{K}{a_0^2 H_0^2}\,. \tag{5.27}$$

It follows that $\Sigma_j \Omega_j = 1$. A combining fit of Planck 2015 and other cosmological data yields $\Omega_K = 0.000 \pm 0.005$ at 95% CL [4], which essentially tells us the universe is very close to flat today. From now on we will just assume the universe is flat and set $K = 0$. Considering Eqs. (5.16), (5.17) and (5.18) we can track the energy density of different components back in time with their density today, hence Eq. (5.22) becomes

$$H^2 = H_0^2\left[\Omega_m\left(\frac{a}{a_0}\right)^{-3} + \Omega_r\left(\frac{a}{a_0}\right)^{-4} + \Omega_\Lambda\right]\,. \tag{5.28}$$

So as long as the present fractions Ω_i are non-zero, the universe begins in an era in which radiation dominates, and is later dominated by matter, and finally it is dominated by dark energy.

During the periods in which the energy density is dominated by one component, the different evolution stages can be obtained by solving Eq. (5.28):

- *Radiation domination:*
$$a \propto t^{1/2} \propto \tau \, . \tag{5.29}$$
- *Matter domination:*
$$a \propto t^{2/3} \propto \tau^2 \, . \tag{5.30}$$
- *Dark energy domination:*
$$a \propto e^{H_0 t} \propto \frac{1}{\tau_0 - \tau} \, . \tag{5.31}$$

In summary, in a matter or radiation dominated universe we have

$$a \propto t^{2/3(1+w)} \propto \tau^{2/(1+3w)} \, , \tag{5.32}$$

while in the dark energy dominated universe the simple power law no longer holds.

5.1.2 Inhomogeneities and Anisotropies

We have solved the metric evolution in the previous section within a single-component, homogeneous and isotropic universe. The metric is only characterized by the scale factor $a(t)$, which grows either as power law or as exponential of time t. However, inhomogeneities and anisotropies add complexity to this simple picture. In what follows we will introduce the effect of anisotropies and inhomogeneities and treat them as "perturbations" over an isotropic homogeneous "background".

In a universe with inhomogeneities and anisotropies, the metric is perturbed with

$$\delta g_{\mu\nu} = g_{\mu\nu} - \bar{g}_{\mu\nu} \, , \tag{5.33}$$

where $\bar{g}_{\mu\nu}$ is the metric in the background universe. The corresponding spacetime interval can be then written in terms of the perturbed metric as

$$ds^2 = a^2(\tau) \left[(1+2A) d\tau^2 - 2B_i dx^i d\tau - (\delta_{ij} + C_{ij}) dx^i dx^j \right] \, . \tag{5.34}$$

This can be compared with Eq. (5.4) where the spacetime dependent variables A, B and C all vanish. Generically these metric perturbations can be decomposed into scalar, vector and tensor components, but this parametrization is redundant and we always have the gauge freedom to choose a specific time slicing of the spacetime and reduce some of the parameters. Throughout this chapter we will adopt the conformal Newtonian gauge [165], which is more convenient when we discuss CMB and matter power spectrum. In this gauge, the metric is

$$ds^2 = a^2(\tau)\left[(1+2\Psi)d\tau^2 - (1-2\Phi)dx^i dx_i\right] \,, \tag{5.35}$$

where Ψ and Φ are known as the Bardeen potentials [166]. The vector and tensor perturbations are not explicit in the Newtonian gauge. This is a convenient gauge as in this thesis we only focus on the scalar perturbations which dominate the growth of inhomogeneities and anisotropies.

The energy-momentum tensor is also perturbed due to the perturbation of energy density, pressure and velocity. Moreover, there is one more ingredient– the anisotropic stress Σ—in an anisotropic universe which arises from the collisionless particles whose dynamics can not be described by a specific velocity in one direction, like photons or neutrinos. Without loss of generality, we can set $\Sigma^0_0 = \Sigma^i_0 = \Sigma^0_i = 0$ and $\mathrm{Tr}\Sigma = 0$, since otherwise these entries can be removed by the redefinition of the energy-momentum tensor and its perturbations. With the anisotropic stress, the energy-momentum tensor in Eq. (5.14) is perturbed as

$$\delta T^\mu{}_\nu = (\delta\rho + \delta P)\bar{U}^\mu \bar{U}_\nu + (\bar{\rho} + \bar{P})(\delta U^\mu \bar{U}_\nu + \bar{U}^\mu \delta U_\nu) - \delta P \delta^\mu_\nu - \Sigma^\mu_\nu \,. \tag{5.36}$$

The stress is always small and can be neglected most of the time during the evolution of the universe, however, as we will see in Sec. 5.2, it does leave some imprints on the the metric perturbations.

In the rest frame of the fluid we can relate the spacetime interval to the conformal time

$$ds = a(\tau)\sqrt{1+2\Psi}\, d\tau \,, \tag{5.37}$$

and evaluating the four-velocity explicitly using Eq. (5.9), we obtain

$$\begin{aligned} \delta T^0{}_0 &= \delta\rho \,, & (5.38)\\ \delta T^i{}_0 &= (\bar{\rho} + \bar{P})v^i \,, & (5.39)\\ \delta T^i{}_j &= -\delta P \delta^i_j - \Sigma^i_j \,, & (5.40) \end{aligned}$$

where have defined the perturbations to the fluid velocity as $v^i \equiv dx^i/d\tau$. We can again plug in the metric and energy-momentum tensor perturbations back to Eq. (5.13). Evaluating the $\nu = 0$ component and expanding in the small perturbations, at zeroth order we recover Eq. (5.15) for the mean pressure $\bar{P}$

and density $\bar{\rho}$. At first order, we find

$$\delta' + \left(1 + \frac{\bar{P}}{\bar{\rho}}\right)(\nabla \cdot \mathbf{v} - 3\Phi') + 3\mathcal{H}\left(\frac{\delta P}{\delta \rho} - \frac{\bar{P}}{\bar{\rho}}\right)\delta = 0\,, \tag{5.41}$$

where we define the overdensity $\delta \equiv \delta\rho/\bar{\rho}$. This is the perturbed continuity equation. We will not talk about inflation models in this thesis, but simple inflation models predict initial conditions with adiabatic fluctuations where the density and pressure perturbations have the relation

$$\frac{\delta P}{\delta \rho} = \frac{\bar{P}'}{\bar{\rho}'} = c_s^2\,, \tag{5.42}$$

where c_s is the sound speed of the fluid. We can also write Eq. (5.41) in Fourier space, where a general function in terms of spacial coordinates are transformed as

$$f(\boldsymbol{x}) = \int \frac{d^3k}{(2\pi)^3} e^{i\mathbf{k}\cdot\mathbf{x}} f(\mathbf{k})\,. \tag{5.43}$$

It follows that Eq. (5.41) has the form

$$\delta' + (1+w)(\theta - 3\Phi') + 3\mathcal{H}(c_s^2 - w)\delta = 0\,, \tag{5.44}$$

where we have also introduced the notation $\theta = ik^i v_i$ and used the equation of state $\bar{P} = w\bar{\rho}$. In Eq. (5.44) the overdensity, velocity and gravitational potential are functions of k and τ. It also benefits to evaluate the $\nu = i$ component of Eq. (5.13) where we arrive at the *Euler* equation

$$\theta' + \mathcal{H}(1 - 3c_s^2)\theta - \frac{k^2 c_s^2}{1+w}\delta + k^2\sigma - k^2\Psi = 0\,, \tag{5.45}$$

where the stress perturbation

$$\sigma \equiv -\frac{(\hat{k}_i \hat{k}^j - \frac{1}{3}\delta_i^j)\Sigma_j^i}{\bar{\rho} + \bar{P}}\,. \tag{5.46}$$

As we mentioned before, the energy-momentum conservation equations (5.15), (5.41), (5.45), apply to each decoupled component of the fluid independently.

The same expansion can also be applied to the Einstein equation. Evaluating the 00 component of Eq. (5.19), to the zeroth order we arrive at the first

Friedmann equation (5.22) for $\bar{\rho}$, i.e.

$$\mathcal{H}^2 = \frac{8\pi G}{3} a^2 \bar{\rho} \,. \tag{5.47}$$

And at first order,

$$k^2 \Phi + 3\mathcal{H}(\Phi' + \mathcal{H}\Psi) = -4\pi G \bar{\rho} a^2 \delta = -\frac{3}{2}\mathcal{H}^2 \delta \,, \tag{5.48}$$

where in the rhs we have introduced (5.47). Evaluating the $0i$ component, we get the equation

$$k^2(\Phi' + \mathcal{H}\Psi) = 4\pi G a^2 (\bar{\rho} + \bar{P})\theta \,. \tag{5.49}$$

And for traceless part of the ij equations we get

$$k^2(\Phi - \Psi) = 12 G a^2 (\bar{\rho} + \bar{P})\sigma \,, \tag{5.50}$$

where we have used the definition of σ in Eq. (5.46). Eq. (5.50) reveals the fundamental idea that in the absence of anisotropic stress, the two gravitational potentials are equal, i.e.

$$\Phi = \Psi \,. \tag{5.51}$$

We will discuss the effect of σ in the next section, but let us keep it 0 for now.

The last thing is to evaluate the trace part of Eq. (5.19). Again to the zeroth order we arrive at the second Friedmann equation (Eq. (5.23)) for $\bar{P}$ which can be rewrite as

$$2\mathcal{H}' + \mathcal{H}^2 = -8\pi G a^2 \bar{P} \,. \tag{5.52}$$

And at first order,

$$\Phi'' + \mathcal{H}(\Psi' + 2\Phi') + (2\mathcal{H}' + \mathcal{H}^2)\Psi + \frac{k^2}{3}(\Phi - \Psi) = 4\pi G a^2 \delta P \,. \tag{5.53}$$

Eqs. (5.48) (5.49) (5.50) and (5.53) are the perturbed Einstein equations.

Altogether when universe is dominated by a single component with $P = w\rho$ (so for that dominating component we can approximate c_s^2 by w) substituting the Friedmann Equations (5.47), and (5.52), together with Eq. (5.48) into Eq. (5.53), we obtain the evolution equation for the gravitational potential

$$\Phi'' + 3(1 + w)\mathcal{H}\Phi' + w k^2 \Phi = 0 \,. \tag{5.54}$$

while for the density perturbations, using Eq. (5.48), one gets

$$\delta = -\frac{2k^2}{3\mathcal{H}^2}\Phi - \frac{2}{\mathcal{H}}\Phi' - 2\Phi\,. \tag{5.55}$$

Let us introduce the comoving distance a signal can propagate within specific time:

$$d = \int_0^\tau v d\tau' \propto \tau\,. \tag{5.56}$$

In case the signal travels at a speed of light, d is called particle horizon, i.e., it shows the maximum distance particles have traveled within conformal time τ. It can be easily shown that τ is proportional to $1/\mathcal{H}$ in a matter or radiation dominated universe where $a \propto \tau^n$. Therefore $d \propto 1/\mathcal{H}$ characterizes the maximum scale which perturbations can propagate. We will see below that the gravitational potentials and perturbations behave differently over and inside the particle horizon. In case the perturbation travels like a sound wave with the sound speed c_s, we can show that $d \propto c_s/\mathcal{H}$ assuming constant c_s. This is also called the sound horizon. It is relevant for radiations undergoing acoustic oscillations in matter and radiation eras.

Superhorizon Limit

Superhorizon limit implies $k \ll \mathcal{H}$, so we can drop the term proportional to k^2 in Eq. (5.54). A trial solution $\Phi \propto \tau^p$ yields $p = 0$ or $p = 1 - 6(1+w)/(1+3w)$ (which is negative for $w = 0$ or $w = 1/3$). The solution indicates two modes for the evolution of Φ, one is the "growing" mode which indeed is constant, and the other one is the decaying mode which quickly decays to 0. Thus in the superhorizon scale the gravitational potentials remain constant.

As for the density perturbations, in the superhorizon limit the first term in Eq. (5.55) is neglected. Only the decaying mode contributes to Φ' so $\Phi'/\mathcal{H}$ also decays quickly. As a consequence,

$$\delta \simeq -2\Phi \propto const\,. \tag{5.57}$$

This applies for the radiation density fluctuations in a radiation dominated era and matter density fluctuations in a matter dominated era. Furthermore, if we started from adiabatic initial conditions for all components $\delta\rho_i/\rho_i'$ takes the same value, which using the continuity equation implies that $\delta_i/(1+w_i)$ takes the same value for all components (so $\delta_m = 3/4\delta_r$). Thus in this case both matter and radiation density fluctuations are constant in either the matter or radiation dominated era.

Dark energy only dominates the universe much later and has little affect on the CMB and matter power spectrum. As a consequence, we will not discuss dark energy dominated era in detail in this thesis.

Subhorizon Limit

In the subhorizon limit, the evolution is different depending on whether radiation or matter dominates the expansion.

- *Radiation dominated.* The evolution equation for gravitational potential is still Eq. (5.54) with $w = 1/3$, which has a solution

  $$\Phi(k,\tau) = -\frac{C(k)}{x^3}(\sin x - x\cos x)\,, \tag{5.58}$$

  where we have dropped a mode leading to infinite potential at $\tau = 0$. $C(k)$ is a positive function of k set by initial conditions and x is defined as $x \equiv k\tau/\sqrt{3}$. Inside the horizon $x \gg 1$ (remember $k \gg \mathcal{H} \sim 1/\tau$) and we have the approximation

  $$\Phi(k,\tau) \simeq -3C(k)\frac{\cos(k\tau/\sqrt{3})}{(k\tau)^2}\,. \tag{5.59}$$

  This is, in radiation era, the gravitational potential oscillates with an amplitude decaying with time.

  The density perturbation is dominated by that of radiation and we immediately find from Eq (5.55) that

  $$\delta_r \simeq -\frac{2k^2}{3\mathcal{H}^2}\Phi = 2C(k)\cos(k\tau/\sqrt{3})\,, \tag{5.60}$$

  where we only keep the first non-decaying term. Unlike gravitational potential, the radiation density undergoes oscillation with constant amplitude.

  As for the density of dark matter, at the time of interest dark matter is already decoupled from the fluid. As mentioned above, the energy-momentum tensor of any decoupled component is conserved separately, so we can combine the time derivative of Eq. (5.44) with Eq. (5.45) and Eq. (5.44) (both for with $w = c_s = 0$) and neglecting terms $\mathcal{O}(\mathcal{H}/k)$ to get the evolution equation for cold dark matter fluctuations

  $$\delta''_{\rm cdm} + H\delta'_{\rm cdm} = -k^2\Phi\,. \tag{5.61}$$

Plugging in Eq. (5.48) we find

$$\delta''_{\rm cdm} + H\delta'_{\rm cdm} - 4\pi G a^2 \bar{\rho}_{\rm cdm}\delta_{\rm cdm} \simeq 0\,. \tag{5.62}$$

In radiation or matter dominated universe, the Hubble parameter is related to the scale factor by

$$\frac{\mathcal{H}^2}{\mathcal{H}_0^2} = \frac{\Omega_m^2}{\Omega_r}\left(\frac{1}{y} + \frac{1}{y^2}\right)\,, \tag{5.63}$$

where $y \equiv a/a_{\rm eq}$ with $a_{\rm eq}$ as the scale factor at matter-radiation equality (one can easily verify this equation in the radiation or matter era from Eqs. (5.29) and (5.30)). Eq. (5.62) are solved with the solutions

$$\delta_{\rm cdm} \propto \begin{cases} 2+3y \\ (2+3y)\ln\left(\dfrac{\sqrt{1+y}+1}{\sqrt{1+y}-1}\right) - 6\sqrt{1+y} \end{cases}\,. \tag{5.64}$$

In the radiation era $y \ll 1$ and we are left with the mode $\delta_{\rm cdm} \propto \ln a$.

- *Matter dominated.* In the matter domination era Eq.(5.54) is further simplified with $w = 0$, i.e.

$$\Phi'' + \frac{6}{\tau}\Phi' = 0\,. \tag{5.65}$$

The gravitational potential Φ comes with a constant mode and a decaying mode proportional to τ^{-5}. The radiation density contrast can be obtained from the combination of Eq. (5.44) and Eq. (5.45) which yields

$$\delta''_r + \frac{1}{3}k^2\delta_r = -\frac{4}{3}k^2\Phi\,. \tag{5.66}$$

This is just the harmonic oscillator with a constant driving force. The solution is

$$\delta_r = D(k)\cos(k\tau/\sqrt{3}) + E(k)\sin(k\tau/\sqrt{3}) - 4\Phi\,, \tag{5.67}$$

where Φ is a constant.

As for matter fluctuations, in matter era matter perturbation dominates so we can use either Eq. (5.55) with a constant Φ and using that $\mathcal{H} \propto 1/\tau$ or use Eq.(5.62) which still holds but with $y \gg 1$. Either way we find the growing mode $\delta_{\rm cdm} \propto a \propto \tau^2$.

Let us summarize what we have discussed in this section. Outside the horizon, both gravitational potentials and density perturbations are frozen. Inside the horizon and during radiation era, gravitational potentials decay while radiation perturbation oscillates with a constant amplitude. Radiation perturbation continues to oscillate in the matter era, which induces acoustic peaks in the CMB temperature spectrum while gravitational potentials remain constant. On the other hand, inside the horizon, matter perturbation grows only logarithmically in the radiation era, but quickly becomes proportional to scale factor in the matter dominated era. The different behavior in matter and radiation eras form the shape of matter power spectrum. Furthermore light particles like baryons and neutrinos change from behaving as radiation to behave as matter as the universe evolve. For example in the early universe when the temperature is high, baryons couple tightly to photons and experience acoustic oscillations. However, after decoupling, baryons behave like dark matter and its perturbation grows as that of dark matter. The acoustic oscillation at baryon decoupling does leave some imprint in the clustering of matter (traced by galaxy clusters) today, which characterizes the scale of sound horizon in the baryon acoustic oscillation (BAO) measurements. As for neutrinos we discuss their effects next.

5.2 Effects of Neutrinos in Cosmology

In the previous discussion we have neglected neutrinos, especially we have neglected the neutrino anisotropic stress to make the gravitational potentials equal ($\Phi = \Psi$). However, as an ingredient in the universe, neutrinos play important roles in the expansion of the universe and the growth of matter perturbations.

In Sec. 5.2.1 we show the effects of neutrinos on CMB and big bang nucleosynthesis (BBN) due to the modification of the expansion rate of the universe, and in Sec. 5.2.2 we show how neutrinos suppress the structure formation at small scales. The discussions in this section are based on Refs. [164, 167].

5.2.1 Effects on Expansion Rate

Neutrino energy density and pressure enters the Friedman equations (Eqs. (5.22) and (5.23)) of an homogeneous and isotropic universe (these effects are usually denoted as “background” effects). This has the direct effect that the expansion rate has to be modified. For example the time of nucleosynthesis or of matter-radiation equality is changed.

In the early universe neutrinos are tightly coupled with electrons and baryons. The rate of the weak interactions can be approximated by

$$\Gamma_\nu = n_\nu \langle \sigma v \rangle \sim G_F^2 T^5 \,, \tag{5.68}$$

where G_F is Fermi constant. Neutrinos decouple when the interaction rate is comparable to the expansion rate, which in the radiation era is

$$\Gamma_\nu \sim H \sim \sqrt{G T^4} \,. \tag{5.69}$$

We see immediately from Eqs. (5.68) and (5.69) that neutrinos decouple at the temperature $T \sim 1$ MeV. After that neutrinos free-stream without interacting with the background plasma. Soon after neutrino decoupling the temperature drops below the mass of electrons, and electrons and positrons begin to annihilate to photons (and very few neutrinos). This enhances the temperature of photons (and hence that of all other particles in the plasma in equilibrium with the photons) relative to neutrinos. During annihilation, the total entropy

$$S \propto g_{*,s} T^3 \tag{5.70}$$

is conserved, where T is the temperature of the plasma and $g_{*,s}$ is the effective number of degrees of freedom defined as

$$g_{*,s} = \sum_{i=b} g_i + \frac{7}{8} \sum_{i=f} g_i \,, \tag{5.71}$$

which sums up the spin degree of freedom of bosons and fermions in thermal equilibrium. Before annihilation both photons, electrons and positrons are counted as relativistic species in the plasma (so $g_{*,s} = 11/2$), while after annihilation only photons remain ($g_{*,s} = 2$). Thus the conservation of entropy density implies that

$$T_\nu = \left(\frac{4}{11} \right)^{1/3} T_\gamma \,. \tag{5.72}$$

Therefore, after annihilation we can write the neutrino energy density as

$$\rho_\nu = \left[\frac{7}{8} \left(\frac{4}{11} \right)^{4/3} N_{\rm eff} \right] \rho_\gamma \,, \tag{5.73}$$

where ρ_γ is the energy density of photons. We have introduced $N_{\rm eff}$ as the effective number of neutrino species. Theoretical calculation predicts $N_{\rm eff} = 3.046$ (not exactly 3 due to the energy leak from e^+e^- annihilation to neutrinos). A deviation from this value has important effects on the big bang nucleosynthesis (BBN) and CMB, as we will see below.

Effects on BBN

In the early universe when temperature is much higher than 1 MeV, the primordial plasma consisting of photons, neutrinos, electrons and baryons is in thermal equilibrium. While being non-relativistic, protons and neutrons have the number density

$$n = g\left(\frac{mT}{2\pi}\right)^{3/2} e^{-m/T} . \tag{5.74}$$

Therefore, the ratio of number density for protons and neutrons in equilibrium is

$$\left(\frac{n_n}{n_p}\right)_{\text{eq}} = \left(\frac{m_n}{m_p}\right)^{3/2} e^{-Q_{np}/T} , \tag{5.75}$$

where $Q_{np} = m_n - m_p = 1.3$ MeV. The small mass difference is not important when it comes to the prefactor m_n/m_p, but it does make a big difference when it enters the exponential. Especially when the temperature drops below 1 MeV, the neutron-to-proton ratio decreases drastically. Neutrons and protons are balanced mainly though beta decay and inverse beta decay, say

$$\begin{aligned} n + \nu_e &\leftrightarrow p + e^- \\ n + e^+ &\leftrightarrow p + \bar{\nu}_e . \end{aligned} \tag{5.76}$$

The two interaction rates are equal and can be approximated by $\Gamma_{np} \propto G_F^2 T^5$ provided that $n_e = 2n_{\nu_e}$ since they share the same matrix element. In case neutrino number density deviates from this relation, the neutron-proton conversion rate

$$\Gamma_{np} \propto (1 + \bar{n}_{\nu_e}) T^5 , \tag{5.77}$$

where $\bar{n}_{\nu_e} = n_{\nu_e}/n^*_{\nu_e}$ is the electron neutrino number density normalized to the equilibrium number density $n^*_{\nu_e} = n_e/2$. At about 1 MeV the relativistic degree of freedom

$$g_* = 10.75 + \Delta N_{\text{eff}} , \tag{5.78}$$

where $\Delta N_{\text{eff}} = N_{\text{eff}} - 3.046$. In the matter dominated era, the total energy density $\rho_{\text{tot}} \propto g_* T^4$, and from the Friedmann equation (5.22) we see the Hubble rate $H \propto g_*^{1/2} T^2$. Neutrons freeze out from the plasma when the neutron-proton conversion rate becomes comparable to the the Hubble rate, and it is not difficult to find the freezing-out temperature

$$T_f \propto \left[\frac{g_*^{1/2}}{(1+\bar{n}_{\nu_e})/2} \right]^{1/3} . \tag{5.79}$$

It shows that both N_{eff} and electron neutrino number density can affect the time of neutron decoupling. A larger N_{eff} can increase the expansion rate of the universe, which increases the freezing-out temperature; on the other hand, larger number density of electron neutrinos tend to increase the neutron-proton conversion rate, postponing the time of decoupling. The neutron-to-proton ratio n_n/n_p is roughly frozen after neutron decoupling (a few neutrons decay, though) until the temperature drops below 0.1 MeV, when the synthesis of nuclei begin. Almost all the remaining neutrons are bounded in the nuclei, thus the neutron-to-proton ratio at decoupling is of crucial importance in the determination of the abundances of primordial elements.

Effects on CMB

The main effects on the CMB spectrum are associated with the modification of the time of matter-radiation equality. Given the dependence of different components on the scale factor, we can find the scale factor at matter-radiation equality as

$$\frac{a_{\text{eq}}}{a_0} = \frac{\Omega_\gamma + \widetilde{\Omega}_\nu}{\Omega_b + \Omega_{\text{cdm}}} . \tag{5.80}$$

Note that

$$\widetilde{\Omega}_\nu \equiv \frac{\rho_{\nu,\text{eq}}}{\rho_{c,0}} \frac{a_{\text{eq}}^4}{a_0^4} \tag{5.81}$$

is not the fraction of neutrino energy density today, but rather the energy density at equality extrapolated until today. This is because neutrinos are massive and may undergo non-relativistic transition in the matter dominated era. The matter-radiation equality happens at around $T_\gamma \sim 0.7$ eV when neutrinos with mass of order 1 eV or smaller are still relativistic. It follows that neutrinos contribute to the radiation energy density though N_{eff}. Thus a modification of N_{eff} will shift the time of matter-radiation equality. We will see below that this has important effects on the CMB spectrum.

Photons decouple at the temperature $T_\gamma \sim 0.3$ eV, when electrons and protons combine to form atoms and the universe becomes transparent to photons. This is an epoch called recombination at which time CMB photons began free-streaming and eventually form the spectrum we observe today. As we have seen in the previous section, photons undergo acoustic oscillations before decoupling, and induce peaks in the CMB temperature spectrum. The decoupling temperature is quite close to that of matter-radiation equality so recombination takes place right after entering matter radiation era. During radiation era and inside the horizon gravitational potentials decay. At recombination when radiation is still not negligible, gravitational potentials continue to decay, which acts as a driving force and enhances the anisotropy spectrum. This effect is not seen in Eq. (5.66) where we treat Φ as a constant, but does present if we keep the time derivatives as in Eq. (5.99). The effect is more significant when equality is closer to the time of recombination (otherwise deep inside the matter era gravitational potentials remain constant). At recombination neutrinos are still relativistic and should be counted as radiation. The presence of neutrinos increases the radiation density and postpones the time of equality. This enhances the peaks of CMB anisotropy spectrum at small scales (inside the horizon).

In addition, as we have seen from Eq. (5.67), the acoustic oscillation of photons are characterized by the size of sound horizon (we approximate it by $\tau/\sqrt{3}$ in that equation). Adding neutrinos changes the expansion history of the universe and affects the size of sound horizon at recombination. As a consequence, the CMB acoustic peaks also shift with different neutrino energy density.

5.2.2 Effects on Matter Perturbations

The main effect of neutrinos on matter perturbations is to suppress their amplitude at small scales. To understand the origin of this effect, let us begin by solving the equations for the density perturbations of the neutrinos density.

Neutrinos in equilibrium can be described by the Fermi-Dirac distribution

$$f_0(\epsilon) = \frac{g_\nu}{(2\pi\hbar)^3}\frac{1}{e^{E_\nu/(k_B T_\nu)}+1} = \frac{g_\nu}{(2\pi\hbar)^3}\frac{1}{e^{\epsilon/(k_B T_{\nu 0})}+1}\,, \tag{5.82}$$

where $\epsilon = aE_\nu = a\sqrt{p^2+m^2} = \sqrt{q^2+a^2m^2}$ with $q \equiv ap$. $T_{\nu 0}$ is the neutrino temperature today and after decoupling it is verified that $T_{\nu 0}/T_\nu = a$ assuming the scale factor today $a_0 = 1$. k_B is the Boltzmann constant. For neutrinos the spin degree of freedom $g_\nu = 1$.

In a universe with inhomogeneities and anisotropies neutrinos deviate from the equilibrium and the phase space distribution is perturbed as

$$f(x^i, q_j, \tau) = f_0(q)\left[1 + \mathcal{N}(x^i, q, n_j, \tau)\right]\,, \tag{5.83}$$

where $\hat{\mathbf{n}}$ marks the orientation of the momentum. The phase space distribution follows the neutrino Boltzmann equation

$$\frac{Df}{d\tau} = \frac{\partial f}{\partial \tau} + \frac{dx^i}{d\tau}\frac{\partial f}{\partial x^i} + \frac{dq}{d\tau}\frac{\partial f}{\partial q} + \frac{dn^i}{d\tau}\frac{\partial f}{\partial n^i} = \left(\frac{\partial f}{\partial \tau}\right)_C . \tag{5.84}$$

The right-hand side of the equation is induced by neutrino collisions. After neutrino decoupling, this term can be set to 0. The derivatives in the Boltzmann equation can be obtained from the geodesic equation

$$q^0 \frac{dq^\mu}{d\tau} + \Gamma^\mu_{\alpha\beta} q^\alpha q^\beta = 0 \, . \tag{5.85}$$

With this we can write the Boltzmann equation as

$$\frac{\partial \mathcal{N}}{\partial \tau} + i\frac{q}{\epsilon}(\boldsymbol{k}\cdot\hat{\mathbf{n}})\mathcal{N} + \frac{d\ln f_0}{d\ln q}\left[\Phi' - i\frac{\epsilon}{q}(\boldsymbol{k}\cdot\hat{\mathbf{n}})\mathcal{N}\right] = \frac{1}{f_0}\left(\frac{\partial f}{\partial \tau}\right)_C . \tag{5.86}$$

The corresponding energy-momentum tensor is the integral of phase space distribution, i.e.

$$T_{\mu\nu} = \int \frac{d^3q}{\sqrt{-g}} \frac{q^\mu q^\nu}{\epsilon} f \, , \tag{5.87}$$

where g is the determinant of the metric $g_{\mu\nu}$. We can thus relate the phase space perturbation to the perturbations in energy density and pressure. Specifically, for massless neutrinos we can expand the perturbation in terms of Legendre polynomials $P_l(\hat{\mathbf{k}}\cdot\hat{\mathbf{n}})$ where we define

$$F_\nu(\boldsymbol{k},\hat{\mathbf{n}},\tau) \equiv \frac{\int q^3 f_0 \mathcal{N} dq}{\int q^3 f_0 dq} = \sum_{l=0}^{\infty}(-i)^l(2l+1)F_{\nu l}(\boldsymbol{k},\tau)P_l(\hat{\mathbf{k}}\cdot\hat{\mathbf{n}}) \, . \tag{5.88}$$

Substituting it into Eq. (5.87) we find

$$\delta_\nu = F_{\nu 0} \, , \tag{5.89}$$

$$\theta_\nu = \frac{3}{4} k F_{\nu 1} \, , \tag{5.90}$$

$$\sigma_\nu = \frac{1}{2} F_{\nu 2} \, . \tag{5.91}$$

We can also work out the evolution equations from Eq. (5.86), where we obtain

$$\begin{aligned}
\delta'_\nu &= -\frac{4}{3}\theta_\nu + 4\Phi' \,, && (5.92)\\
\theta'_\nu &= k^2(\frac{1}{4}\delta_\nu - \sigma_\nu) + k^2\Psi \,, && (5.93)\\
F'_{\nu l} &= \frac{k}{2l+1}\left[lF_{\nu(l-1)} - (l+1)F_{\nu(l+1)}\right] \,, \quad l \geq 2 \,. && (5.94)
\end{aligned}$$

The above equations apply to relativistic neutrinos whose masses can be neglected. We can solve the equations in the superhorizon limit $k\tau \ll 1$ and find [163]

$$\begin{aligned}
\delta_\nu &= -2\Psi \,, && (5.95)\\
\theta_\nu &= \frac{1}{2}(k^2\tau)\Psi \,, && (5.96)\\
\sigma_\nu &= \frac{1}{15}(k\tau)^2\Psi \,, && (5.97)\\
\Phi &= (1 + \frac{2}{5}R_\nu)\Psi \,, && (5.98)
\end{aligned}$$

where $R_\nu \equiv \bar{\rho}_\nu/\bar{\rho}_r$. This is consistent with our discussion in the previous section that density perturbations are frozen outside the horizon. But we see from Eq. (5.98) that the neutrino stress does induce a small difference between the two potentials. Still for superhorizon scales the neutrino density perturbations are of the same order as those of the other components.

Inside the horizon, the perturbations are transferred to higher multiples which undergo fast oscillation and the overdensity is damped. We can also see this by combining Eq. (5.92) and (5.93), i.e.

$$\delta''_\nu + \frac{1}{3}k^2\delta_\nu = -\frac{4}{3}k^2\Psi + 4\Phi'' - \frac{4}{3}k^2\sigma_\nu \,. \tag{5.99}$$

This looks like Eq. (5.66) for radiation overdensity but now we have more terms corresponding to the derivative of potential and the anisotropic stress. σ_ν serves as the viscosity of the neutrino fluid which damps the oscillation of density contrast. In the radiation era an analytic solution is complicated because of Φ''. In the matter era the gravitational potentials approximately remain constant and we have

$$\delta_\nu = -4\Psi + C(k)\frac{\sin(k\tau)}{k\tau} \,. \tag{5.100}$$

The second term decays rapidly with time and we are left with a constant density perturbation proportional to the gravitational potential.

For massive neutrinos the simple relation $\epsilon = q$ doesn't hold. Instead, we expand the phase space perturbation $\mathcal{N}$ directly in terms of the Legendre series

$$\mathcal{N}(\boldsymbol{k}, \hat{\mathbf{n}}, q, \tau) = \sum_{l=0}^{\infty} (-i)^l (2l+1) \mathcal{N}_l(\boldsymbol{k}, q, \tau) P_l(\hat{\mathbf{k}} \cdot \hat{\mathbf{n}}) . \tag{5.101}$$

We can then obtain from Eq.(5.86) that

$$\begin{aligned} \mathcal{N}_0' &= -\frac{qk}{\epsilon}\mathcal{N}_1 - \Phi' \frac{d\ln f_0}{d\ln q} , & (5.102) \\ \mathcal{N}_1' &= \frac{qk}{3\epsilon}(\mathcal{N}_0 - 2\psi_2) - \frac{\epsilon k}{3q}\Psi \frac{d\ln f_0}{d\ln q} , & (5.103) \\ \mathcal{N}_l' &= \frac{qk}{(2l+1)\epsilon}[l\psi_{l-1} - (l+1)\mathcal{N}_{l+1}] , \quad l \geq 2 . & (5.104) \end{aligned}$$

By using Eq. (5.87) the perturbed energy density, pressure, velocity and shear stress of neutrinos are given by

$$\begin{aligned} \delta\rho_\nu &= 4\pi a^{-4} \int q^2 dq \epsilon f_0(q) \Psi_0 , & (5.105) \\ \delta P_\nu &= \frac{4\pi}{3} a^{-4} \int q^2 dq \frac{q^2}{\epsilon} f_0(q) \Psi_0 , & (5.106) \\ (\bar{\rho}_\nu + \bar{P}_\nu)\theta_\nu &= 4\pi k a^{-4} \int q^2 dq q f_0(q) \Psi_1 , & (5.107) \\ (\bar{\rho}_\nu + \bar{P}_\nu)\sigma_\nu &= \frac{8\pi}{3} a^{-4} \int q^2 dq \frac{q^2}{\epsilon} f_0(q) \Psi_2 . & (5.108) \end{aligned}$$

We can again combine the perturbed continuity equation (Eq. (5.44)) and Euler equation (Eq. (5.45)) to find the evolution of neutrino overdensity in the non-relativistic limit (neutrinos only become non-relativistic after radiation era), and it is not different from Eq. (5.61), i.e. the evolution of dark matter in matter era. The solution is similar to Eq. (5.64) which is

$$\delta_\nu = A(k) \ln\tau + B(k) - \frac{(k\tau)^2}{6}\Psi . \tag{5.109}$$

The constants are determined by matching Eq. (5.100) to the corresponding ones at the time at which neutrinos become non-relativistic. Let us introduce

$k_{\rm nr}$ that corresponds to the size of the horizon at the time at which neutrinos become non-relativistic. So if at that time a perturbation mode has entered the horizon (i.e. $k \geq k_{\rm nr}$), the matching is to the solution in Eq. (5.100) whose amplitude is small. From then now that δ_ν eventually grows as a like the behavior of dark matter but its amplitude is always smaller because it starts from a smaller value. On the other hand for perturbation modes which are still outside the horizon at the neutrino non-relativistic transition ($k < k_{\rm nr}$), the overdensity of neutrinos is determined by the "frozen" perturbation which has the same order as $\delta_{\rm cdm}$. Even for modes outside the horizon but later enter the horizon after non-relativistic transition, δ_ν begins to grow proportionally to a and it quickly becomes the same as the overdensity of the dark matter. So we conclude that neutrino overdensity is suppressed relative to that of dark matter at scales smaller than $k_{\rm nr}$.

All this leaves an imprint in the matter power spectrum. Let us recall Eq. (5.62) but restore $\delta\rho_{\rm cdm}$ as the total overdensity (i.e. keep the contribution from baryons and neutrinos), we have

$$\delta''_{\rm cdm} + \mathcal{H}\delta'_{\rm cdm} = 4\pi G a^2 \delta\rho\,. \tag{5.110}$$

We know from the previous discussion that for k corresponding to scales smaller than the size of the horizon at the time of the neutrino non-relativistic transitions $\delta_{\rm cdm} = \delta_b$ (δ_b is the baryon density contrast) and δ_ν grows less efficiently so we can approximate it by 0. On the other hand, neutrino energy density does contribute to the expansion rate via the Friedmann equation (Eq. (5.47)). After non-relativistic transition, it is more convenient to define the neutrino density fraction as

$$f_\nu \equiv \frac{\bar\rho_\nu}{\bar\rho_{\rm cdm} + \bar\rho_b + \bar\rho_\nu} = \frac{\Omega_\nu}{\Omega_m}\,, \tag{5.111}$$

where

$$\Omega_\nu \equiv \frac{\rho_{\nu,0}}{\rho_{c,0}} = \frac{\Sigma m_\nu n_\nu}{\rho_{c,0}}\,. \tag{5.112}$$

With this definition and recall the relation Eq. (5.30) we can rewrite Eq. (5.110) as

$$\delta''_{\rm cdm} + \frac{2}{\tau}\delta'_{\rm cdm} - \frac{6}{\tau^2}(1-f_\nu)\delta_{\rm cdm} = 0\,, \tag{5.113}$$

where f_ν is the density fraction of neutrinos defined in Eq. (5.111). The solution of Eq. (5.113) corresponds to a growing mode

$$\delta_{\rm cdm} \propto a^{1-3f_\nu/5}\,. \tag{5.114}$$

Compared with the solution without neutrinos where $\delta_{\rm cdm} \propto a$, the density contrast of dark matter is reduced. This simply says that the growth of matter perturbation are suppressed at scales which are smaller than the horizon at the time of the non-relativistic transition (i.e. for $k > k_{nr}$).

The matter power spectrum $P(k)$ is defined as $P(k) \equiv \langle \delta_m^2 \rangle$. A careful calculation gives [168]

$$\frac{P(k)^{f_\nu} - P(k)^{f_\nu=0}}{P(k)^{f_\nu=0}} \simeq -8 f_\nu \,, \tag{5.115}$$

which means the matter power spectrum is suppressed at those small scales, and the suppression depends on the masses of neutrinos.

In summary, we have seen that neutrinos are able to affect the evolution of the universe both at background and perturbation levels. With the current precision of cosmological observations both these effects can be constrained. As illustration we show in Fig. 5.1 the results of an analysis of Planck 2015 high multipole TT, EE, TE spectrum and low multipole temperature and polarization data, as well as lensing and BAO measurements in the framework of ΛCDM model with flexible neutrino masses and effective number of neutrino species $N_{\rm eff}$. We find the marginalized posterior of neutrino mass is $\Sigma m_\nu < 0.18$ eV at 95% CL and $N_{\rm eff} = 3.04 \pm 0.18$ at 68% CL. So this analysis puts tight constraints on additional neutrino species in the universe, especially for neutrinos heavier than this mass limit.

We will discuss in the next section how to reconcile additional massive neutrino species in cosmology by adding new interactions.

5.3 Sterile Neutrinos and New Interactions

Besides the three active neutrino flavors, anomalies in short baseline neutrino experiments also suggest the existence of addition sterile neutrino species. As we will show in Sec. 5.3.1, sterile neutrinos with mass of order eV is in tension with the cosmological observations. We introduce new interactions among sterile neutrinos to alleviate this tension in Sec. 5.3.2, and solve the quantum kinetic equations (QKEs) to quantify the effects of the new interactions in Sec. 5.3.3.

5.3.1 Short Baseline Anomalies and Sterile Neutrinos

Why are neutrinos massive? We know from neutrino oscillation experiments that neutrinos are not massless, but the mechanism of generating neu-

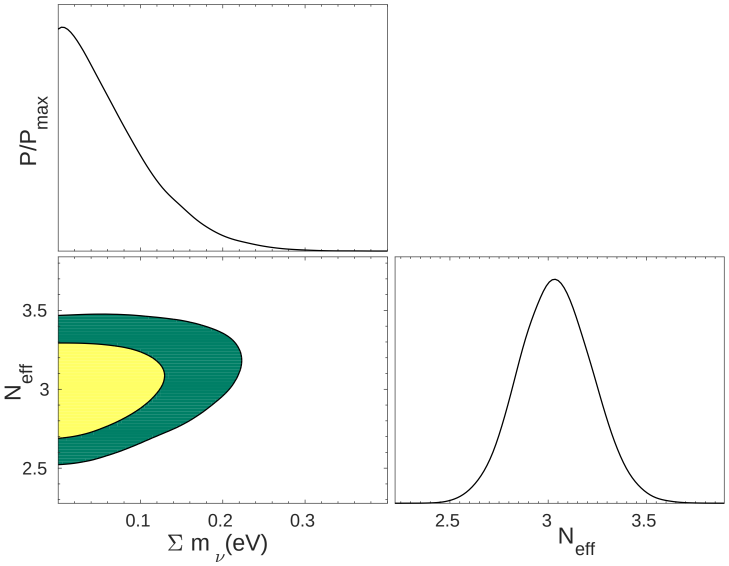

Figure 5.1: Posterior probability distribution of N_{eff} and the sum of neutrino masses. The data used is Planck 2015 high multipole TT, EE, TE spectrum and low multipole temperature and polarization data, as well as lensing and BAO measurements. The contours are allowed at 68% and 95% CL.

trino masses is still a missing piece in the Standard Model of particle physics. Of various models, the seesaw mechanisms are the most popular choices to accommodate massive neutrinos. In seesaw models, new particles have to be introduced to the Standard Model to break the $B-L$ gauge symmetry. Possible candidates for these new particles are right-handed neutrinos which are $SU(2)$ singlets. These neutrinos do not interact with particles in the framework of Standard Model and are also refer to as "sterile". Generically they are very heavy and they decouple well before any interesting epoch discussed in this thesis. However there are scenarios in which they can be light (with masses of the order of the three "active" neutrinos of the Standard Model). Such light sterile neutrinos can mix with active neutrinos and affect the neutrino flavor oscillation probabilities.

Indeed the existence of light sterile neutrinos has been invoked to explain some anomalies observed in neutrino oscillation experiments at short baselines. The first evidence came from the LSND experiment [169] which observed excess events of $\bar{\nu}_\mu \rightarrow \bar{\nu}_e$ oscillations. An excess was also observed in the antineutrino mode of MiniBooNE [170] which was consistent with the results of LSND, while the search for $\nu_\mu \rightarrow \nu_e$ oscillations reported excess only in the low energy range [171]. GALLEX [56, 172, 173] and SAGE[174] detected electron neutrinos produced by radioactive sources and observed deficit in the ν_e capture rates. The deficit is called Gallium anomaly. Furthermore, some reactor antineutrino measurements also reported deficit in the $\bar{\nu}_e$ flux [175] in the near detectors. These anomalies cannot be explained in the framework of three active neutrino oscillations. This can be understood from Eq. (2.16) where we write the neutrino flavor transition probability from one flavor to another flavor in the two neutrino case as

$$P_{\alpha\beta} = \sin^2 2\theta \sin^2 \left(1.27 \frac{\Delta m^2}{\mathrm{eV}^2} \frac{L}{\mathrm{km}} \frac{\mathrm{GeV}}{E} \right) , \tag{5.116}$$

Take LSND as example. The typical energy of the neutrinos produced by the accelerator is less than hundred MeV and the maximum mass difference of active neutrinos is $\Delta m^2 \sim 10^{-3}$ eV^2. We thus require the baseline L to be as long as hundred kilometers for significant oscillations to happen. However at LSND neutrinos travel only about 30 meters before reaching the detector. So the results can only be explained by introducing additional light neutrinos with much larger mass difference. We know from precision electroweak data that there are only three active (this is, with weak interactions) neutrinos. So any additional light neutrino states invoked to resolve these anomalies must be sterile.

There are several works in the literature which analyze these anomalies in such extended scenarios adding one (what is usually refereed to as 3+1 models) or two (3+2 models) sterile neutrinos. For example in Ref. [176] it was concluded that some reasonable fit could be found to explain these anomalies with a 4th neutrino of mass of the order $\mathcal{O}$(eV). For illustration we show in Fig. 5.2 the allowed range of $\Delta m^2_{41} \simeq \Delta m^2_{42} \simeq \Delta m^2_{43}$ vs the relevant combination of mixing angles from that analysis

Recently, Daya Bay collaboration [177] pointed out that the reactor antineutrino anomaly may be caused by the uncertainties in the expected neutrino fluxes, but a combined analysis of Daya Bay data with NEOS and DANSS experiments still allowed the parameter space for eV sterile neutrinos [178].

Besides the debate on the status of these hints towards light sterile neutrinos in oscillation experiments, the non-interacting light sterile neutrinos are also in great tension with cosmological observations. This is because light sterile neutrinos which mix with the active ones (as required to explain the oscillation anomalies) are in thermal equilibrium with active neutrinos in the early universe which results in $N_{\mathrm{eff}} \simeq 4$. As we have discussed at the end of the previous section, larger N_{eff} will enhance and shift the peaks in the CMB anisotropy spectrum. Furthermore, large sterile neutrino mass (compared with active neutrinos) will greatly suppress the matter power spectrum

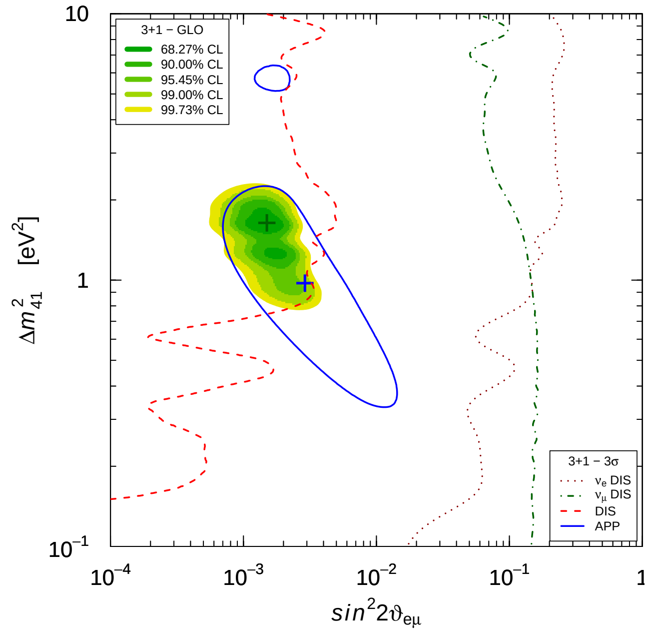

Figure 5.2: Allowed range of parameters for a 4th sterile neutrino to explain the short baseline anomalies.

at small scales. The combined analysis of Planck 2015 and other cosmological observations gives $N_{\text{eff}} = 3.04 \pm 0.18$ at 68% CL and $\Sigma m_\nu < 0.17$ eV at 95% CL [4] (which are also consistent with the results we have shown at the end of the previous section), manifesting the tension between eV sterile neutrinos and cosmology.

5.3.2 Introducing New Interactions

The tension with cosmology can be relieved by introducing new mechanisms, able to suppress the contribution of sterile neutrinos to the cosmological observables. One such possibility is that of new interactions between sterile neutrinos [179, 180], for example mediated by a new massive gauge boson X

$$\mathcal{L}_{\text{int}} = g_X \bar{\nu}_s \gamma_\mu \frac{1}{2}(1-\gamma_5)\nu_s X^\mu \,, \tag{5.117}$$

where g_X is the gauge coupling. In the energy scale smaller than the gauge boson mass M_X, we can integrate X out to obtain an effective four sterile neutrino interaction Lagrangian with effective coupling

$$\frac{G_X}{\sqrt{2}} = \frac{g_X^2}{8M_X^2}\,, \tag{5.118}$$

in total analogy with the weak Fermi constant.

The rate of the new interaction (analogous to Eq. (5.68) for weak interaction) is

$$\Gamma_X = n_{\nu_s}\langle\sigma v\rangle \simeq G_X^2 T_s^5\,, \tag{5.119}$$

where n_{ν_s} and T_s are the number density and temperature of the sterile neutrinos.

Likewise, the elastic forward scattering among the sterile neutrinos in the early universe generated by this interaction lead to an effective potential for the sterile neutrino in analogy to the MSW potential due to weak interactions of active neutrinos with any fermions in their background. The effective potential takes the form [181]

$$V_{\rm eff} = -\frac{8\sqrt{2}G_X\, p\,\varepsilon_s}{3M_X^2}\,, \tag{5.120}$$

where p is the momentum of the sterile neutrino and ε_s its energy density (in what follows we will use ε to denote energy density instead of ρ used in the previous sections to avoid confusion with the density matrix).

By introducing this effective potential the in-medium mixing angle between active and sterile neutrinos deviates from its vacuum value by (see Eq. (2.24))

$$\sin^2 2\theta_m \;=\; \frac{\sin^2 2\theta_0}{\left(\cos 2\theta_0 \;+\; 2E/{m_{\rm st}}^2\, V_{\rm eff}\right)^2 \;+\; \sin^2 2\theta_0}\,, \tag{5.121}$$

If $V_{\rm eff} \gg f_{\rm osc} = {m_{\rm st}}^2/(2E)$ before neutrinos decoupling from the primordial plasma, the in-medium mixing angle is highly suppressed and sterile neutrino production is deferred until after decoupling. This late production is significant since the entropy possessed by the three active neutrino species will be shared with the sterile neutrinos, which leads to a reduction in the total neutrino energy density. In the extreme case where each neutrino species achieves the equal number density after decoupling, their temperatures inferred from entropy conservation will be then $T_\nu = (3/4)^{1/3}\,(4/11)^{1/3}$ instead of Eq. (5.72) and $N_{\rm eff}$ can be as low as 2.7 instead of 4. This greatly relieves the tension between eV sterile neutrinos and CMB data, which requires $N_{\rm eff}$ to be close to 3 up to high significance.

One can qualitative estimate the range of interaction parameters for which this mechanism can work by comparing the potential, the interaction rate, and the vacuum frequency f_{osc}. We show them in units of the Hubble rate in Fig. 5.3 as a function of the photon temperature for $G_X = 10^{10} G_F$. For simplicity we have assumed the neutrino temperature always to follow Eq. (5.72) when calculating V_{eff} and Γ_X (but not when determining H) so above the temperature relevant for e^+e^- annihilation they are underestimated. Nevertheless, as seen in the figure, the effective potential for that coupling is much larger than the oscillation frequency above 1 MeV and hence the conversion from active to sterile neutrinos will be strongly suppressed.

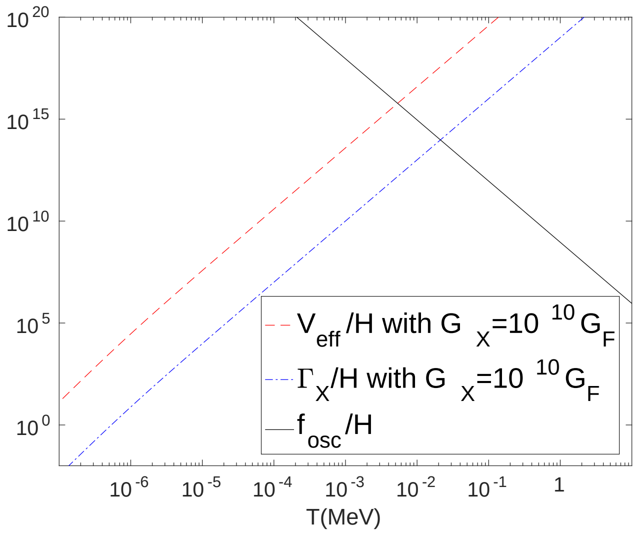

Figure 5.3: The effective in-medium potential, the scattering rate and vacuum oscillation frequency as a function of the temperature for $G_X = 10^{10} G_F$ and $g_X = 0.1$. We assume the light sterile neutrino mass $m_{\text{st}} = 1$ eV.

This qualitative estimate indicates that strong enough interaction can lead to the late production of sterile neutrinos and results in relatively low N_{eff}. With this motivation we now move to precisely quantify which range of interactions can lead to successful description of the bulk of cosmological data.

5.3.3 Determination of N_{eff}

The quantitative determination of N_{eff} in scenarios with light sterile neutrinos which are brought in to equilibrium by their mixing with the standard three active neutrinos requires to evaluate the time evolution of their energy density. To do so we can use the quantum kinetic equations (QKEs) of the 3+1 neutrino ensemble [182].

The starting point is the density matrix for the neutrinos

$$\varrho(p,\, t) = \begin{pmatrix} \varrho_{ee} & \varrho_{e\mu} & \varrho_{e\tau} & \varrho_{es} \\ \varrho_{\mu e} & \varrho_{\mu\mu} & \varrho_{\mu\tau} & \varrho_{\mu s} \\ \varrho_{\tau e} & \varrho_{\tau\mu} & \varrho_{\tau\tau} & \varrho_{\tau s} \\ \varrho_{se} & \varrho_{s\mu} & \varrho_{s\tau} & \varrho_{ss} \end{pmatrix}, \tag{5.122}$$

whose evolution is governed by the QKEs [183]

$$\mathrm{i}\,\frac{d\varrho}{dt} = [\Omega, \varrho] + C[\varrho]\,, \tag{5.123}$$

where $C[\varrho]$ represents the collision terms while the oscillation and in-medium potential terms corresponding to CC interactions with the background electrons and the NC interactions with the background neutrinos are

$$\begin{aligned} \Omega &= \frac{1}{2p} U^\dagger M^2 U + \sqrt{2} G_F \left[-\frac{8p}{3} \left(\frac{\mathcal{E}_l}{M_W^2} + \frac{\mathcal{E}_\nu}{M_Z^2} \right) \right] \\ &+ \sqrt{2} G_X \left[-\frac{8p}{3} \frac{\mathcal{E}_s}{M_X^2} \right] . \end{aligned} \tag{5.124}$$

$M^2 = \mathrm{diag}(0, \Delta m_{21}^2, \Delta m_{31}^2, m_{\mathrm{st}}^2)$ (we assume the sterile neutrino mass is much larger than the active ones), and M_W and M_Z are the masses of W and Z bosons respectively. U is the active-sterile vacuum mixing matrix constructed through

$$U = R_{34} R_{24} R_{23} R_{14} R_{13} R_{12}. \tag{5.125}$$

where R_{ij} represent a rotation of angle θ_{ij} in the ij plane. In what follows we fix the oscillation parameters between the three active neutrinos Δm_{21}^2, Δm_{31}^2, θ_{12} , θ_{13}, and θ_{23} to the best fit for normal ordering from the global oscillation analysis in NuFIT 3.0 [5, 6].

In Eq. (5.124) $\mathcal{E}_l = \mathrm{diag}(\varepsilon_e, 0, 0, 0)$, $\mathcal{E}_\nu$, and $\mathcal{E}_s = \mathrm{diag}(0, 0, 0, \varepsilon_s)$ are 4×4 matrices containing the energy density of the electrons, active neutrinos (which is in general non-diagonal with non-zero entries in the upper 3×3 sector), and sterile neutrinos respectively.

At this point it is more convenient to replace time, momentum and temperature by the variables:

$$x \equiv ma, \quad y \equiv pa, \quad z_\gamma \equiv T_\gamma a, \quad z_\nu \equiv T_\nu a, \tag{5.126}$$

where we take the arbitrary mass scale m to be 1 MeV. We stress that we have added z_ν to trace the difference between neutrino and photon temperatures at or after the time of e^+e^- annihilation. Also we normalize the scale factor to that $a(t) = 1/T_\nu$ so that $z_\nu(x)$ is always 1. We can solve for $z_\gamma(x)$ from the continuity equation (Eq. (5.15), see Eq. (15) in [184] for a detailed treatment). The solution doesn't depend on the details of the neutrino flavor evolution, so this $z_\gamma(x)$ is precomputed as a known function before solving the QKEs. With the new variables introduced above, we can rewrite Eq. (5.123) as

$$\begin{aligned} i\frac{d\varrho}{dx} = &+ \frac{x^2}{2m^2 y \widetilde{H}}\left[U^\dagger M^2 U, \varrho\right] + \frac{\sqrt{2}G_F m^2}{x^2 \widetilde{H}}\left[\left(-\frac{8ym^2}{3x^2M_W^2}\widetilde{\mathcal{E}}_l - \frac{8ym^2}{3x^2M_Z^2}\widetilde{\mathcal{E}}_\nu\right), \varrho\right] \\ &+ \frac{\sqrt{2}G_X m^2}{x^2 \widetilde{H}}\left[-\frac{8ym^2}{3x^2M_X^2}\widetilde{\mathcal{E}}_s, \varrho\right] + \frac{xC[\varrho]}{m\widetilde{H}}, \end{aligned} \tag{5.127}$$

where now $\varrho(x, y)$ is a function of x and y explicitly, and we define the normalized Hubble parameter as

$$\widetilde{H} \equiv \frac{x^2}{m}H = \frac{m}{M_{\text{Pl}}}\sqrt{\frac{8\pi\tilde{\varepsilon}(x, z_\gamma(x), z_\nu(x))}{3}}, \tag{5.128}$$

where M_{Pl} is the Planck mass and the comoving total energy density is defined as $\tilde{\varepsilon} \equiv \varepsilon(x/m)^4$ with ε as the total energy density. We are only interested in the radiation dominant era after muon decay, thus to a good approximation we can write the total energy density as

$$\tilde{\varepsilon}(x, z_\gamma(x), z_\nu(x)) = \tilde{\varepsilon}_\gamma + \tilde{\varepsilon}_e + \tilde{\varepsilon}_\nu, \tag{5.129}$$

$$\tilde{\varepsilon}_\gamma = \frac{\pi^2}{15}z_\gamma^4(x), \tag{5.130}$$

$$\tilde{\varepsilon}_e = \frac{2}{\pi^2}\int_0^\infty dy y^3 f_{\text{FD}}(y, z_\gamma(x)), \tag{5.131}$$

$$\tilde{\varepsilon}_\nu = \frac{1}{2\pi^2}\int_0^\infty dy y^3 \text{Tr}[\varrho(x, y) + \bar{\varrho}(x, y)]. \tag{5.132}$$

In what follows we assume the density matrix of antineutrinos is the same as neutrinos. The Fermi-Dirac distribution function in Eq. 5.131 is defined in Eq. (5.82) with the substitution $g_\nu \to g_e$.

Eq. (5.122), though clear, is extremely computationally demanding due to the momentum dependence of the density matrix, especially in the case of three active plus one sterile neutrino species. To retain the main features of the flavor evolution within a reasonable amount of computing time, we still resort to the average momentum approximation as described in [182]. In this approximation, we remove the momentum dependence in the equations by assuming

$$\varrho(x, y) \longrightarrow f_{\text{FD}}(y)\rho(x). \tag{5.133}$$

Note that $z_\nu(x)$ is a constant so $f_{\rm FD}$ is a function of y only. It is now straightforward to compute the momentum average of the variables by making use of the relation $\langle g(y)\rangle = \int_0^\infty y^2 g(y) f_{\rm FD}(y)dy / \int_0^\infty y^2 f_{\rm FD}(y)dy$ (one can immediately verify $\langle y\rangle = 3.15$ and $\langle 1/y\rangle = 0.456$). We can now write Eq. (5.127) in a compact form as

$$\begin{aligned} i\frac{d\rho}{dx} = &+ \frac{x^2}{2m^2\widetilde{H}}\langle\frac{1}{y}\rangle\left[U^\dagger M^2 U, \rho\right] + \frac{\sqrt{2}G_F m^2}{x^2\widetilde{H}}\left[\left(-\frac{8\langle y\rangle m^2}{3x^2M_W^2}\widetilde{\mathcal{E}}_l - \frac{8\langle y\rangle m^2}{3x^2M_Z^2}\widetilde{\mathcal{E}}_\nu\right), \rho\right] \\ &+ \frac{\sqrt{2}G_X m^2}{x^2\widetilde{H}}\left[-\frac{8\langle y\rangle m^2}{3x^2M_X^2}\widetilde{\mathcal{E}}_s, \rho\right] + \frac{x\langle C[\rho]\rangle}{m\widetilde{H}}\,, \end{aligned} \tag{5.134}$$

where in the potentials

$$\widetilde{\mathcal{E}}_l = \mathrm{diag}(\tilde{\varepsilon}_e, 0, 0, 0)\,, \tag{5.135}$$

$$\widetilde{\mathcal{E}}_\nu = \frac{2}{2\pi^2}\int_0^\infty dy y^3 G_s \varrho(x,y) G_s = \frac{7}{8}\frac{\pi^2}{15} G_s \rho(x) G_s\,, \tag{5.136}$$

$$\widetilde{\mathcal{E}}_s = \frac{2}{2\pi^2}\int_0^\infty dy y^3 G_{sX} \varrho(x,y) G_{sX} = \frac{7}{8}\frac{\pi^2}{15} G_{sX} \rho(x) G_{sX}\,. \tag{5.137}$$

In terms of the average momentum approximation, the diagonal entries in the density matrix denote the number density of active or sterile neutrinos normalized to the neutrino density in the standard cosmology, i.e. neutrino number densities follow standard Fermi-Dirac distribution with temperatures determined from Eq. (5.72) after e^+e^- annihilation. In the above equations $G_s = \mathrm{diag}(1,1,1,0)$ and $G_{sX} = \mathrm{diag}(0,0,0,1)$ contain the dimensionless coupling constants for active and sterile neutrinos, respectively. $\langle C[\varrho]\rangle$ is the momentum average of active and sterile collision terms expressed as [182, 185]

$$\begin{aligned} \langle C_\nu[\varrho]\rangle &= -\frac{i}{2}G_F^2\frac{m^5}{x^5}(\{S^2, \rho - I\} - 2S(\rho - I)S + \{A^2, \rho - I\} + 2A(\rho - I)A\,, \\ \langle C_s[\varrho]\rangle &= -\frac{i}{2}G_X^2\frac{m^5}{x^5}(\{S_X^2, \rho - I\} - 2S_X(\rho - I)S_X)\,, \end{aligned} \tag{5.138}$$

where the active neutrino scattering and annihilation matrix $S = \mathrm{diag}(g_s^e, g_s^\mu, g_s^\tau, 0)$ and $A = \mathrm{diag}(g_a^e, g_a^\mu, g_a^\tau, 0)$ with [185]

$$(g_s^e)^2 = 3.06, \quad (g_a^e)^2 = 0.50\,,$$
$$(g_s^{\mu,\tau})^2 = 2.22, \quad (g_a^{\mu,\tau})^2 = 0.28\,.$$

For sterile neutrinos $S_X = \mathrm{diag}(0,0,0,1)$. We always work in the approximation $T_\nu < M_X$ so the annihilation terms are neglected . Note that when using the average momentum approximation we lose the details of the phase-space distribution, so we always assume all neutrino species share the same temperature when solving the QKEs. This assumption is robust since even if there are small differences between the temperature of the different neutrino species, the in-medium potential are only corrected by factors of $\mathcal{O}(1)$ and the solution of the QKEs would be barely changed. We shall revisit this assumption later when we compute N_{eff}, where instead a small shift in neutrino temperature can make a big difference.

Our aim is to explore as large parameter space as possible but solving the QKEs is time demanding. So as a compromise, we allow the parameters to vary within the range $G_X = 10^{-2}G_F \sim 10^{10}G_F$ (from much smaller than weak coupling to much larger than weak coupling), $g_X = 10^{-3} \sim 10^{-1}$ (so we treat the gauge boson mass M_X as a parameter derived from G_X and g_X). As the benchmark values for the mixings we take $\sin^2\theta_{14} = 0.033$ and $\sin^2\theta_{24} = 0.012$ which are the best fit of the 3+1 scheme obtained with short baseline oscillation data [186]. We extend around those values by in the range $\sin^2\theta_{14} = 0.0033 \sim 0.33$ but fixing $\sin^2\theta_{14}/\sin^2\theta_{24}$ to 0.033/0.012. For simplicity we assume $\sin\theta_{34} = 0$ (no mixing between tau neutrinos and sterile neutrinos). We allow ${m_{\text{st}}}^2 = 0.01\ \text{eV}^2 \sim 10\ \text{eV}^2$ so that the allowed sterile neutrino mass can be as low as the 95% CL of the cosmological bounds on neutrino masses, and can be much larger than the mass suggested by short baseline anomalies.

As illustration of the output of the QKEs we show in Fig. 5.4 an example of the neutrino flavor evolution with parameters such that the new interaction is much stronger than electroweak interactions. As one would expect, sterile neutrinos are produced only when the temperature is well below 1 MeV and all four neutrino species get to similar (though not the exactly the same) number densities after thermalization. For comparison we show in the right panel the standard neutrino flavor evolution in the absence of new interactions. In this case sterile neutrinos get immediately thermalized with the active neutrinos. It clearly shows that the gauge boson interaction, when strong enough, is capable of postponing the production of sterile neutrinos until after active neutrino decoupling.

Now that we have the solutions of the QKEs, the next step is to obtain N_{eff} from the solutions. It is, however, not a straightforward task. Naively we would expect $N_{\text{eff}} = \rho_{ee}+\rho_{\mu\mu}+\rho_{\tau\tau}+\rho_{ss}$ where ρ_{ee}, $\rho_{\mu\mu}$, $\rho_{\tau\tau}$ and ρ_{ss} are the normalized number density of four neutrino species. But this method fails when neutrino thermalization takes place after active neutrino decoupling. This is so because the total entropy and number in the neutrino sector is conserved after decoupling, so the total normalized neutrino number density will always be close to 3. But it does not mean $N_{\text{eff}} = 3$ because the entropy initially

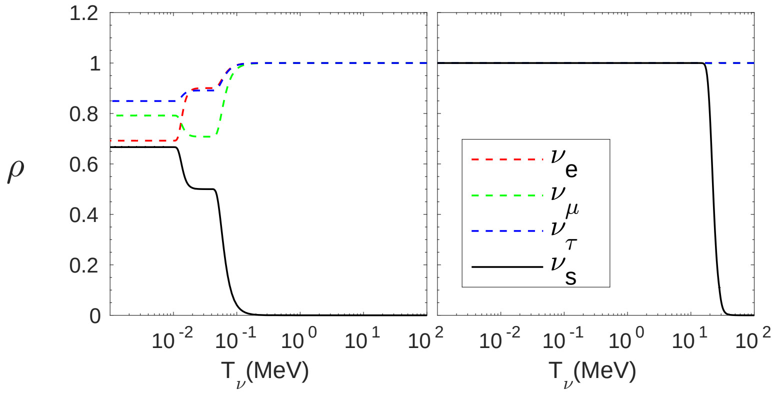

Figure 5.4: The number density $\rho_{\alpha\alpha}$ of active and sterile neutrino species as a function of the neutrino temperature. The left panel shows the flavor evolution for $G_X = 10^{10} G_F$, $g_X = 0.1$, $m_{\rm st} = 1$ eV and $\sin\theta_{14} = 0.1$. The right panel corresponds to standard 4ν evolution without any new interactions.

shared by the three active neutrino species is later shared by sterile neutrinos as well through thermalization, which leads to a reduction in the total neutrino energy density. To obtain a reasonable $N_{\rm eff}$ we make the following assumptions:
1) Active neutrinos have decoupled completely from the plasma at 1 MeV. At that time e^+e^- annihilation has not taken place yet, so in the standard cosmology neutrinos still have the same temperature as the plasma at 1 MeV.
2) All neutrino species keep Fermi-Dirac distribution during flavor evolution and their phase-space distribution is only characterized by their temperatures.

At this point it is important to differentiate the temperature of different neutrino species since this is relevant for the determination of $N_{\rm eff}$. We argue that neutrinos are able to maintain Fermi-Dirac shape as long as collision is efficient enough to bring neutrinos to equilibrium. This happens when the new interaction is strong enough to keep neutrinos self-coupled, and when the new interaction is so weak that thermalization occurs before decoupling at which time electroweak interaction is still efficient. For the interaction strength in between, the behaviour of the physical system is expected to be continuous. We find that keeping the Fermi-Dirac shape approximation leads to solutions which interpolate well between the two limiting regimes of $N_{\rm eff}$. So we feel confident that we are still capturing the main dependence of the results with the model parameters.

Following the hypotheses above, we compute the temperatures of electron neutrinos and other neutrino species as referred to the temperature of ν_e in standard cosmology. The evolution of temperature is determined by entropy conservation after 1 MeV and N_{eff} is calculated based on the neutrino temperatures. We can do this step by step. First we have

$$\rho_{ee,\mathrm{dec}} = \frac{n_{\nu_e,\mathrm{dec}}}{n^*_{\nu,\mathrm{dec}}} = \left(\frac{T_{\nu_e,\mathrm{dec}}}{T^*_{\nu,\mathrm{dec}}}\right)^3 , \tag{5.139}$$

where where "dec" stands for the complete decoupling at 1 MeV and n^*_ν and T^*_ν are the neutrino number density (for one neutrino species) and temperature in the standard 3ν mixing case. This is the definition of ρ_{ee} which is the number density of electron neutrinos normalized to that of a standard neutrino species. Since we assume Fermi-Dirac distributions the number density $n_\nu \propto T^3_\nu$. From this we can solve for the temperature of electron neutrinos as referred to the standard active neutrinos at decoupling. After that it is straightforward to calculate the temperatures of other neutrino species with respect to this temperature by comparing their number densities, i.e.

$$\frac{\rho_{\alpha\alpha,\mathrm{dec}}}{\rho_{ee,\mathrm{dec}}} = \left(\frac{T_{\nu_\alpha,\mathrm{dec}}}{T_{\nu_e,\mathrm{dec}}}\right)^3 . \tag{5.140}$$

After decoupling the total entropy in the neutrino sector is conserved. In the presence of sterile neutrinos and new interactions, the entropy

$$S \propto \sum_\alpha T^3_{\nu_\alpha,\mathrm{dec}} a^3_{\mathrm{dec}} = \sum_\alpha T^3_{\nu_\alpha,\mathrm{th}} a^3_{\mathrm{th}} , \tag{5.141}$$

where "th" means some time later when the thermalization process stops, i.e. the normalized number density doesn't change anymore. Or in the standard cosmology

$$T^*_{\nu,\mathrm{dec}} a_{\mathrm{dec}} = T^*_{\nu,\mathrm{th}} a_{\mathrm{th}} . \tag{5.142}$$

Considering Eq. (5.140) we can rewrite Eq. (5.141) as

$$\frac{\sum_\alpha \rho_{\alpha\alpha,\mathrm{dec}}}{\rho_{ee,\mathrm{dec}}} T^3_{\nu_e,\mathrm{dec}} a^3_{\mathrm{dec}} = \frac{\sum_\alpha \rho_{\alpha\alpha,\mathrm{th}}}{\rho_{ee,\mathrm{th}}} T^3_{\nu_e,\mathrm{th}} a^3_{\mathrm{th}} . \tag{5.143}$$

Eqs. (5.143) and (5.142) allow us to determine the electron neutrino temperature in terms of standard neutrino species after thermalization. Again using Eq. (5.140) we can infer the temperature of other neutrino species in terms of the temperature of electron neutrinos, i.e.

$$\frac{\rho_{\alpha\alpha,\mathrm{th}}}{\rho_{ee,\mathrm{th}}} = \left(\frac{T_{\nu_\alpha,\mathrm{th}}}{T_{\nu_e,\mathrm{th}}}\right)^3 . \tag{5.144}$$

Once we have all the neutrino temperatures, we can calculate N_{eff} after thermalization by comparing with the temperature of standard neutrino species where

$$N_{\mathrm{eff}} = \sum_\alpha \left(\frac{T_{\nu_\alpha,\mathrm{th}}}{T^*_{\nu,\mathrm{th}}}\right)^4 . \tag{5.145}$$

Finally when switching to mass eigenstates we estimate the neutrino number densities by $n_{\nu_i} = \sum_\alpha |U_{\alpha i}|^2 n_{\nu_\alpha}$ where as before i denotes mass eigenstates and α denotes flavor eigenstates. We still assume Ferimi-Dirac distribution for mass eigenstates.

We show in Fig. 5.5 N_{eff} as a function of G_X. For very small G_X early thermalization leads to $N_{\mathrm{eff}} \simeq 4$ and for very large G_X late thermalization leads to $N_{\mathrm{eff}} \simeq 2.7$. The range of G_X where the transition from 4 to 2.7 takes place depends on the choice of g_X for fixed sterile neutrino mass and mixing.

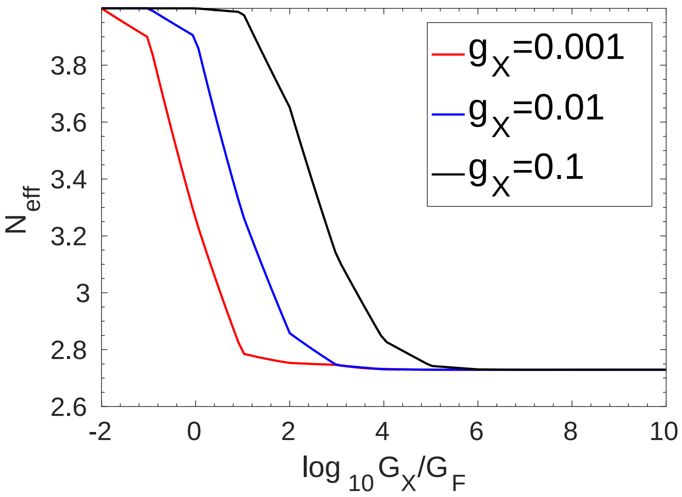

Figure 5.5: N_{eff} as a function of effective coupling G_X. The red, blue and black curves correspond to g_X =0.001, 0.01, 0.1, respectively. Other parameters are fixed to $m_{\mathrm{st}} = 1$ eV and $\sin\theta_{14} = 0.1$.

Besides its effect on N_{eff}, the new interactions can also possibly help to avoid the cosmological constraints on the total neutrino mass. Sterile neutrinos may suppress the growth of matter perturbation because of their free-streaming till they become non-relativistic. However, if sterile neutrinos remain tightly coupled before non-relativistic transition, this constraint is not valid anymore. We see from Fig. 5.3 that the ratio Γ_X/H is still larger than 1 at 1 eV, which again justifies our choice of parameter range $G_X = 10^{-2}G_F \sim 10^{10}G_F$.

5.3.4 Effects on Perturbations

Next we would like to see quantitatively how the new interactions can affect the predictions of CMB and large scale structure (LSS) data. New interactions add collision terms to the right of the Boltzmann equation (5.86) and make it quite complicated. However, it has been shown in Ref. [187] that an exact description of neutrino interactions is quantitatively equivalent to the relaxation time approximation [188] where the collision term can be approximated by [189, 190]

$$\frac{1}{f_0}\frac{\partial f}{\partial \tau} = -\frac{\mathcal{N}}{\tau_\nu}\,, \tag{5.146}$$

where $\tau_\nu = (n_{\nu_s}\langle\sigma v\rangle)^{-1}$ is the mean conformal time between collisions. Since $\langle\sigma v\rangle \simeq G_X^2 T_{\nu_s}^2$, we have

$$\tau_\nu^{-1} = \frac{3}{2}\frac{\zeta(3)}{\pi^2}G_X^2 T_{\nu_s}^5\,, \tag{5.147}$$

where T_{ν_s} is obtained from the solution of QKEs. In terms of mass basis, Eq. (5.86) can be written as

$$\frac{\partial \mathcal{N}_i}{\partial \tau} + i\frac{q}{\epsilon}(\boldsymbol{k}\cdot\hat{\mathbf{n}})\mathcal{N}_i + \frac{d\ln f_0}{d\ln q}\left[\Phi_i' - i\frac{\epsilon}{q}(\boldsymbol{k}\cdot\hat{\mathbf{n}})\Psi_i\right] = -\Gamma_{ij}\mathcal{N}_j,. \tag{5.148}$$

where $i = 1, 4$ denote the mass eigenstates and Γ_{ij} is defined in mass basis as

$$\begin{aligned}\Gamma_{ij}/\tau_\nu^{-1} &= U\,\mathrm{diag}(0,0,0,1)U^\dagger \\ &= \begin{bmatrix} \sin^2\theta_{14} & \frac{1}{2}\sin 2\theta_{14}\sin\theta_{24} & 0 & \frac{1}{2}\sin 2\theta_{14}\cos\theta_{24} \\ \frac{1}{2}\sin 2\theta_{14}\sin\theta_{24} & \cos^2\theta_{14}\sin^2\theta_{24} & 0 & \frac{1}{2}\cos^2\theta_{14}\sin 2\theta_{24} \\ 0 & 0 & 0 & 0 \\ \frac{1}{2}\sin 2\theta_{14}\cos\theta_{24} & \frac{1}{2}\cos^2\theta_{14}\sin 2\theta_{24} & 0 & \cos^2\theta_{14}\cos^2\theta_{24} \end{bmatrix}\end{aligned} \tag{5.149}$$

It is straightforward to expand $\mathcal{N}$ as in Eq. (5.101) and obtain the new Boltzmann equation

$$\mathcal{N}'_{i,0} = -\frac{qk}{\epsilon}\mathcal{N}_{i,1} - \Phi'\frac{d\ln f_{i,0}}{d\ln q}\,, \tag{5.150}$$

$$\mathcal{N}'_{i,1} = \frac{qk}{3\epsilon}(\mathcal{N}_{i,0} - 2\psi_{i,2}) - \frac{\epsilon k}{3q}\Psi\frac{d\ln f_{i,0}}{d\ln q}\,, \tag{5.151}$$

$$\mathcal{N}'_{i,l} = \frac{qk}{(2l+1)\epsilon}[l\psi_{i,(l-1)} - (l+1)\mathcal{N}_{i,(l+1)}] - \Gamma_{ij}\mathcal{N}_{j,l}\,, \quad l \geq 2\,. \tag{5.152}$$

As in Ref. [190] we have set the collision terms to zero in the equations of monopole and dipole to ensure particle number and momentum conservation. In case $\Gamma_{ij} > \mathcal{H}$, the quadrupole (related to the anisotropic σ_ν) and higher multipoles are suppressed. So contrary to our discussion of free-streaming neutrinos in radiation era in the previous section, in the presence of the interactions the power in higher multipoles are now transferred to the density and velocity fluctuations which in turn contribute to the total gravitational source and enhance the amplitude of the CMB fluctuations that entered the horizon before recombination. This enhancement is clearly seen in Fig. 5.6, when we compare the red line ($G_X = 10^7 G_F$) with the dashed red line ($G_X = 10^{10} G_F$). To obtain these predictions we have solved the new collisional Boltzmann equation in a modified version of the Boltzmann code CLASS [191] [1].

It is no surprise that the first peak of the red lines are all lower than that of ΛCDM best fit. This is because for the interactions considered the resulting N_{eff} is always smaller than 3 and N_{eff} smaller than 3 tends to reduce the energy density of radiation and bring ahead the matter-domination equality, and hence reduce the amplitude of the peaks. The expansion history is also changed because of this reduction. As we can see the peaks are shifted to the left. In addition, notice that we have defined N_{eff} when neutrinos are all relativistic, so for CMB observables the contribution of the sterile neutrino is further reduced a little because they become partially non-relativistic during recombination. The solid blue line ($G_X = 10^{-2} G_F$), on the other hand, shows the opposite behaviour since for these weak interactions the resulting N_{eff} is larger than 3. Indeed, as a cross check, we have verified explicitly that the blue line can exactly mimic the behavior of a sterile species without interactions. The new interaction in this case is too weak to be significant in the thermalization of sterile neutrinos.

To examine the effects of new interactions on the growth of large scale

---

[1] Note that Eqs. (5.150)-(5.152) are written in Newtonian gauge. It is transformed into Synchronous gauge in the code (see Ref. [163] for a detailed description of gauges and gauge transformations in cosmology).

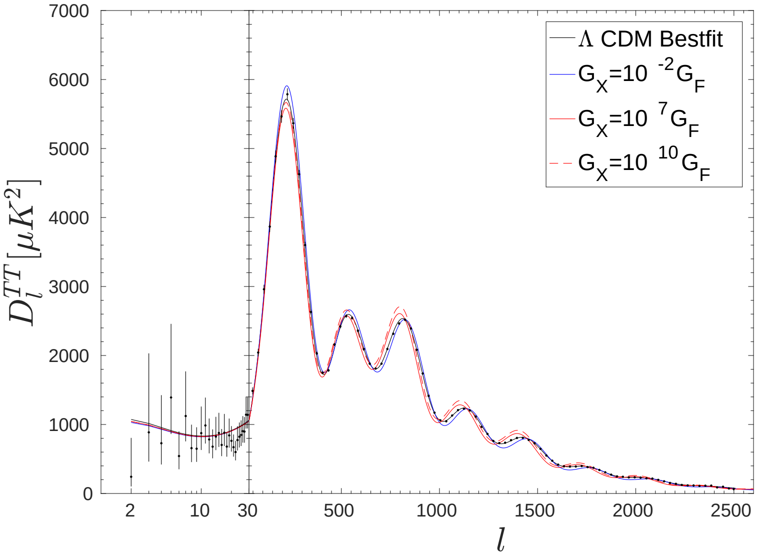

Figure 5.6: CMB temperature power spectrum. The predicted spectrum in ΛCDM for the best fit of Planck TT+lowP [4] ($\omega_b = 0.0222$, $\omega_{\rm cdm} = 0.1197$, $100\theta_{\rm MC} = 1.0485$, $\tau_{\rm reio} = 0.078$, $\ln 10^{10} A_s = 3.089$, and $n_s = 0.9655$) is shown in black along with error bars from Planck 2015 data. Colored lines correspond to ΛCDM models with one sterile neutrino species and new interactions. Cosmological parameters are the same as the best fit of Planck TT+lowP and the implicit parameters for new interactions are the same as Fig. 5.4 ($g_X = 0.1$, $m_{\rm st} = 1$ eV, and $\sin\theta_{14} = 0.1$). The solid blue, solid red and dashed red lines show different interaction strength corresponding to $G_X = 10^{-2} G_F\,(N_{\rm eff} = 4)$, $G_X = 10^{7} G_F\,(N_{\rm eff} = 2.7)$, $G_X = 10^{10} G_F\,(N_{\rm eff} = 2.7)$, respectively.

structures we also show the corresponding matter power spectrum in Fig. 5.7. As discussed, a $\mathcal{O}$(eV) sterile neutrino will greatly suppress the matter power spectrum at small scales, as we can see from the blue curve. However, adding the new ν_s interactions is able to make neutrinos less free streaming and bring the red curves close to ΛCDM best fit.

5.4 Confronting with Cosmological Data

In the previous section we have solved the QKEs to study the flavor transitions in the early universe. It provides a powerful tool to explore the role of sterile neutrinos in the expansion history of the universe in the presence of new sterile neutrinos with additional interactions. Furthermore to quantify

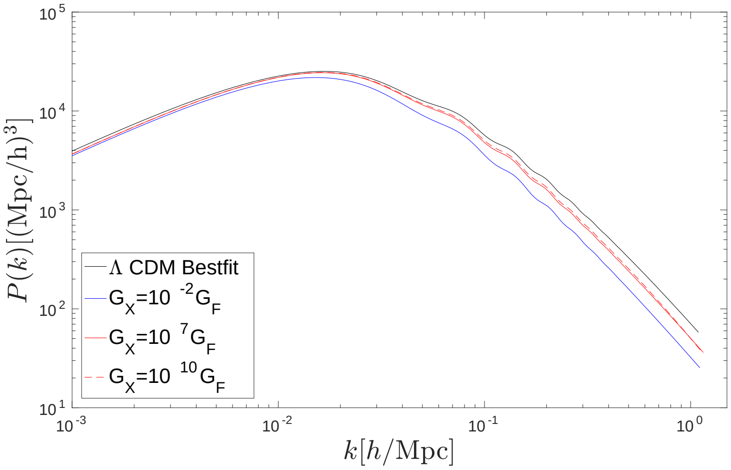

Figure 5.7: Matter power spectrum as a function of k. The models and parameters are the same as Fig. 5.6.

the effects of the sterile interactions in the evolution of the perturbations we have modified the neutrino Boltzmann equation in Sec. 5.3.4 and show the corresponding CMB and matter power spectrum.

Now we are going to confront these modifications with data. First in Sec. 5.4.1 we show the constraints on sterile neutrino mass and new interaction strength from their effects on BBN. After that we confront the new ν_s interaction model with CMB and LSS measurements and present the results in Sec. 5.4.2.

5.4.1 Constraints from Big Bang Nucleosynthesis

We have seen from Eq. (5.79) that both N_{eff} and the number density of electron neutrinos can affect the abundances of BBN nuclei. In terms of our solution of QKEs, the normalized electron neutrino number density $\bar{n}_{\nu_e} = \rho_{ee}$. The effect of ν_e number density can be incorporated to a redefinition of g_* and ΔN_{eff}, say

$$\frac{\sqrt{g_*}}{(1+\bar{n}_{\nu_e})/2} = \frac{\sqrt{g'_*}}{(1+1)/2}\,, \tag{5.153}$$

where $g'_* \equiv 10.75 + \Delta N'_{\mathrm{eff}}$, i.e. we start with a standard neutrino number density, but modify ΔN_{eff} to get the correct neutron freezing-out temperature. It is straightforward to see the modified ΔN_{eff} to be

$$\Delta N'_{\mathrm{eff}} = \frac{4}{7}\left[\frac{43+7\Delta N_{\mathrm{eff}}}{(1+\bar{n}_{\nu_e})^2} - 10.75\right]\,. \tag{5.154}$$

This treatment is similar to that of Dolgov *et al.* [192]. Since $N_{\rm eff}$ and $\bar{n}_{\nu_e}$ are rather insensitive to the small change in T_f, while the neutron-to-proton depends on T_f exponentially, we use the $N_{\rm eff}$ and $\bar{n}_{\nu_e}$ at 1 MeV to determine the ratio n_n/n_p. The most abundant nuclei heavier than hydrogen are ^{4}He and deuterium. Their abundances have been determined by observations to bew[193]

$$Y_{\rm P} \equiv 4\frac{n_{\rm He}}{n_b} = 0.2465 \pm 0.0097\,, \tag{5.155}$$

and [194]

$$y_{\rm DP} \equiv 10^5\frac{n_{\rm D}}{n_{\rm H}} = 2.53 \pm 0.04\,, \tag{5.156}$$

where n_b, $n_{\rm He}$, $n_{\rm D}$, $n_{\rm H}$ are the number density of baryons and helium, deuterium and hydrogen nuclei respectively. To confront the predictions in the presence of new ν_s interactions with Big Bang Nucleosynthesis (BBN) data, we use the helium and deuterium abundances given by Taylor expansions obtained with the PArthENoPE code [195], i.e.

$$\begin{aligned}
Y_{\rm P} &= 0.2311 + 0.9502\omega_b - 11.27\omega_b^2 \\
&+ \Delta N'_{\rm eff}(0.01356 + 0.008581\omega_b - 0.1810\omega_b^2) \\
&+ \Delta N'^2_{\rm eff}(-0.0009795 - 0.001370\omega_b + 0.01746\omega_b^2)\,, \qquad (5.157)\\
y_{\rm DP} &= 18.754 - 1534.4\omega_b + 48656\omega_b^2 - 552670\omega_b^3 \\
&+ \Delta N'_{\rm eff}(2.4914 - 208.11\omega_b + 6760.9\omega_b^2 - 78007\omega_b^3) \\
&+ \Delta N'^2_{\rm eff}(0.012907 - 1.3653\omega_b + 37.388\omega_b^2 - 267.78\omega_b^3)\,, \qquad (5.158)
\end{aligned}$$

where ω_b is the energy density of baryons today defined as $\omega_b \equiv \Omega_b h^2$ and $h \equiv H_0/(100{\rm kms^{-1}Mpc^{-1}})$. The treatment is similar to that of Planck Collaboration [4]. The theoretical predictions are subject to errors from neutron lifetime and the interaction rate of d(p,γ)^{3}He. They are predicted to be $\sigma^{\rm th}(Y_{\rm P}) = 0.0003$ and $\sigma^{\rm th}(y_{\rm DP}) = 0.06$. Since theoretical errors are not correlated with the errors from observations, we can add them in quadrature.

We perform a Bayesian inference with MultiNest [53–55]. The likelihood function is constructed by

$$-2\ln\mathcal{L}(\boldsymbol{\omega}) = \frac{(Y_{\rm P}(\boldsymbol{\omega}) - Y_{\rm P}^{\rm dat})^2}{(\sigma^{\rm dat}_{Y_{\rm P}})^2 + (\sigma^{\rm th}_{Y_{\rm P}})^2} + \frac{(Y_{\rm P}(\boldsymbol{\omega}) - y_{\rm DP}^{\rm dat})^2}{(\sigma^{\rm dat}_{y_{\rm DP}})^2 + (\sigma^{\rm th}_{y_{\rm DP}})^2}\,, \tag{5.159}$$

where the parameters $\boldsymbol{\omega} = (G_X, g_X, \omega_b, m_{\rm st}, \theta_{14})$. We assume flat priors on these parameters within the range

$$\begin{array}{ll} -2 \leq \log_{10}(G_X/G_F) \leq 10 \ , & 0.001 \leq g_X \leq 0.1 \ , \\ 0.93 \text{ eV} \leq m_{\text{st}} \leq 1.43 \text{ eV} \ , & 0.012 \leq \sin^2\theta_{14} \leq 0.05 \ , \\ 0.02153 \leq \omega_b \leq 0.02291 \ , & \end{array} \tag{5.160}$$

where the prior on ω_b is the 3σ range as obtained from [4] and the 3σ ranges of m_{st} and $\sin^2\theta_{14}$ come from the fit of short baseline anomalies [196]. The posteriors of G_X and g_X are shown in Fig. 5.8. As expected very small G_X is disfavored since it yields N_{eff} close to 4. The posterior distribution of g_X is almost flat meaning this parameter is very mildly constrained by BBN data. Indeed, the marginalized posteriors of the parameters are $g_X \leq 0.064\,(1\sigma)$ and $\log_{10}(G_X/G_F) \geq 5.9\,(1\sigma)$ and $\log_{10}(G_X/G_F) \geq 3.8\,(2\sigma)$. All values of g_X is allowed in the 2σ range.

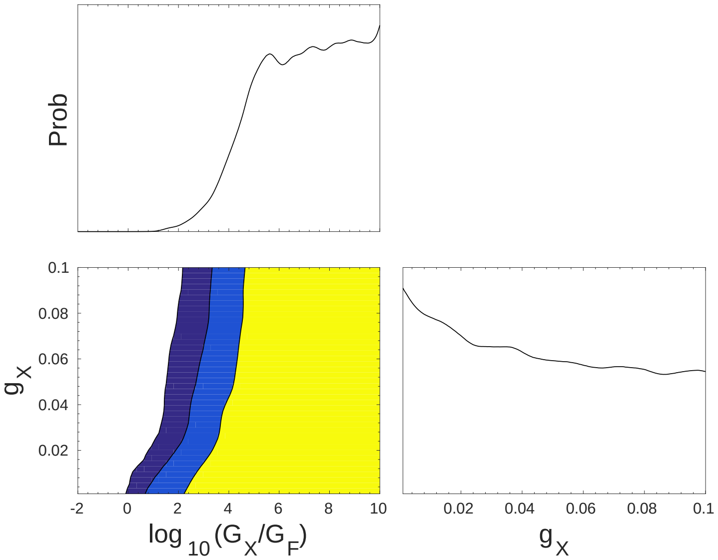

Figure 5.8: Posteriors of $\log_{10}(G_X/G_F)$ and g_X. The yellow, blue and dark blue regions correspond to the 2σ, 3σ and 4σ allowed ranges, respectively.

5.4.2 Global Analysis of Cosmological Data

We perform a Bayesian analysis of the CMB and LLS data to test the new interaction model by interfacing CLASS with the Markov Chain Monte Carlo (MCMC) code Monte Python [197]. The cosmological parameters are the same as the base ΛCDM model in Ref. [4], i.e. the baryon energy density ω_b, the cold dark matter density $\omega_{\text{cdm}} \equiv \Omega_{\text{cdm}} h^2$, the size of sound horizon at recombination

$100\theta_{\rm MC}$, the optical depth to reionisation $\tau_{\rm reio}$ and the amplitude and tilt of the initial power spectrum $\ln(10^{10}A_s)$ and n_s respectively. All cosmological parameters have flat priors without upper nor lower limits except $\tau_{\rm reio} \geq 0.04$. Besides the six cosmological parameters, we have four more parameters to describe the new scenario: $\log_{10}(G_X/G_F)$, g_X, $m_{\rm st}$ and $\sin^2\theta_{14}$. Their prior ranges for them can be found in Table 5.1.

Prior	$\log_{10}(G_X/G_F)$	g_X	$m_{\rm st}$(eV)	$\sin^2\theta_{14}$
Broad	$[-2,\ 10]$	$[0.001,\ 0.064]$	$[0.1,\ 3]$	$[0.0033\,, 0.33]$
Narrow	$[-2,\ 10]$	$[0.001,\ 0.064]$	1.27 ± 0.03	0.028 ± 0.006

Table 5.1: Prior ranges for "broad prior" and "narrow prior". All the parameters are flat except $m_{\rm st}$ and $\sin^2\theta_{14}$ for narrow prior which are instead gausian with the center and width listed above.

Note that the prior of the parameter g_X is flat in the limited range $[0.001,\ 0.064]$. It is motivated by the 1σ range of BBN constraint discussed in the previous section. The upper limit is put to avoid an over large parameter space for the nearly unconstrained parameter or otherwise the MCMC chains would not be converged. g_X only enters the Boltzmann code through $N_{\rm eff}$, where it degenerates with other three new interaction parameters. As we can see from the analysis of BBN data, simply fitting $N_{\rm eff}$ can not put tight constraints on g_X. So we argue our limit on g_X is consistent with BBN data but without loss of generality. We impose two different kind of priors on $m_{\rm st}$ and $\sin^2\theta_{14}$. One is flat in the range 0.1 eV $\leq m_{\rm st} \leq$ 3 eV and $0.0033 \leq \sin^2\theta_{14} \leq 0.33$, which we denote as "broad prior" . They are as large as the range where we have solved the QKEs. The other one is gaussian with $m_{\rm st} = 1.27 \pm 0.03$ eV and $\sin^2\theta_{14} = 0.028 \pm 0.006$. They are motivated by the best fit and width as obtained from the analysis of short baseline anomalies [196]. We denote it as "narrow prior". Technically, the narrow prior is imposed by adding a gaussian likelihood to the data likelihood. To interface the QKEs with the modified CLASS code for the neutrino Boltzmann equations, we first solve the QKEs in the parameter ranges listed above and then interpolate the solutions to obtain $N_{\rm eff}$ and neutrino temperatures to be input in CLASS. The resulting priors of $N_{\rm eff}$ corresponding to the two priors for the relevant parameters is illustrated in Fig. 5.9. As $N_{\rm eff}$ mainly depends on the effective coupling G_X, if $G_X \gg G_F$, $N_{\rm eff} \simeq 2.7$; on the other hand, if $G_X \ll G_F$, $N_{\rm eff} \simeq 4$. Therefore the resultant $N_{\rm eff}$ of both broad and narrow priors are peaked at these two extremes and it differs from those extreme values in a very small range of the input parameter space. In the figure we also include a modified prior which is nearly flat in $N_{\rm eff}$ that we will describe at the end of this section.

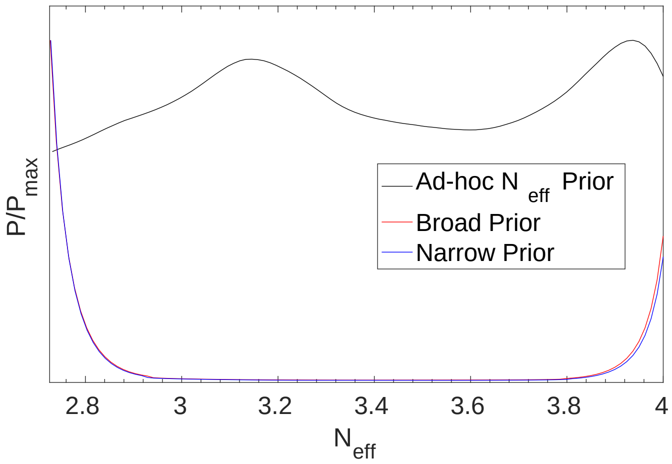

Figure 5.9: Resulting priors on $N_{\rm eff}$ for broad prior (red line) and narrow prior (blue line). For comparison we also cut the parameter space of M_X to force a nearly flat prior on $N_{\rm eff}$. See text for details.

For CMB we use the Planck 2015 [198] high multipole temperature correlation data as well as the low multipole polarization data (denoted as “Planck TT+lowP” in the Planck papers, and we use “TT” here for short). For the LSS data we include the measurements of the scale of the Baryon Acoustic Oscillation peak (BAO) at different red shifts as measured in the 6dF Galaxy Survey [199], the SDSS DR7 main Galaxy samples [200], the CMASS [201] and LOWZ [202] samples from SDSS DR11 results of BOSS experiment. The full information of the matter power spectrum is helpful in understanding the role of new interactions in structure formation, though, we do not use this data since it is subject to galaxy bias and other non-linear effects which are not well modeled within our assumptions.

We have summarized our results in Table 5.2 and Fig. 5.10 where we give the allowed ranges of the 6+4 parameters in the analysis and the posterior probability distribution for the four new parameters respectively. As expected there is nearly no constraint on g_X and $\sin^2\theta_{14}$. The 95% CL limit on $m_{\rm st}$ for broad prior and TT data is $m_{\rm st} < 0.91$ eV. It can be compared with the 95% limit of $m_{\rm st} < 0.82$ eV in terms of the SΛCDM model in Ref. [190]. There is no wonder that our limit is a little relaxed since we work in a larger range of G_X. But it shows that even with new interactions a sterile mass larger than 1 eV is still excluded by more than 2σ. Adding BAO data puts even tighter constraint on $m_{\rm st}$ and we find $m_{\rm st} < 0.37$ eV at 95% CL.

We also notice that the interacting ν_s scenario with large G_X ($G_X >$

	Broad Prior		Narrow Prior	
Parameter	TT	TT+BAO	TT	TT+BAO
ω_b	$0.02192^{+0.00021}_{-0.00033}$	0.02248 ± 0.00033	$0.02192^{+0.00023}_{-0.00031}$	$0.02301^{+0.00037}_{-0.00043}$
$\omega_{\rm cdm}$	$0.1179^{+0.0019}_{-0.0036}$	$0.1190^{+0.0047}_{-0.0081}$	$0.1172^{+0.0021}_{-0.0036}$	0.1145 ± 0.0061
$100\theta_{\rm MC}$	$1.04218^{+0.00065}_{-0.00046}$	$1.04189^{+0.0010}_{-0.00080}$	1.04226 ± 0.00061	$1.04218^{+0.00083}_{-0.00074}$
$\ln 10^{10} A_s$	$3.077^{+0.032}_{-0.045}$	$3.125^{+0.045}_{-0.052}$	$3.078^{+0.035}_{-0.045}$	3.184 ± 0.056
n_s	$0.9509^{+0.0067}_{-0.013}$	$0.977^{+0.010}_{-0.019}$	$0.9388^{+0.0079}_{-0.013}$	0.985 ± 0.021
$\tau_{\rm reio}$	$0.075^{+0.016}_{-0.021}$	0.097 ± 0.021	$0.076^{+0.017}_{-0.021}$	0.130 ± 0.024
$\log_{10}(G_X/G_F)$	$[0.41, 8.37]$	$[-1.36, 7.56]$	> 1.42	$[-1.90, 2.31]$
g_X	-	-	-	< 0.054
$m_{\rm st}/{\rm eV}$	< 0.91	< 0.37	1.27 ± 0.03	1.26 ± 0.03
$\sin^2\theta_{14}$	-	-	0.028 ± 0.006	0.027 ± 0.006
H_0	$63.3^{+1.5}_{-2.3}$	$68.5^{+1.6}_{-3.1}$	$60.26^{+0.81}_{-1.8}$	67.6 ± 2.5

Table 5.2: Allowed ranges for the model parameters for different priors and data sets. Cosmological parameters are shown in mean$\pm 1\sigma$ and the parameters for new interactions are shown in 95% CL except for $m_{\rm st}$ and $\sin^2\theta_{14}$ in narrow priors. We also show the corresponding derived ranges for H_0 in unit of kms^{-1}Mpc^{-1}.

$10^4 G_F$) is preferred over the non-interacting scenario when considering TT data only. This is expected since small G_X tends to produce $N_{\rm eff} \simeq 4$ which is too far away from the favoured value of 3 to be reconciled with the shift of other cosmological parameters. What is surprising is that by adding BAO data, the favouring of large G_X drops significantly while that of small G_X is lifted considerably. Indeed in the case of narrow prior, the non-interacting scenario is even more favored than the strongly interacting case. This change is also reflected in the posterior of $N_{\rm eff}$. Remember that the priors of $N_{\rm eff}$ are peaked both at 2.7 and 4 (see Fig. 5.9) but the peak of around 4 is lower. However, as seen in Fig. 5.10, the inclusion of BAO information to the TT data raises the peak of around $N_{\rm eff} = 4$ and for the case of the narrow prior it totally disfavours $N_{\rm eff} = 2.7$.

To better understand this behavour we plot the predicted values of the BAO observable as a function of redshift $z = a_0/a - 1$ in Fig. 5.11. The plotted function $D_V(z)$ is defined as the combination of the angular diameter

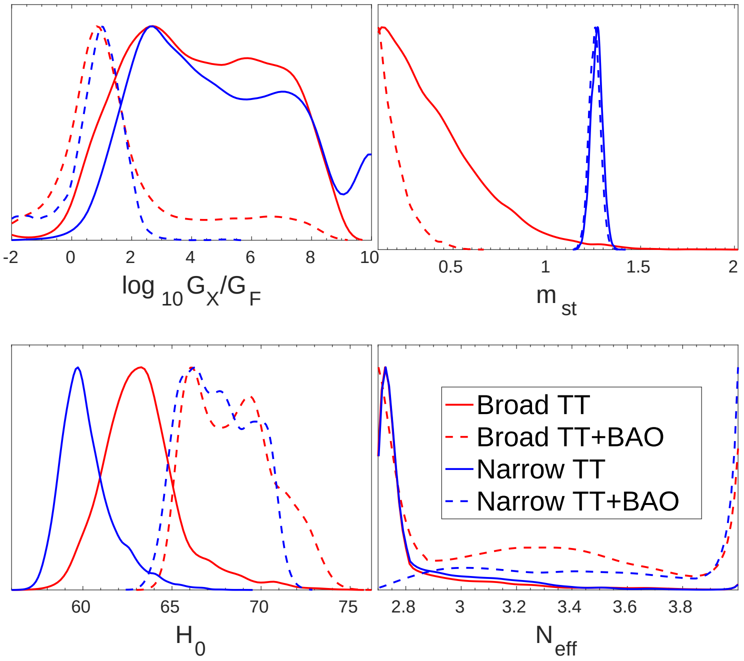

Figure 5.10: Posterior distribution of relevant cosmological and new interaction parameters. The solid red, dashed red, solid blue and dashed blue lines correspond to full prior with Planck data, full prior with Planck+BAO data, narrow prior with Planck data and narrow prior with Planck+BAO data, respectively. They are normalized so that the maximum probability is 1.

distance $D_A(z)$ and Hubble parameter $H(z)$, i.e.

$$D_V(z) = \left[(1+z)^2 D_A^2(z) \frac{cz}{H(z)}\right]^{1/3}, \tag{5.161}$$

where the angular diameter distance is defined, for an astrophysical object with physical size d and angular size θ as

$$D_A = \frac{d}{\theta}\,. \tag{5.162}$$

r_s is the comoving sound horizon at the end of the baryon drag epoch (roughly the time when baryons decoupled from photons). The ratio is quite robust and unaffected by uncertainties in the modeling of non-linear structure formation and other systematics. It is clear that both D_V and r_s are affected by the expansion history of the universe and hence depend on H_0. Let us stress that

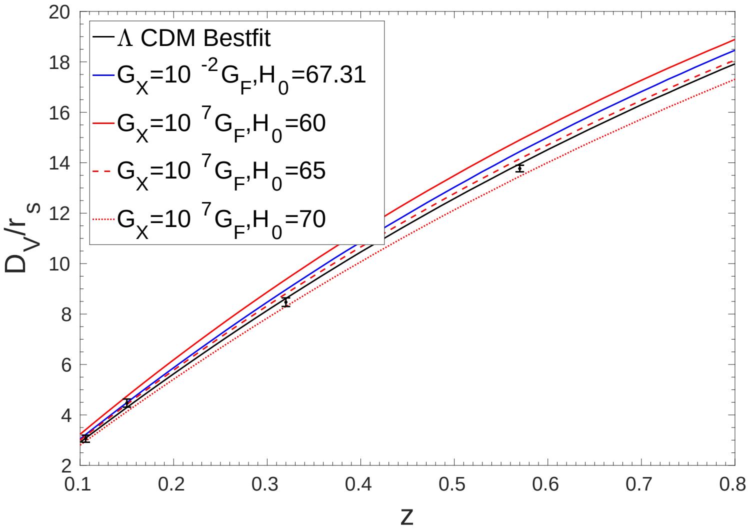

Figure 5.11: D_V/r_s as a function of redshift z. BAO data and error bars are shown in black. The parameters for the solid black (ΛCDM) are the same as Fig. 5.6 so for this curve $H_0 = 67.31$. The colored lines correspond to the interacting ν_s scenario with $g_X = 0.1$, $m_{\rm st} = 1$ eV, andsin $\theta_{14} = 0.1$ and different values of G_X as labeled in the figure. For these curves the other cosmological parameters have been fixed to the ΛCDM best fit except the size of the sound horizon at recombination $100\theta_{\rm MC}$ which has been adjusted to produce the corresponding values of H_0 given in the label (in units of kms^{-1}Mpc^{-1}).

in our analysis so far we have used as input parameters the ten parameters described above, so given a set of values for the ten parameters, H_0 is a derived quantity. For example for the parameters at the best fit of ΛCDM the Hubble constant comes out to be $H_0 = 67.31\,\mathrm{km}s^{-1}\mathrm{Mpc}^{-1}$. In here, however, to better control the dependence on H_0 we have traded one of the input parameters (which we chose to be the sound horizon at recombination $100\theta_{\rm MC}$) by H_0. And as we can see from Fig. 5.11 for the strong interacting scenario BAO data favour H_0 in between 65 kms^{-1}Mpc^{-1} and 70 kms^{-1}Mpc^{-1}. Indeed we see that the prediction for a strongly interacting ν_s but with H_0 as low as 60 kms^{-1}Mpc^{-1} is even worse than the case of non-interacting sterile neutrinos with $H_0 = 67.31$ kms^{-1}Mpc^{-1}.

However, a small H_0 is preferred by TT data, as we can see from Table 5.2 and Fig. 5.10. For example when using the broad (narrow) prior we find that TT data prefers $H_0 = 63.3^{+1.5}_{-2.3}$ kms^{-1}Mpc^{-1} ($H_0 = 60.26^{+0.81}_{-1.8}$ kms^{-1}Mpc^{-1}) Indeed there exists a strong correlation between H_0 and $N_{\rm eff}$ which we have shown in Fig. 5.12 where we plot the two-dimensional posterior allowed regions

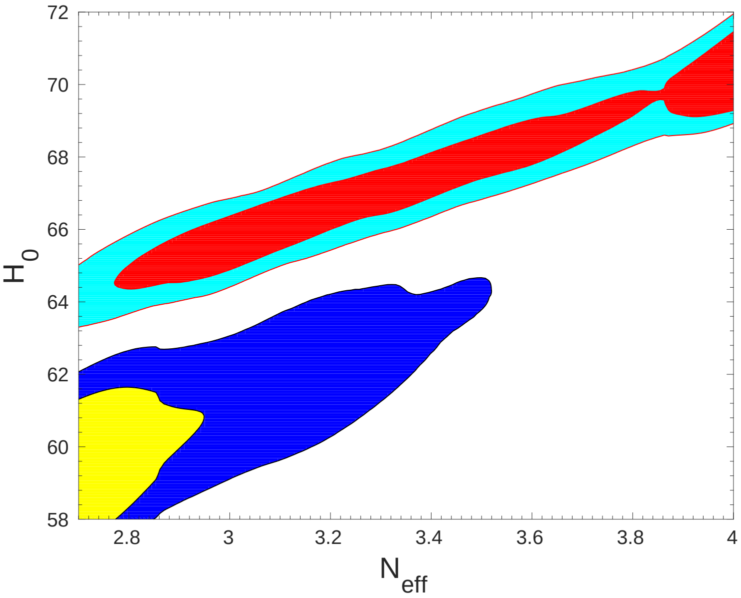

Figure 5.12: 2d posterior correlation of H_0 and $N_{\rm eff}$ in terms of narrow prior. The yellow and blue regions show the 68% and 95% credible intervals using Planck data only. The red and cyan regions are the corresponding ones using Planck+BAO data.

for those parameters from the analysis with narrow prior (the corresponding ones for the broad prior are not very different). As discussed, the change in $N_{\rm eff}$ leaves an imprint on the sound horizon at recombination, which has to be compensated by the shift in H_0. This explains the small H_0 favored by TT. However this small H_0 raises a tension with the BAO data. So when adding BAO to the analysis, a small G_X which predicts large $N_{\rm eff}$ and large H_0 can give a better overall description.

Quality of Fit

So far we have discussed the posteriors of cosmological and new interaction parameters. However, we have somehow left aside one important question: How much can we "gain" by adding new interactions to reconcile eV sterile neutrinos in cosmology? We can get an estimate of it by looking at the minimum χ^2 for the different analysis which we have summarized in Table 5.3. From the table we read that the best fit for the interacting ν_s model with the broad priors is always comparable to the ΛCDM best fit, and much better than the case without new interactions. This is because within the broad

Data	ΛCDM	Free-ν_s BP	Free-ν_s NP	Int-ν_s BP	Int-ν_s NP
TT	11262	11271	11282v	11264	11271
TT+BA O	11266	11274	11304	11267	11299

Table 5.3: $\chi^2_{\rm min}$ for various models and data combinations. "Free-ν_s BP" and "Free-ν_s NP" are models of ΛCDM with one non-interacting sterile neutrino species with $m_{\rm st}$ and θ_{14} priors as in Table 5.1 but with a fixed and very weak interaction ($G_X = 10^{-2}G_F$ so effectively for this model $N_{\rm eff} = 4$).

prior there always exists an interaction strength which predicts $N_{\rm eff} \simeq 3$ and a reasonable fit can be obtained at the lower limit of the allowed range of $m_{\rm st}$.

For the interacting ν_s model with narrow priors we find that, as for cosmological data respects, ΛCDM is a better fit by $\Delta\chi^2_{\rm min} = 9.41$ when using TT data, but still, it provides a much much better description than the non-interacting case. However, as read from the table, including BAO data (which are 4 data points) increases the χ^2 of both interacting and non-interacting scenarios with the narrow prior by $\sim$ 25 units. Therefore we conclude that new interactions have limited power to reconcile the sterile neutrinos required by the short baseline anomalies when the information from LSS is included.

Dependence on $N_{\rm eff}$ Prior

One another thing to keep in mind is that for the priors used in our previous analysis for the model parameters the derived $N_{\rm eff}$ prior is not flat but peaked at 2.7 and 4 as shown in Fig. 5.9 and while TT favours models close to the 2.7 peak, BAO disfavours them severely to the point of favouring models close to the 4 peak.

One may wonder then if for models leading to $N_{\rm eff}$ in the intermediate region one could find some some compromise. This possibility however is not observed in the posterior distribution of those analysis as a result of the "volume effect" of the priors which suppresses this possibility. It is important to stress however that the conclusion about the bad quality of the overall description of the TT+BAO data when using the narrow prior holds independently of this prior bias because it is based on the value of the minimum χ^2 of the analysis which is independent of the shape of prior probability distributions.

Still, to quantify the effect of this bias induced by the prior in the derived posterior for the broad prior analysis, we have searched for an add-hoc prior for the four model parameters which resulted into a derived prior for $N_{\rm eff}$ which was as flat as possible. We found that for this it was best to use M_X and g_X as base parameters instead of G_X and g_X. With a flat prior on $\log_{10} M_X$ for

M_X between 70 MeV and 1200 MeV and g_X still flat between 0.001 and 0.064 (so the derived range of $-2 \leq \log_{10}(G_X/G_F) \leq 4.1$) and with broad or narrow prior ranges for $m_{\rm st}$ and θ_{14}, the derived $N_{\rm eff}$ prior obtained is that shown in the corresponding curve in Fig. 5.9, which, as seen in the figure, is relatively flat between 2.7 and 4.

The resulting posterior for $m_{\rm st}$ and $N_{\rm eff}$ for the analysis with this add-hoc broad prior are shown in Fig. 5.13. The first thing we notice is that with the ad-hoc prior we do not observe the appearance of the peak in the posterior around $N_{\rm eff} = 4$ when including BAO data. We find instead that even when considering TT+BAO data $N_{\rm eff} < 3.54$ and $m_{\rm st} < 0.40$ eV at 95% CL. In what respects to the interaction parameters for the add-hoc prior we find that the full range of g_X is allowed at this CL while $70 \leq M_X \leq 931$ MeV when using TT data only (which implies $0.45 \leq \log_{10}(G_X/G_F) \leq 3.88$) while the full range of $70 \leq M_X \leq 1200$ MeV and $-0.64 \leq \log_{10}(G_X/G_F) \leq 3.36$ is allowed in the TT+BAO analysis.

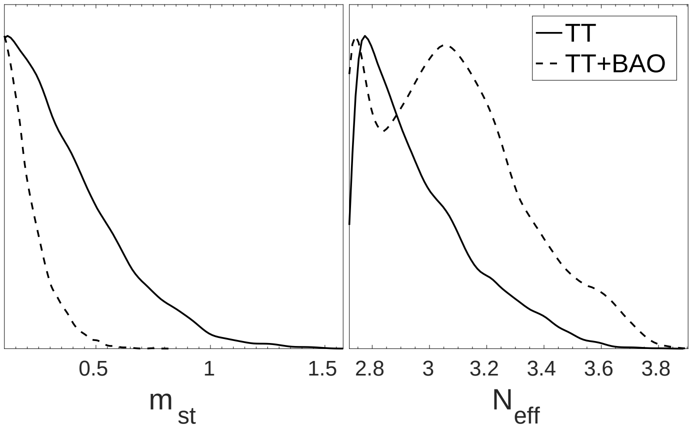

Figure 5.13: Posterior distribution of $m_{\rm st}$ and $N_{\rm eff}$ assuming the add-hoc $N_{\rm eff}$ prior and for the data combinations as labeled in the figure

We finish by commenting that when using this ad-hoc quasi-flat $N_{\rm eff}$ prior we can cross-check the results of our analysis with the corresponding analysis performed by the Planck collaboration in terms of an "effective" sterile neutrino mass with free $N_{\rm eff}$ [4]. We find that our results are consistent with those obtained by Planck collaboration in their analysis (which includes TT+lensing+BAO data) $N_{\rm eff} < 3.7$ and $m^{\rm eff}_{\nu,{\rm sterile}} < 0.38$ eV.

5.5 Summary

In this chapter we have made use of the physics of cosmological neutrinos to probe beyond the Standard Model scenarios in the neutrino sector. Our main motivation has been to test the explanations invoked to accommodate some anomalies observed in oscillation experiments at short baselines which indicate the possible existence of an additional sterile neutrino with non-negligible mixing with the three standard ones.

We started by briefly reviewing the role of neutrinos in cosmology. Their energy density and pressure affect the expansion history of universe and their free-streaming suppresses the structure formation at small scales. This leaves imprints on the CMB, BBN and LSS data which can be used to constrain the neutrino properties. As a consequence, the current cosmological data leads to bounds on the sum of neutrino masses and on the number of neutrino-like degrees of freedom N_{eff} which contradict the existence of sterile neutrinos of mass $\sim$eV as favored by the short baseline oscillation data. In this chapter we have aimed at exploring how a new self-interaction with some coupling g_X among such massive sterile neutrinos mediated by a a gauge boson of some mass M_X can (or cannot) improve the description of cosmological data.

We show that if the in-medium potential induced by the new interaction is much larger than the neutrino vacuum oscillation frequency in the early universe the production of sterile neutrinos can be postponed until after neutrino decoupling. This can lead to $N_{\mathrm{eff}} \simeq 2.7$. On the other hand, if the effective interaction strength $G_X/\sqrt{2} = g_X^2/(8M_X^2)$ is much smaller than that of electroweak interaction, the universe still ends up with $N_{\mathrm{eff}} \simeq 4$. A comparison between the new interaction model and BBN data shows that the effective coupling strength must verify $\log_{10}(G_X/G_F) \geq 3.8$ at 95% CL to correctly describe BBN.

We have also performed a Bayesian analysis of the self-interacting sterile neutrino model with Planck and BAO measurements and study the dependence on the prior ranges allowed for the model parameters. By allowing a wide prior of sterile neutrino mass, we find $m_{\mathrm{st}} \leq 0.91$ eV (95% CL) considering Planck data only and $m_{\mathrm{st}} \leq 0.37$ eV (95% CL) using a combination of Planck and BAO data. So the mass bounds are relaxed compared with that of a non-interacting sterile neutrino but a sterile neutrino mass of 1 eV is still excluded by more than 2σ CL. We also perform an analysis by fixing the sterile neutrino mass and mixing to the values preferred by short baseline data. Both analysis show that Planck data alone favors relatively large G_X, i.e. the new interaction scenario, while including BAO information significantly increases the probability of models with small G_X, i.e the non-interacting scenarios. We have shown how this can be explained by the known degeneracy between H_0

and N_{eff}—the small N_{eff} ($N_{\text{eff}} \simeq 2.7$) leads to small H_0, which is in contradiction with the BAO data.

We conclude then that adding the new interaction can alleviate the tension between eV sterile neutrinos and Planck data, but when including also the BAO data this interacting model leads to a much worse fit than the pure ΛCDM model without sterile neutrinos.

Chapter 6

Conclusions

In this thesis we have studied neutrinos from three different extraterrestrial sources: neutrinos from the Sun, ultra high energy neutrinos from astrophysical objects and relic neutrinos from the big bang. These neutrinos serve as powerful tools when studying their sources and interactions. Here we present a brief summary of our main conclusions.

- *Solar neutrinos.* In Chapters 2 and 3 we have addressed two main questions: what do we know about the solar neutrino fluxes independently of the solar models and how this knowledge together with the results of helioseismic observations can be used not only to test the predictions of solar models but to actually improve on the modeling. In particular in Chapter 2 we have shown how using Bayesian statistics techniques applied to the latest data from both solar and non-solar neutrino experiments, we can determinate the solar neutrino fluxes without invoking any solar model. We have compared the results obtained with and without imposing that nuclear physics is the only source of energy generation. This study has allowed to reduce our uncertainty in the ^{7}Be and *pp* (and correspondingly *pep*) fluxes by a factor 2, and by 30% in the ^{8}B flux compared to previous analysis. Furthermore the uncertainty on the total luminosity due to nuclear physics as derived from neutrino data has been reduced by a factor two and is now, for the first time, below 10%. Also when comparing with the predictions of standard solar models, we have shown that our bounds on CNO neutrino fluxes are very close to the theoretical 3σ range.

  Turning to the issue of the solar modeling the main motivation for our work has been the so-called solar abundance problem which has led to the existence of two sets of models differing on the set of input abundances (with either lower metallicity or higher metallicity) used in their construction with the one used the most updated abundances yielding the worse description of the helioseismic data. As both variants yield different neutrino fluxes we first checked if our determined neutrino fluxes could discriminate between the two. Our statistical comparison showed, however, that with our present flux precision, both variants lead to comparable description of the data. We have found that a future CNO flux measurement with $\sigma_{\text{CNO}} = 5\%$ uncertainty would be needed to yield a moderate evidence in favor of one of the two sets.

In Chapter 3 we have presented our contribution to possible improvements on the solar modeling which can lead to a better description of both neutrino and helioseismic results. In this study we have used the latest generation of solar models: B16-GS98 (low metalicity variant) and B16-AGSS09met (high metalicity variant) with include updates on several model inputs: some nuclear reaction rates, the treatment of the equation of state and of the opacity uncertainties. We have performed detailed comparisons of the high and low metallicity variants against different ensembles of solar observables including solar neutrinos, surface helium abundance, depth of convective envelope and sound speed profile. We have obtained that the global analysis including all observables yields a p-value of 2.7σ for the B16-GS98 model and 4.7σ for the B16-AGSS09met, with the main culprit being the inability of the models to describe the sound speed data.

We first studied how much the agreement could be improved with a more flexible modeling of the radiative opacity profile possible with the introduction of a Gaussian Process approach. Our results show that this more flexible modeling makes the preference of B16-GS98 model over B16-AGSS09 model less marked.

Next we turned to an alternative approach to the abundance problem and have developed the methodology to “build” an alternative set of Standard Solar Models which are able to describe the helioseismic and neutrino data. This is, we have shown how to turn the outputs of the model calculations into inputs. We had done so by using Bayesian inference techniques. Starting from a composition unbiased set of SSMs we have reconstructed the solar opacity profile and other inputs in a data driven way. In this way we have estimated the total opacity uncertainty (data + priors) to be 7.5% at the base of the convective envelope and 1.8% at the solar core. We have also determined the chemical composition and other solar inputs which better describe the helioseismic and neutrino observations. As an output of the study we derive the corresponding data driven predictions for the solar neutrino fluxes.

- *Astrophysical neutrinos.* The measurement of the flavor composition of the detected ultra-high energy neutrinos can be a powerful tool to learn about the mechanisms at work in their sources. Such inference, however, relies on the understanding of the particle physics processes relevant to the neutrino propagation from the source to the detector. The presence of new physics effects beyond those of the well established mass-induced 3ν oscillations alters the flavor composition at the detector and can therefore affect the conclusions on the dominant production mechanism.

  In Chapter 4 we have focused on new physscs effects associated with non-standard interactions of the neutrinos in the Earth matter. The relevant flavor transition probabilities accounting for oscillations from the source to the Earth plus the non-standard interactions in the Earth are energy independent but depend on the zenith angle of the arrival direction of the neutrinos, which is a characteristic feature of this form of new physics. Quantitatively, we have shown that, within the presently allowed range of non-standard interactions, large deviations from the standard 3ν oscillation predictions for the detected flavor composition can be expected, in particular for fluxes dominated by one flavor at the source. On the contrary we find that the expectation of equalized flavors in the Earth for sources dominated by production via pion-muon decay-chain is robust even in the presence of this form of new physics. Our results are based on coherent forward scattering but show robustness when including incoherent effects.

- *Cosmological neutrinos.* Cosmological neutrinos are the relics of the big bang. Their energy density and pressure affect the expansion history of universe and their free-streaming suppresses the structure formation at small scales. All this leaves imprints on the CMB, BBN and large scale structure data. In Chapter 5 we have studied how to apply this data to learn about extended scenarios with additional light ($\mathcal{O}(eV)$ mass) sterile neutrinos invoked to explain some anomalies observed in the oscillation data at short baseline and how the inclusion of self-interactions among these light sterile neutrinos affect the results. The foundation of the study is the well-known result that the current cosmological data leads to bounds on the sum of neutrino masses and on the number of neutrino-like degrees of freedom N_{eff} which contradict the existence of sterile neutrinos of mass ∼eV as required by the short baseline oscillation data.

  In Chapter 5 we have shown that including new interactions of coupling g_X among such massive sterile neutrinos mediated by a a gauge boson of some mass $M_X \gg T$ can induce an in-medium potential. If this potential is much larger than the neutrino vacuum oscillation frequency in the early universe the production of sterile neutrinos can be postponed until after neutrino decoupling. This leads to a reduction $N_{\text{eff}} \simeq 2.7$. On the other hand, if the effective interaction strength $G_X/\sqrt{2} = g_X^2/(8M_X^2)$ is much smaller than that of electroweak interaction, the universe still ends up with $N_{\text{eff}} \simeq 4$. We have performed an analysis of the BBN data to show that interactions with $\log_{10}(G_X/G_F) \geq 3.8$ and any value of g_X can describe the BBN results with 95% CL.

We have also confronted the predictions of the self-interacting sterile neutrino scenario with the CMB and large scale structure data by performing a Bayesian analysis including Planck and BAO measurements. By allowing a wide prior for the sterile neutrino mass, we found $m_{\text{st}} \leq 0.91$ eV (95% CL) considering Planck data only and $m_{\text{st}} \leq 0.37$ eV (95% CL) using a combination of Planck and BAO data. So the mass bounds are relaxed compared with the non-interacting sterile neutrino scenario but we still found that a sterile neutrino mass of more than 1 eV was excluded at more than 2σ CL. We have also performed the same analysis but forcing the sterile neutrino mass and mixing to the values preferred by short baseline data. Both analysis show that Planck data alone favors relatively large G_X, i.e. the new interaction scenario, while including BAO information significantly increases the probability of models with small G_X, i.e the non-interacting scenario. We have shown how this can be explained by degeneracy between H_0 and N_{eff}—the small N_{eff} ($N_{\text{eff}} \simeq 2.7$) leads to small H_0, which is in contradiction to the BAO data. As a consequence we have shown that the minimum χ^2 for any of the sterile neutrino scenarios with or without self-interactions grows by about 25 units when included the 4 BAO data points in the fit.

In conclusion, we have shown that the inclusion of the new self-interactions among the sterile neutrinos has limited power to reconcile the sterile neutrinos required by the short baseline anomalies with the cosmological observations in particular when the information from the large scale structure is included.

Bibliography

[1] N. Vinyoles, A. M. Serenelli, F. L. Villante, S. Basu, J. Bergstrm, M. C. Gonzalez-Garcia, M. Maltoni, C. Pea-Garay, and N. Song, *A new Generation of Standard Solar Models*, *Astrophys. J.* **835** (2017), no. 2 202, [`1611.09867`].

[2] A. M. Serenelli, W. C. Haxton, and C. Pena-Garay, *Solar models with accretion. I. Application to the solar abundance problem*, *Astrophys. J.* **743** (2011) 24, [`arXiv:1104.1639`].

[3] M. C. Gonzalez-Garcia, M. Maltoni, and T. Schwetz, *Updated fit to three neutrino mixing: status of leptonic CP violation*, *JHEP* **11** (2014) 052, [`arXiv:1409.5439`].

[4] **Planck** Collaboration, P. A. R. Ade et al., *Planck 2015 results. XIII. Cosmological parameters*, *Astron. Astrophys.* **594** (2016) A13, [`1502.01589`].

[5] I. Esteban, M. C. Gonzalez-Garcia, M. Maltoni, I. Martinez-Soler, and T. Schwetz, *Updated fit to three neutrino mixing: exploring the accelerator-reactor complementarity*, *JHEP* **01** (2017) 087, [`1611.01514`].

[6] I. Esteban, M. C. Gonzalez-Garcia, M. Maltoni, I. Martinez-Soler, and Schwetz, "Nufit 3.0." `http://www.nu-fit.org`, 2016.

[7] J. N. Bahcall, W. F. Huebner, S. H. Lubow, P. D. Parker, and R. K. Ulrich, *Standard Solar Models and the Uncertainties in Predicted Capture Rates of Solar Neutrinos*, *Rev. Mod. Phys.* **54** (1982) 767.

[8] Z. Xing and S. Zhou, *Neutrinos in particle physics, astronomy and cosmology.* Springer Science & Business Media, 2011.

[9] J. N. Bahcall, *The Luminosity constraint on solar neutrino fluxes*, *Phys. Rev.* **C65** (2002) 025801, [`hep-ph/0108148`].

[10] N. Grevesse and A. J. Sauval, *Standard Solar Composition*, *Space Sci. Rev.* **85** (1998) 161–174.

[11] M. Asplund, N. Grevesse, A. J. Sauval, and P. Scott, *The chemical composition of the Sun*, *Ann. Rev. Astron. Astrophys.* **47** (2009) 481–522, [`arXiv:0909.0948`].

[12] J. N. Bahcall, A. M. Serenelli, and S. Basu, *10,000 standard solar models: a Monte Carlo simulation*, *Astrophys. J. Suppl.* **165** (2006) 400–431, [`astro-ph/0511337`].

[13] S. Basu and H. M. Antia, *Constraining solar abundances using helioseismology*, *Astrophys. J.* **606** (2004) L85, [`astro-ph/0403485`].

[14] S. Basu and H. M. Antia, *Seismic measurement of the depth of the solar convection zone*, *Monthly Notices of the Royal Astronomical Society* **287** (1997), no. 1 189–198.

[15] B. Pontecorvo, *Neutrino Experiments and the Problem of Conservation of Leptonic Charge*, *Sov. Phys. JETP* **26** (1968) 984–988. [Zh. Eksp. Teor. Fiz.53,1717(1967)].

[16] V. N. Gribov and B. Pontecorvo, *Neutrino astronomy and lepton charge*, *Phys. Lett.* **B28** (1969) 493.

[17] M. C. Gonzalez-Garcia and M. Maltoni, *Phenomenology with Massive Neutrinos*, *Phys. Rept.* **460** (2008) 1–129, [`arXiv:0704.1800`].

[18] R. Davis, *A review of the Homestake solar neutrino experiment*, *Prog. Part. Nucl. Phys.* **32** (1994) 13–32.

[19] L. Wolfenstein, *Neutrino Oscillations in Matter*, *Phys. Rev.* **D17** (1978) 2369–2374.

[20] S. P. Mikheev and A. Yu. Smirnov, *Resonance Amplification of Oscillations in Matter and Spectroscopy of Solar Neutrinos*, *Sov. J. Nucl. Phys.* **42** (1985) 913–917.

[21] S. P. Mikheyev and A. Y. Smirnov, *Resonant amplification of ν oscillations in matter and solar-neutrino spectroscopy*, *Il Nuovo Cimento C* **9** (Jan, 1986) 17–26.

[22] E. Chaisson and S. McMillan, *Astronomy today.* Addison-Wesley, 2013.

[23] A. Fraknoi, D. Morrison, and S. Wolff, *Voyages through the universe*. Harcourt College Pub, 2000.

[24] R. Davis, *Solar neutrinos. II: Experimental*, *Phys. Rev. Lett.* **12** (1964) 303–305.

[25] B. T. Cleveland, T. Daily, R. Davis, Jr., J. R. Distel, K. Lande, C. K. Lee, P. S. Wildenhain, and J. Ullman, *Measurement of the solar electron neutrino flux with the Homestake chlorine detector*, *Astrophys. J.* **496** (1998) 505–526.

[26] J. N. Bahcall, *What next with solar neutrinos?*, *Phys. Rev. Lett.* **23** (1969) 251–254.

[27] **GALLEX** Collaboration, W. Hampel et al., *GALLEX solar neutrino observations: Results for GALLEX IV*, *Phys. Lett.* **B447** (1999) 127–133.

[28] **SAGE** Collaboration, J. N. Abdurashitov et al., *Solar neutrino flux measurements by the Soviet-American Gallium Experiment (SAGE) for half the 22 year solar cycle*, *J. Exp. Theor. Phys.* **95** (2002) 181–193, [`astro-ph/0204245`]. [Zh. Eksp. Teor. Fiz.122,211(2002)].

[29] **GNO** Collaboration, M. Altmann et al., *Complete results for five years of GNO solar neutrino observations*, *Phys. Lett.* **B616** (2005) 174–190, [`hep-ex/0504037`].

[30] **Kamiokande** Collaboration, Y. Fukuda et al., *Solar neutrino data covering solar cycle 22*, *Phys. Rev. Lett.* **77** (1996) 1683–1686.

[31] **Super-Kamiokande** Collaboration, M. B. Smy et al., *Precise measurement of the solar neutrino day / night and seasonal variation in Super-Kamiokande-1*, *Phys. Rev.* **D69** (2004) 011104, [`hep-ex/0309011`].

[32] **SNO** Collaboration, J. Boger et al., *The Sudbury neutrino observatory*, *Nucl. Instrum. Meth.* **A449** (2000) 172–207, [`nucl-ex/9910016`].

[33] **SNO** Collaboration, B. Aharmim et al., *Measurement of the* ν_e *and Total* ^8B *Solar Neutrino Fluxes with the Sudbury Neutrino Observatory Phase-III Data Set*, *Phys. Rev.* **C87** (2013), no. 1 015502, [`arXiv:1107.2901`].

[34] L. Oberauer, *Status of the BOREXINO solar neutrino experiment*, *Nucl. Phys. Proc. Suppl.* **77** (1999) 48–54. [AIP Conf. Proc.555,no.1,393(2001)].

[35] **Borexino** Collaboration, M. Agostini et al., *First Simultaneous Precision Spectroscopy of pp, ^{7}Be, and pep Solar Neutrinos with Borexino Phase-II*, `1707.09279`.

[36] **SNO+** Collaboration, S. Biller, *SNO+ with Tellurium*, *Phys. Procedia* **61** (2015) 205–210, [`arXiv:1405.3401`].

[37] **JUNO** Collaboration, M. He, *Jiangmen Underground Neutrino Observatory*, *Nucl. Part. Phys. Proc.* **265-266** (2015) 111–113, [`arXiv:1412.4195`].

[38] S.-B. Kim, *New results from RENO and prospects with RENO-50*, *Nucl. Part. Phys. Proc.* **265-266** (2015) 93–98, [`arXiv:1412.2199`].

[39] **LENA** Collaboration, M. Wurm et al., *The next-generation liquid-scintillator neutrino observatory LENA*, *Astropart. Phys.* **35** (2012) 685–732, [`arXiv:1104.5620`].

[40] K. Abe et al., *Letter of Intent: The Hyper-Kamiokande Experiment — Detector Design and Physics Potential —*, `arXiv:1109.3262`.

[41] **LENS** Collaboration, R. S. Raghavan, *LENS, MiniLENS: Status and outlook*, *J. Phys. Conf. Ser.* **120** (2008) 052014.

[42] J. R. Alonso et al., *Advanced Scintillator Detector Concept (ASDC): A Concept Paper on the Physics Potential of Water-Based Liquid Scintillator*, `arXiv:1409.5864`.

[43] Z. Maki, *Z. maki, m. nakagawa, and s. sakata, prog. theor. phys. 28, 870 (1962).*, *Prog. Theor. Phys.* **28** (1962) 870.

[44] **KamLAND** Collaboration, A. Gando et al., *Constraints on θ_{13} from A Three-Flavor Oscillation Analysis of Reactor Antineutrinos at KamLAND*, *Phys. Rev.* **D83** (2011) 052002, [`arXiv:1009.4771`].

[45] T.-K. Kuo and J. T. Pantaleone, *The Solar Neutrino Problem and Three Neutrino Oscillations*, *Phys. Rev. Lett.* **57** (1986) 1805–1808.

[46] J. N. Bahcall, S. Basu, M. Pinsonneault, and A. M. Serenelli, *Helioseismological implications of recent solar abundance*

determinations, *Astrophys. J.* **618** (2005) 1049–1056, [`astro-ph/0407060`].

[47] J. N. Bahcall and M. H. Pinsonneault, *Standard solar models, with and without helium diffusion and the solar neutrino problem*, *Rev. Mod. Phys.* **64** (1992) 885–926.

[48] J. N. Bahcall and M. H. Pinsonneault, *Solar models with helium and heavy element diffusion*, *Rev. Mod. Phys.* **67** (1995) 781–808, [`hep-ph/9505425`].

[49] J. N. Bahcall, M. H. Pinsonneault, and S. Basu, *Solar models: Current epoch and time dependences, neutrinos, and helioseismological properties*, *Astrophys. J.* **555** (2001) 990–1012, [`astro-ph/0010346`].

[50] J. N. Bahcall, A. M. Serenelli, and S. Basu, *New solar opacities, abundances, helioseismology, and neutrino fluxes*, *Astrophys. J.* **621** (2005) L85–L88, [`astro-ph/0412440`].

[51] M. Asplund, N. Grevesse, and J. Sauval, *The Solar chemical composition*, *Nucl. Phys.* **A777** (2006) 1–4, [`astro-ph/0410214`]. [ASP Conf. Ser.336,25(2005)].

[52] J. Bergstrom, M. C. Gonzalez-Garcia, M. Maltoni, C. Pena-Garay, A. M. Serenelli, and N. Song, *Updated determination of the solar neutrino fluxes from solar neutrino data*, *JHEP* **03** (2016) 132, [`1601.00972`].

[53] F. Feroz and M. P. Hobson, *Multimodal nested sampling: an efficient and robust alternative to MCMC methods for astronomical data analysis*, *Mon. Not. Roy. Astron. Soc.* **384** (2008) 449, [`arXiv:0704.3704`].

[54] F. Feroz, M. P. Hobson, and M. Bridges, *MultiNest: an efficient and robust Bayesian inference tool for cosmology and particle physics*, *Mon. Not. Roy. Astron. Soc.* **398** (2009) 1601–1614, [`arXiv:0809.3437`].

[55] F. Feroz, M. P. Hobson, E. Cameron, and A. N. Pettitt, *Importance Nested Sampling and the MultiNest Algorithm*, `arXiv:1306.2144`.

[56] F. Kaether, W. Hampel, G. Heusser, J. Kiko, and T. Kirsten, *Reanalysis of the GALLEX solar neutrino flux and source experiments*, *Phys. Lett.* **B685** (2010) 47–54, [`arXiv:1001.2731`].

[57] **SAGE** Collaboration, J. N. Abdurashitov et al., *Measurement of the solar neutrino capture rate with gallium metal. III: Results for the 2002–2007 data-taking period*, *Phys. Rev.* **C80** (2009) 015807, [`arXiv:0901.2200`].

[58] **Super-Kamiokande** Collaboration, J. Hosaka et al., *Solar neutrino measurements in super-Kamiokande-I*, *Phys. Rev.* **D73** (2006) 112001, [`hep-ex/0508053`].

[59] **Super-Kamiokande** Collaboration, J. P. Cravens et al., *Solar neutrino measurements in Super-Kamiokande-II*, *Phys. Rev.* **D78** (2008) 032002, [`arXiv:0803.4312`].

[60] **Super-Kamiokande** Collaboration, K. Abe et al., *Solar neutrino results in Super-Kamiokande-III*, *Phys. Rev.* **D83** (2011) 052010, [`arXiv:1010.0118`].

[61] Y. Koshio, *Solar results from Super-Kamiokande*, *AIP Conf. Proc.* **1666** (2015) 090001.

[62] **SNO** Collaboration, B. Aharmim et al., *Combined Analysis of all Three Phases of Solar Neutrino Data from the Sudbury Neutrino Observatory*, *Phys. Rev.* **C88** (2013) 025501, [`arXiv:1109.0763`].

[63] G. Bellini et al., *Precision measurement of the 7Be solar neutrino interaction rate in Borexino*, *Phys. Rev. Lett.* **107** (2011) 141302, [`arXiv:1104.1816`].

[64] **Borexino** Collaboration, G. Bellini et al., *Final results of Borexino Phase-I on low energy solar neutrino spectroscopy*, *Phys. Rev.* **D89** (2014), no. 11 112007, [`arXiv:1308.0443`].

[65] **Borexino** Collaboration, G. Bellini et al., *Measurement of the solar 8B neutrino rate with a liquid scintillator target and 3 MeV energy threshold in the Borexino detector*, *Phys. Rev.* **D82** (2010) 033006, [`arXiv:0808.2868`].

[66] **BOREXINO** Collaboration, G. Bellini et al., *Neutrinos from the primary protonproton fusion process in the Sun*, *Nature* **512** (2014), no. 7515 383–386.

[67] J. Bergstrom, M. C. Gonzalez-Garcia, M. Maltoni, and T. Schwetz, *Bayesian global analysis of neutrino oscillation data*, *JHEP* **09** (2015) 200, [`1507.04366`].

[68] T. S. M. Gonzalez-Garcia, M. Maltoni, “Nufit 2.0.” `http://www.nu-fit.org`, 2014.

[69] **Super-Kamiokande** Collaboration, R. Wendell, *Atmospheric Results from Super-Kamiokande*, *AIP Conf. Proc.* **1666** (2015) 100001, [`arXiv:1412.5234`].

[70] **Super-Kamiokande** Collaboration, R. Wendell et al., *Atmospheric neutrino oscillation analysis with sub-leading effects in Super-Kamiokande I, II, and III*, *Phys. Rev.* **D81** (2010) 092004, [`arXiv:1002.3471`].

[71] **T2K** Collaboration, K. Abe et al., *Precise Measurement of the Neutrino Mixing Parameter θ_{23} from Muon Neutrino Disappearance in an Off-Axis Beam*, *Phys. Rev. Lett.* **112** (2014), no. 18 181801, [`arXiv:1403.1532`].

[72] **MINOS** Collaboration, P. Adamson et al., *Electron neutrino and antineutrino appearance in the full MINOS data sample*, *Phys. Rev. Lett.* **110** (2013), no. 17 171801, [`arXiv:1301.4581`].

[73] **T2K** Collaboration, K. Abe et al., *Observation of Electron Neutrino Appearance in a Muon Neutrino Beam*, *Phys. Rev. Lett.* **112** (2014) 061802, [`arXiv:1311.4750`].

[74] **CHOOZ** Collaboration, M. Apollonio et al., *Limits on neutrino oscillations from the CHOOZ experiment*, *Phys. Lett.* **B466** (1999) 415–430, [`hep-ex/9907037`].

[75] **Palo Verde** Collaboration, A. Piepke, *Final results from the Palo Verde neutrino oscillation experiment*, *Prog. Part. Nucl. Phys.* **48** (2002) 113–121. [,113(2002)].

[76] **Double Chooz** Collaboration, Y. Abe et al., *Reactor electron antineutrino disappearance in the Double Chooz experiment*, *Phys. Rev.* **D86** (2012) 052008, [`arXiv:1207.6632`].

[77] **Daya Bay** Collaboration, C. Zhang, *Recent Results from the Daya Bay Experiment*, *AIP Conf. Proc.* **1666** (2015) 080003, [`1501.04991`].

[78] **RENO** Collaboration, S.-H. Seo, *New Results from RENO and The 5 MeV Excess*, *AIP Conf. Proc.* **1666** (2015) 080002, [`arXiv:1410.7987`].

[79] J. N. Bahcall and P. I. Krastev, *How well do we (and will we) know solar neutrino fluxes and oscillation parameters?*, *Phys. Rev.* **D53** (1996) 4211–4225, [`hep-ph/9512378`].

[80] M. Spiro and D. Vignaud, *Solar Model Independent Neutrino Oscillation Signals in the Forthcoming Solar Neutrino Experiments?*, *Phys. Lett.* **B242** (1990) 279–284. [,609(1990)].

[81] M. C. Gonzalez-Garcia, M. Maltoni, and J. Salvado, *Direct determination of the solar neutrino fluxes from solar neutrino data*, *JHEP* **05** (2010) 072, [`arXiv:0910.4584`].

[82] E. Caffau, H.-G. Ludwig, M. Steffen, B. Freytag, and P. Bonifacio, *Solar Chemical Abundances Determined with a CO5BOLD 3D Model Atmosphere*, *Solar Phys.* **268** (2011) 255, [`arXiv:1003.1190`].

[83] F. Delahaye and M. Pinsonneault, *The solar heavy element abundances. 1. constraints from stellar interiors*, *Astrophys. J.* **649** (2006) 529–540, [`astro-ph/0511779`].

[84] J. A. Guzik, L. S. Watson, and A. N. Cox, *Can enhanced diffusion improve helioseismic agreement for solar models with revised abundances?*, *Astrophys. J.* **627** (2005) 1049–1056, [`astro-ph/0502364`].

[85] M. Castro, S. Vauclair, and O. Richard, *Low abundances of heavy elements in the solar outer layers: Comparisons of solar models with helioseismic inversions*, *Astron. Astrophys.* **463** (2007), no. 2 755–758, [`astro-ph/0611619`].

[86] S. Basu and H. M. Antia, *Helioseismology and Solar Abundances*, *Phys. Rept.* **457** (2008) 217–283, [`arXiv:0711.4590`].

[87] J. A. Guzik and K. Mussack, *Exploring mass loss, low-Z accretion, and convective overshoot in solar models to mitigate the solar abundance problem*, *Astrophys. J.* **713** (2010) 1108–1119, [`arXiv:1001.0648`].

[88] N. Song, M. C. Gonzalez-Garcia, F. L. Villante, N. Vinyoles, and A. Serenelli, *Helioseismic and Neutrino Data Driven Reconstruction of Solar Properties*, `1710.02147`.

[89] S. Turck-Chieze and S. Couvidat, *Solar neutrinos, helioseismology and the solar internal dynamics*, *Rept. Prog. Phys.* **74** (2011) 086901, [`arXiv:1009.0852`].

[90] M. Salaris and S. Cassisi, *Evolution of stars and stellar populations.* John Wiley & Sons, 2005.

[91] G. Gamow, *Zur Quantentheorie des Atomkernes*, *Z. Phys.* **51** (1928) 204–212.

[92] E. G. Adelberger et al., *Solar fusion cross sections II: the pp chain and CNO cycles*, *Rev. Mod. Phys.* **83** (2011) 195, [`arXiv:1004.2318`].

[93] F. J. Rogers and A. Nayfonov, *Updated and expanded opal equation-of-state tables: Implications for helioseismology*, *Astrophys. J.* **576** (2002), no. 2 1064.

[94] S. Cassisi, M. Salaris, and A. W. Irwin, *The initial helium content of galactic globular cluster stars from the r-parameter: comparison with the cmb constraint*, *Astrophys. J.* **588** (2003) 862, [`astro-ph/0301378`].

[95] L. E. Marcucci, R. Schiavilla, and M. Viviani, *Proton-Proton Weak Capture in Chiral Effective Field Theory*, *Phys. Rev. Lett.* **110** (2013), no. 19 192503, [`arXiv:1303.3124`].

[96] E. Tognelli, S. Degl'Innocenti, L. E. Marcucci, and P. G. Prada Moroni, *Astrophysical implications of the protonproton cross section updates*, *Phys. Lett.* **B742** (2015) 189–194, [`arXiv:1411.5480`].

[97] B. Acharya, B. D. Carlsson, A. Ekstrm, C. Forssn, and L. Platter, *Uncertainty quantification for protonproton fusion in chiral effective field theory*, *Phys. Lett.* **B760** (2016) 584–589, [`1603.01593`].

[98] X. Zhang, K. M. Nollett, and D. R. Phillips, *Halo effective field theory constrains the solar* $^7Be + p \quad ^8B + \quad$ *rate*, *Phys. Lett.* **B751** (2015) 535–540, [`1507.07239`].

[99] **LUNA** Collaboration, M. Marta et al., *The 14N(p,gamma)15O reaction studied with a composite germanium detector*, *Phys. Rev.* **C83** (2011) 045804, [`arXiv:1103.5393`].

[100] S. Basu, W. J. Chaplim, Y. Elsworth, R. New, and A. M. Serenelli, *Fresh insights on the structure of the solar core*, *Astrophys. J.* **699** (2009) 1403–1417, [`arXiv:0905.0651`].

[101] F. L. Villante, A. M. Serenelli, F. Delahaye, and M. H. Pinsonneault, *The chemical composition of the Sun from helioseismic and solar neutrino data*, *Astrophys. J.* **787** (2014) 13, [`arXiv:1312.3885`].

[102] S. Degl'Innocenti, W. A. Dziembowski, G. Fiorentini, and B. Ricci, *Helioseismology and standard solar models*, *Astropart. Phys.* **7** (1997) 77–95, [`astro-ph/9612053`].

[103] N. R. Badnell, M. A. Bautista, K. Butler, F. Delahaye, C. Mendoza, P. Palmeri, C. J. Zeippen, and M. J. Seaton, *Up-dated opacities from the Opacity Project*, *Mon. Not. Roy. Astron. Soc.* **360** (2005) 458–464, [`astro-ph/0410744`].

[104] J. W. Ferguson, D. R. Alexander, F. Allard, T. Barman, J. G. Bodnarik, P. H. Hauschildt, A. Heffner-Wong, and A. Tamanai, *Low temperature opacities*, *Astrophys. J.* **623** (2005) 585–596, [`astro-ph/0502045`].

[105] A. Serenelli, C. Pea-Garay, and W. C. Haxton, *Using the standard solar model to constrain solar composition and nuclear reaction S factors*, *Phys. Rev.* **D87** (2013), no. 4 043001, [`arXiv:1211.6740`].

[106] S. C. Tripathy and J. Christensen-Dalsgaard, *Opacity effects on the solar interior. I. solar structure*, *Astron. Astrophys.* **337** (1998) 579, [`astro-ph/9709206`].

[107] F. L. Villante, *Constraints on the opacity profile of the sun from helioseismic observables and solar neutrino flux measurements*, *Astrophys. J.* **724** (2010) 98–110, [`arXiv:1006.3875`].

[108] W. C. Haxton and A. M. Serenelli, *CN-Cycle Neutrinos and Solar Metalicity*, `arXiv:0902.0036`.

[109] C. A. Iglesias and F. J. Rogers, *Updated Opal Opacities*, *Astrophys. J.* **464** (1996) 943.

[110] M. Krief, A. Feigel, and D. Gazit, *Line broadening and the solar opacity problem*, *Astrophys. J.* **824** (2016), no. 2 98.

[111] G. Mondet, C. Blancard, P. Coss, and G. Faussurier, *Opacity calculations for solar mixtures*, *Astrophys. J. Suppl.* **220** (2015), no. 1 2.

[112] J. Colgan, D. P. Kilcrease, N. H. Magee, M. E. Sherrill, J. A. Jr., P. Hakel, C. J. Fontes, J. A. Guzik, and K. A. Mussack, *A new generation of los alamos opacity tables*, *Astrophys. J.* **817** (2016), no. 2 116.

[113] J. E. Bailey, T. Nagayama, G. P. Loisel, G. A. Rochau, C. Blancard, J. Colgan, P. Cosse, G. Faussurier, C. Fontes, F. Gilleron, et al., *A higher-than-predicted measurement of iron opacity at solar interior temperatures*, *Nature* **517** (2015), no. 7532 56.

[114] B. Chaboyer, P. Demarque, D. B. Guenther, and M. H. Pinsonneault, *Rotation, Diffusion, and overshoot in the sun: Effects on the oscillation frequencies and the neutrino flux*, *Astrophys. J.* **446** (1995) 435, [`astro-ph/9501058`].

[115] O. Richard, S. Vauclair, C. Charbonnel, and W. A. Dziembowski, *New solar models including helioseismological constraints and light-element depletion*, *Astron. Astrophys.* **312** (1996) 1000–1011, [`astro-ph/9601136`].

[116] **IceCube** Collaboration, M. G. Aartsen et al., *First observation of PeV-energy neutrinos with IceCube*, *Phys. Rev. Lett.* **111** (2013) 021103, [`arXiv:1304.5356`].

[117] **IceCube** Collaboration, M. G. Aartsen et al., *Evidence for High-Energy Extraterrestrial Neutrinos at the IceCube Detector*, *Science* **342** (2013) 1242856, [`arXiv:1311.5238`].

[118] **IceCube** Collaboration, M. G. Aartsen et al., *Observation of High-Energy Astrophysical Neutrinos in Three Years of IceCube Data*, *Phys. Rev. Lett.* **113** (2014) 101101, [`arXiv:1405.5303`].

[119] **IceCube** Collaboration, M. G. Aartsen et al., *Evidence for Astrophysical Muon Neutrinos from the Northern Sky with IceCube*, *Phys. Rev. Lett.* **115** (2015), no. 8 081102, [`1507.04005`].

[120] L. A. Anchordoqui et al., *Cosmic Neutrino Pevatrons: A Brand New Pathway to Astronomy, Astrophysics, and Particle Physics*, *JHEAp* **1-2** (2014) 1–30, [`arXiv:1312.6587`].

[121] O. Mena, S. Palomares-Ruiz, and A. C. Vincent, *Flavor Composition of the High-Energy Neutrino Events in IceCube*, *Phys. Rev. Lett.* **113** (2014) 091103, [`arXiv:1404.0017`].

[122] M. Bustamante, J. F. Beacom, and W. Winter, *Theoretically palatable flavor combinations of astrophysical neutrinos*, *Phys. Rev. Lett.* **115** (2015), no. 16 161302, [`1506.02645`].

[123] A. Palladino, G. Pagliaroli, F. L. Villante, and F. Vissani, *What is the Flavor of the Cosmic Neutrinos Seen by IceCube?*, *Phys. Rev. Lett.* **114** (2015), no. 17 171101, [`1502.02923`].

[124] S. Palomares-Ruiz, A. C. Vincent, and O. Mena, *Spectral analysis of the high-energy IceCube neutrinos*, *Phys. Rev.* **D91** (2015), no. 10 103008, [`1502.02649`].

[125] A. Watanabe, *The spectrum and flavor composition of the astrophysical neutrinos in IceCube*, *JCAP* **1508** (2015) 030, [`arXiv:1412.8264`].

[126] N. Kawanaka and K. Ioka, *Neutrino Flavor Ratios Modified by Cosmic Ray Secondary Acceleration*, *Phys. Rev.* **D92** (2015), no. 8 085047, [`1504.03417`].

[127] **IceCube** Collaboration, M. G. Aartsen et al., *A combined maximum-likelihood analysis of the high-energy astrophysical neutrino flux measured with IceCube*, *Astrophys. J.* **809** (2015), no. 1 98, [`1507.03991`].

[128] A. C. Vincent, S. Palomares-Ruiz, and O. Mena, *Analysis of the 4-year IceCube high-energy starting events*, *Phys. Rev.* **D94** (2016), no. 2 023009, [`1605.01556`].

[129] D. Hooper, D. Morgan, and E. Winstanley, *Lorentz and CPT invariance violation in high-energy neutrinos*, *Phys. Rev.* **D72** (2005) 065009, [`hep-ph/0506091`].

[130] J. F. Beacom, N. F. Bell, D. Hooper, S. Pakvasa, and T. J. Weiler, *Decay of high-energy astrophysical neutrinos*, *Phys. Rev. Lett.* **90** (2003) 181301, [`hep-ph/0211305`].

[131] P. Baerwald, M. Bustamante, and W. Winter, *Neutrino Decays over Cosmological Distances and the Implications for Neutrino Telescopes*, *JCAP* **1210** (2012) 020, [`arXiv:1208.4600`].

[132] L. A. Anchordoqui, H. Goldberg, M. C. Gonzalez-Garcia, F. Halzen, D. Hooper, S. Sarkar, and T. J. Weiler, *Probing Planck scale physics with IceCube*, *Phys. Rev.* **D72** (2005) 065019, [`hep-ph/0506168`].

[133] D. Hooper, D. Morgan, and E. Winstanley, *Probing quantum decoherence with high-energy neutrinos*, *Phys. Lett.* **B609** (2005) 206–211, [`hep-ph/0410094`].

[134] J. F. Beacom, N. F. Bell, D. Hooper, J. G. Learned, S. Pakvasa, and T. J. Weiler, *PseudoDirac neutrinos: A Challenge for neutrino telescopes*, *Phys. Rev. Lett.* **92** (2004) 011101, [`hep-ph/0307151`].

[135] A. Esmaili, *Pseudo-Dirac Neutrino Scenario: Cosmic Neutrinos at Neutrino Telescopes*, *Phys. Rev.* **D81** (2010) 013006, [`arXiv:0909.5410`].

[136] H. Athar, M. Jezabek, and O. Yasuda, *Effects of neutrino mixing on high-energy cosmic neutrino flux*, *Phys. Rev.* **D62** (2000) 103007, [`hep-ph/0005104`].

[137] P. F. de Salas, R. A. Lineros, and M. Trtola, *Neutrino propagation in the galactic dark matter halo*, *Phys. Rev.* **D94** (2016), no. 12 123001, [`1601.05798`].

[138] C. A. Argelles, T. Katori, and J. Salvado, *New Physics in Astrophysical Neutrino Flavor*, *Phys. Rev. Lett.* **115** (2015) 161303, [`1506.02043`].

[139] M. C. Gonzalez-Garcia, M. Maltoni, I. Martinez-Soler, and N. Song, *Non-standard neutrino interactions in the Earth and the flavor of astrophysical neutrinos*, *Astropart. Phys.* **84** (2016) 15–22, [`1605.08055`].

[140] **IceCube** Collaboration, A. Achterberg et al., *On the selection of AGN neutrino source candidates for a source stacking analysis with neutrino telescopes*, *Astropart. Phys.* **26** (2006) 282–300, [`astro-ph/0609534`].

[141] E. Waxman, *Gamma-ray bursts: Potential sources of ultra high energy cosmic-rays*, *Nucl. Phys. Proc. Suppl.* **151** (2006) 46–53, [`astro-ph/0412554`].

[142] M. Kachelriess, *The rise and fall of top-down models as main UHECR sources*, in *Proceedings, 20th Rencontres de Bloise on Challenges in Particle Astrophysics: Blois, France, May 18-23, 2008*, pp. 215–224, 2008. `arXiv:0810.3017`.

[143] K. Greisen, *End to the cosmic ray spectrum?*, *Phys. Rev. Lett.* **16** (1966) 748–750.

[144] G. T. Zatsepin and V. A. Kuzmin, *Upper limit of the spectrum of cosmic rays*, *JETP Lett.* **4** (1966) 78–80. [Pisma Zh. Eksp. Teor. Fiz.4,114(1966)].

[145] J. G. Learned and S. Pakvasa, *Detecting tau-neutrino oscillations at PeV energies*, *Astropart. Phys.* **3** (1995) 267–274, [`hep-ph/9405296`].

[146] T. Kashti and E. Waxman, *Flavoring astrophysical neutrinos: Flavor ratios depend on energy*, *Phys. Rev. Lett.* **95** (2005) 181101, [`astro-ph/0507599`].

[147] P. Lipari, M. Lusignoli, and D. Meloni, *Flavor Composition and Energy Spectrum of Astrophysical Neutrinos*, *Phys. Rev.* **D75** (2007) 123005, [`arXiv:0704.0718`].

[148] M. Kachelriess, S. Ostapchenko, and R. Tomas, *High energy neutrino yields from astrophysical sources. 2. Magnetized sources*, *Phys. Rev.* **D77** (2008) 023007, [`arXiv:0708.3047`].

[149] S. Hummer, M. Maltoni, W. Winter, and C. Yaguna, *Energy dependent neutrino flavor ratios from cosmic accelerators on the Hillas plot*, *Astropart. Phys.* **34** (2010) 205–224, [`arXiv:1007.0006`].

[150] W. Winter, *Describing the Observed Cosmic Neutrinos by Interactions of Nuclei with Matter*, *Phys. Rev.* **D90** (2014), no. 10 103003, [`arXiv:1407.7536`].

[151] C. Lunardini and A. Yu. Smirnov, *High-energy neutrino conversion and the lepton asymmetry in the universe*, *Phys. Rev.* **D64** (2001) 073006, [`hep-ph/0012056`].

[152] S. Razzaque and A. Yu. Smirnov, *Flavor conversion of cosmic neutrinos from hidden jets*, *JHEP* **03** (2010) 031, [`arXiv:0912.4028`].

[153] S. Sahu and B. Zhang, *Effect of Resonant Neutrino Oscillation on TeV Neutrino Flavor Ratio from Choked GRBs*, *Res. Astron. Astrophys.* **10** (2010) 943–949, [`arXiv:1007.4582`].

[154] H. Nunokawa, B. Panes, and R. Zukanovich Funchal, *How Unequal Fluxes of High Energy Astrophysical Neutrinos and Antineutrinos can Fake New Physics*, *JCAP* **1610** (2016), no. 10 036, [`1604.08595`].

[155] A. Palladino and F. Vissani, *The natural parameterization of cosmic neutrino oscillations*, *Eur. Phys. J.* **C75** (2015) 433, [`1504.05238`].

[156] M. C. Gonzalez-Garcia and M. Maltoni, *Determination of matter potential from global analysis of neutrino oscillation data*, *JHEP* **09** (2013) 152, [`arXiv:1307.3092`].

[157] A. M. Dziewonski and D. L. Anderson, *Preliminary reference earth model*, *Phys. Earth Planet. Interiors* **25** (1981) 297–356.

[158] I. M. Shoemaker and K. Murase, *Probing BSM Neutrino Physics with Flavor and Spectral Distortions: Prospects for Future High-Energy Neutrino Telescopes*, *Phys. Rev.* **D93** (2016), no. 8 085004, [`1512.07228`].

[159] M. C. Gonzalez-Garcia, F. Halzen, and M. Maltoni, *Physics reach of high-energy and high-statistics icecube atmospheric neutrino data*, *Phys. Rev.* **D71** (2005) 093010, [`hep-ph/0502223`].

[160] C. A. Argelles Delgado, J. Salvado, and C. N. Weaver, *A Simple Quantum Integro-Differential Solver (SQuIDS)*, *Comput. Phys. Commun.* **196** (2015) 569–591, [`arXiv:1412.3832`].

[161] C. A. Delgado, J. Salvadó, and C. N. Weaver, "nusquids." `https://github.com/arguelles/nuSQuIDS`, 2016.

[162] D. Baumann, "Lecture notes for cosmology." `http://www.damtp.cam.ac.uk/user/db275/Cosmology/Lectures.pdf`, 2013.

[163] C.-P. Ma and E. Bertschinger, *Cosmological perturbation theory in the synchronous and conformal Newtonian gauges*, *Astrophys. J.* **455** (1995) 7–25, [`astro-ph/9506072`].

[164] S. Dodelson, *Modern Cosmology.* Academic Press, Amsterdam, 2003.

[165] V. F. Mukhanov, H. A. Feldman, and R. H. Brandenberger, *Theory of cosmological perturbations. Part 1. Classical perturbations. Part 2. Quantum theory of perturbations. Part 3. Extensions*, *Phys. Rept.* **215** (1992) 203–333.

[166] J. M. Bardeen, *Gauge Invariant Cosmological Perturbations*, *Phys. Rev.* **D22** (1980) 1882–1905.

[167] J. Lesgourgues and S. Pastor, *Massive neutrinos and cosmology*, *Phys. Rept.* **429** (2006) 307–379, [`astro-ph/0603494`].

[168] W. Hu, D. J. Eisenstein, and M. Tegmark, *Weighing neutrinos with galaxy surveys*, *Phys. Rev. Lett.* **80** (1998) 5255–5258, [`astro-ph/9712057`].

[169] **LSND** Collaboration, A. Aguilar-Arevalo et al., *Evidence for neutrino oscillations from the observation of anti-neutrino(electron) appearance in a anti-neutrino(muon) beam*, *Phys. Rev.* **D64** (2001) 112007, [`hep-ex/0104049`].

[170] **MiniBooNE** Collaboration, A. A. Aguilar-Arevalo et al., *Event Excess in the MiniBooNE Search for $\bar{\nu}_\mu \to \bar{\nu}_e$ Oscillations*, *Phys. Rev. Lett.* **105** (2010) 181801, [`arXiv:1007.1150`].

[171] **MiniBooNE** Collaboration, A. A. Aguilar-Arevalo et al., *Unexplained Excess of Electron-Like Events From a 1-GeV Neutrino Beam*, *Phys. Rev. Lett.* **102** (2009) 101802, [`arXiv:0812.2243`].

[172] **GALLEX** Collaboration, P. Anselmann et al., *First results from the Cr-51 neutrino source experiment with the GALLEX detector*, *Phys. Lett.* **B342** (1995) 440–450.

[173] **GALLEX** Collaboration, W. Hampel et al., *Final results of the Cr-51 neutrino source experiments in GALLEX*, *Phys. Lett.* **B420** (1998) 114–126.

[174] J. N. Abdurashitov et al., *Measurement of the response of a Ga solar neutrino experiment to neutrinos from an Ar-37 source*, *Phys. Rev.* **C73** (2006) 045805, [`nucl-ex/0512041`].

[175] G. Mention, M. Fechner, T. Lasserre, T. A. Mueller, D. Lhuillier, M. Cribier, and A. Letourneau, *The Reactor Antineutrino Anomaly*, *Phys. Rev.* **D83** (2011) 073006, [`arXiv:1101.2755`].

[176] C. Giunti and M. Laveder, *Implications of 3+1 Short-Baseline Neutrino Oscillations*, *Phys. Lett.* **B706** (2011) 200–207, [`arXiv:1111.1069`].

[177] **Daya Bay** Collaboration, F. P. An et al., *Evolution of the Reactor Antineutrino Flux and Spectrum at Daya Bay*, *Phys. Rev. Lett.* **118** (2017), no. 25 251801, [`1704.01082`].

[178] M. Dentler, . Hernndez-Cabezudo, J. Kopp, M. Maltoni, and T. Schwetz, *Sterile neutrinos or flux uncertainties? Status of the reactor anti-neutrino anomaly*, *JHEP* **11** (2017) 099, [`1709.04294`].

[179] M. Archidiacono, S. Hannestad, R. S. Hansen, and T. Tram, *Cosmology with self-interacting sterile neutrinos and dark matter - A pseudoscalar model*, *Phys. Rev.* **D91** (2015), no. 6 065021, [`arXiv:1404.5915`].

[180] X. Chu, B. Dasgupta, and J. Kopp, *Sterile neutrinos with secret interactionslasting friendship with cosmology*, *JCAP* **1510** (2015), no. 10 011, [`1505.02795`].

[181] G. Sigl and G. Raffelt, *General kinetic description of relativistic mixed neutrinos*, *Nucl. Phys.* **B406** (1993) 423–451.

[182] A. Mirizzi, N. Saviano, G. Miele, and P. D. Serpico, *Light sterile neutrino production in the early universe with dynamical neutrino asymmetries*, *Phys. Rev.* **D86** (2012) 053009, [`arXiv:1206.1046`].

[183] A. Mirizzi, G. Mangano, O. Pisanti, and N. Saviano, *Collisional production of sterile neutrinos via secret interactions and cosmological implications*, *Phys. Rev.* **D91** (2015), no. 2 025019, [`arXiv:1410.1385`].

[184] S. Esposito, G. Miele, S. Pastor, M. Peloso, and O. Pisanti, *Nonequilibrium spectra of degenerate relic neutrinos*, *Nucl. Phys.* **B590** (2000) 539–561, [`astro-ph/0005573`].

[185] Y.-Z. Chu and M. Cirelli, *Sterile neutrinos, lepton asymmetries, primordial elements: How much of each?*, *Phys. Rev.* **D74** (2006) 085015, [`astro-ph/0608206`].

[186] C. Giunti, M. Laveder, Y. F. Li, and H. W. Long, *Pragmatic View of Short-Baseline Neutrino Oscillations*, *Phys. Rev.* **D88** (2013) 073008, [`arXiv:1308.5288`].

[187] I. M. Oldengott, T. Tram, C. Rampf, and Y. Y. Y. Wong, *Interacting neutrinos in cosmology: exact description and constraints*, *JCAP* **1711** (2017), no. 11 027, [`1706.02123`].

[188] P. L. Bhatnagar, E. P. Gross, and M. Krook, *A Model for Collision Processes in Gases. 1. Small Amplitude Processes in Charged and Neutral One-Component Systems*, *Phys. Rev.* **94** (1954) 511–525.

[189] S. Hannestad and R. J. Scherrer, *Selfinteracting warm dark matter*, *Phys. Rev.* **D62** (2000) 043522, [`astro-ph/0003046`].

[190] F. Forastieri, M. Lattanzi, G. Mangano, A. Mirizzi, P. Natoli, and N. Saviano, *Cosmic microwave background constraints on secret interactions among sterile neutrinos*, *JCAP* **1707** (2017), no. 07 038, [`1704.00626`].

[191] J. Lesgourgues, *The Cosmic Linear Anisotropy Solving System (CLASS) I: Overview*, `arXiv:1104.2932`.

[192] A. D. Dolgov and F. L. Villante, *BBN bounds on active sterile neutrino mixing*, *Nucl. Phys.* **B679** (2004) 261–298, [`hep-ph/0308083`].

[193] Y. I. Izotov, T. X. Thuan, and G. Stasinska, *The primordial abundance of He-4: A self-consistent empirical analysis of systematic effects in a large sample of low-metallicity HII regions*, *Astrophys. J.* **662** (2007) 15–38, [`astro-ph/0702072`].

[194] R. Cooke, M. Pettini, R. A. Jorgenson, M. T. Murphy, and C. C. Steidel, *Precision measures of the primordial abundance of deuterium*, *Astrophys. J.* **781** (2014), no. 1 31, [`arXiv:1308.3240`].

[195] O. Pisanti, A. Cirillo, S. Esposito, F. Iocco, G. Mangano, G. Miele, and P. D. Serpico, *PArthENoPE: Public Algorithm Evaluating the Nucleosynthesis of Primordial Elements*, *Comput. Phys. Commun.* **178** (2008) 956–971, [`arXiv:0705.0290`].

[196] S. Gariazzo, C. Giunti, M. Laveder, Y. F. Li, and E. M. Zavanin, *Light sterile neutrinos*, *J. Phys.* **G43** (2016) 033001, [`1507.08204`].

[197] B. Audren, J. Lesgourgues, K. Benabed, and S. Prunet, *Conservative Constraints on Early Cosmology: an illustration of the Monte Python cosmological parameter inference code*, *JCAP* **1302** (2013) 001, [`arXiv:1210.7183`].

[198] **Planck** Collaboration, N. Aghanim et al., *Planck 2015 results. XI. CMB power spectra, likelihoods, and robustness of parameters*, *Astron. Astrophys.* **594** (2016) A11, [`1507.02704`].

[199] F. Beutler, C. Blake, M. Colless, D. H. Jones, L. Staveley-Smith, L. Campbell, Q. Parker, W. Saunders, and F. Watson, *The 6dF Galaxy Survey: Baryon Acoustic Oscillations and the Local Hubble Constant*, *Mon. Not. Roy. Astron. Soc.* **416** (2011) 3017–3032, [`arXiv:1106.3366`].

[200] A. J. Ross, L. Samushia, C. Howlett, W. J. Percival, A. Burden, and M. Manera, *The clustering of the SDSS DR7 main Galaxy sample I. A 4 per cent distance measure at* $z = 0.15$, *Mon. Not. Roy. Astron. Soc.* **449** (2015), no. 1 835–847, [`arXiv:1409.3242`].

[201] **BOSS** Collaboration, L. Anderson et al., *The clustering of galaxies in the SDSS-III Baryon Oscillation Spectroscopic Survey: baryon acoustic oscillations in the Data Releases 10 and 11 Galaxy samples*, *Mon. Not. Roy. Astron. Soc.* **441** (2014), no. 1 24–62, [`arXiv:1312.4877`].

[202] L. Anderson et al., *The clustering of galaxies in the SDSS-III Baryon Oscillation Spectroscopic Survey: Baryon Acoustic Oscillations in the Data Release 9 Spectroscopic Galaxy Sample*, *Mon. Not. Roy. Astron. Soc.* **427** (2013), no. 4 3435–3467, [`arXiv:1203.6594`].